

THESIS FOR THE DEGREE OF LICENTIATE OF ENGINEERING

Remote sensing of clouds and precipitation using active and passive microwave observations

Simon Pfreundschuh



Department of Space, Earth and Environment
CHALMERS UNIVERSITY OF TECHNOLOGY
Göteborg, Sweden 2019

Remote sensing of clouds and precipitation using active and passive microwave observations

SIMON PFREUNDSCHUH

© SIMON PFREUNDSCHUH, 2019.

Department of Space, Earth and Environment
Chalmers University of Technology
SE-412 96 Göteborg, Sweden
Telephone + 46 (0) 31 – 772 1000

Cover: Co-located observations of a convective cloud system in the Coral Sea. Optical observations from the MODIS sensor are displayed as true-color composite on the surface. Contours show the isolines of the passive microwave radiances measured by the GMI sensor. The vertical transect shows radar reflectivities measured by the CloudSat CPR.

Typeset by the author using L^AT_EX.

Printed by Chalmers Reproservice
Göteborg, Sweden 2019

Gosto de um modo carinhoso do inacabado, do malfeito, daquilo que desajeitadamente tenta um pequeno vôo e cai sem graça no chão.

— Clarice Lispector

Remote sensing of clouds and precipitation using active and passive microwave observations

Thesis for the degree of Licentiate of Engineering

Simon Pfreundschnuh

Department of Space, Earth and Environment

Chalmers University of Technology

Abstract

Global observations of clouds and precipitation are of great importance for weather prediction and the monitoring of the climate. Nonetheless, the currently available record of global observations does not constrain the properties of clouds very well owing to the inherent limitations of the observation systems used to produce them. The upcoming Ice Cloud Imager (ICI) microwave radiometer, which will be launched on the next generation of European weather satellites, will improve this situation by providing observations of clouds at sub-millimeter wavelengths. ICI will be the first sensor of its kind to deliver these observations, which will significantly improve the sensitivity to small ice particles and low mass concentrations compared to currently available microwave observations.

This thesis presents research aimed at developing knowledge and methodology required for the modeling and interpretation of the observations that will be provided by ICI. Two studies are presented which propose a method for measuring distributions of ice hydrometeors from ICI-type sub-millimeter observations combined with radar observations.

The first study uses simulated observations to assess the potential benefits of combining sub-millimeter radiometer observations with radar observations for the retrieval of ice hydrometeors. It is found that the combined observations improve the sensitivity to microphysical properties of clouds, which can help to reduce the error in the retrieved mass concentrations for specific hydrometeor types. Furthermore, improved sensitivity to supercooled liquid cloud is found as an additional synergy between the active and passive observations.

The second study aims to validate the results from the first by applying the synergistic retrieval algorithm to observations from a flight campaign. The retrieval algorithm is found to show overall good agreement with in-situ measured ice concentrations taking into account the sensitivity limits of the sensors. In addition to that, indications of a signal from mixed-phase particles are found in observations of convective updrafts. In the two presented studies, a synergistic retrieval algorithm for ice hydrometeors from radar and passive sub-millimeters has been developed, characterized and validated. The method can be applied in a future satellite mission to reduce uncertainties in global observations of clouds or used to study cloud microphysical properties in field campaigns. In addition to that, the presented application to field campaign data provides one of the rare validation cases for the radiative transfer modeling involving clouds at sub-millimeter wavelengths.

Keywords: Microwave remote sensing, hydrometeors, clouds, precipitation

Acknowledgments

First of all, I would like to thank my supervisor Patrick Eriksson for his supervision and guidance during these first two-and-a-half years of my research. For sharing his knowledge on remote sensing and radiative transfer as well as reminding me that there is more to remote sensing than just the Mathematics.

David Duncan, my co-supervisor, for his advice and inspiring discussions on remote sensing, atmospheric processes and beyond. For long runs and even longer bike rides.

Prof. Stefan A. Buehler, Dr. Manfred Brath and Oliver Lemke from the University of Hamburg for the collaboration on ARTS as well as for always finding some space for me when I am in Hamburg.

My present and former colleagues from the Division of Microwave and Optical Remote Sensing for their continuous feedback and support. Especially, I would like to thank Donal Murtagh, Vasileios Barlakas, Robin Ekelund and of course Patrick Eriksson for reading through this thesis and providing valuable feedback even on short notice.

Julia Kukulies for her feedback on this thesis and the courage required to produce it.

Simon Pfreundschnuh
Göteborg, November 2019

List of Publications

This thesis is based on the following appended papers:

- Paper 1.** Pfreundschuh, S., Eriksson, P., Buehler, S. A., Brath, M., Duncan, D., Larsson, R., and Ekelund, R. (2019). “Synergistic radar and radiometer retrievals of ice hydrometeors”, *Atmos. Meas. Tech. Discuss.*, in review.
- Paper 2.** Pfreundschuh, S., Eriksson, P., Buehler, S. A., Brath, M., Duncan, D., Ewald, F., and Delanoë, J. (2019). “Relating microphysical and radiometric properties of cloud hydrometeors at millimeter and sub-millimeter wavelengths”, *Atmos. Meas. Tech. Discuss.*, manuscript in preparation.

Other relevant publications authored or co-authored by Simon Pfreundschuh:

- Ekelund, R., Eriksson, P., and Pfreundschuh, S. (2019). “Using passive and active microwave observations to constrain ice particle models”, *Atmos. Meas. Tech. Discuss.*, in review.
- Hagen, J., Hocke, K., Stober, G., Pfreundschuh, S., Murk, A., and Kämpfer, N. (2019). “First measurements of tides in the stratosphere and lower mesosphere by ground-based Doppler microwave wind radiometry”, *Atmos. Chem. Phys. Discuss.*, in review.
- Duncan, D. I., Eriksson, P., and Pfreundschuh, S. (2019). “An experimental 2DVAR retrieval using AMSR2”, *Atmos. Meas. Tech. Discuss.*, accepted.
- Duncan, D. I., Eriksson, P., Pfreundschuh, S., Klepp, C., and Jones, D. C. (2019). “On the distinctiveness of observed oceanic raindrop distributions”, *Atmos. Chem. Phys.*, 19, 6969–6984, <https://doi.org/10.5194/acp-19-6969-2019>.
- Pfreundschuh, S., Eriksson, P., Duncan, D., Rydberg, B., Håkansson, N., and Thoss, A (2018). “A neural network approach to estimating a posteriori distributions of Bayesian retrieval problems”, *Atmos. Meas. Tech.*, 11, 4627–4643, <https://doi.org/10.5194/amt-11-4627-2018>.

Contents

Abstract	v
Acknowledgments	vii
List of Publications	ix
I Introductory chapters	1
1 Introduction	3
1.1 The role of clouds and precipitation in numerical weather prediction	4
1.2 The role of clouds and precipitation in the climate system	5
1.2.1 The global energy budget	5
1.2.2 Cloud radiative effect and climate sensitivity	5
1.3 Global observations of clouds	6
1.3.1 Frequency domains	6
1.3.2 Active and passive sensors	7
1.3.3 A look into the future	8
2 The physics of clouds and precipitation	11
2.1 Types of hydrometeors	11
2.2 The physics of cloud formation	12
2.3 Warm clouds	13
2.3.1 Formation	13
2.3.2 Growth processes	13
2.4 Cold clouds	14
2.4.1 Formation	14
2.4.2 Growth processes	15
2.4.3 Ice habits	15
2.5 Precipitation	15
3 Microwave radiative transfer in the atmosphere	17
3.1 The theory of radiative transfer	17
3.1.1 Interactions with matter	18
3.1.2 The radiative transfer equation	20
3.2 Microwave observations of clouds and precipitation	21

3.2.1	Liquid hydrometeors	21
3.2.2	Frozen hydrometeors	22
3.2.3	Sub-millimeter wavelengths	23
4	Inverse problems	25
4.1	Formulation	25
4.2	Solution	26
4.3	Error estimation	27
4.3.1	The idealized case	27
4.3.2	Handling forward model error and non-linearity	28
5	Summary of appended papers and outlook	29
5.1	Paper A: Synergistic radar and radiometer retrievals of ice hydrometeors	29
5.1.1	Data and methods	29
5.1.2	Results	30
5.1.3	Conclusions	30
5.2	Paper B: Relating microphysical and radiometric properties of cloud hydrometeors at millimeter and sub-millimeter wavelengths	30
5.2.1	Data and method	30
5.2.2	Results	31
5.2.3	Conclusions	31
5.3	Outlook	31
5.3.1	Relevance of the results	31
5.3.2	Future work	32
	Bibliography	33
II	Appended papers	37
1	Synergistic radar and radiometer retrievals of ice hydrometeors	39
2	Retrieving ice hydrometeors from radar and sub-millimeter observations: Validation of radiative transfer modeling and sensitivity to cloud microphysics	77

Part I

Introductory chapters

Chapter 1

Introduction

Clouds and precipitation affect life on Earth in various ways and on multiple time scales. On short time scales, weather affects human activity, potentially posing threats to transport, agriculture and lives. On longer time scales, precipitation patterns shape ecosystems and societies while clouds influence the global climate by means of their interaction with the incoming and outgoing electromagnetic radiation. Understanding and predicting weather and climate has been a human endeavor dating back at least to the formation of the first settled communities during the agricultural revolution (Hellmann 1908). This is easily understood considering the dependence of agricultural activity on benign weather patterns. Today, this dependency may have even increased as more and more branches of human activity rely on the availability of accurate weather forecasts.

With the dramatic effects of anthropogenic climate change becoming more and more apparent (Coronese et al. 2019; Grinsted et al. 2019), it is indisputable that a firm understanding of the Earth's climate system is critical to ensure a safe passage into this uncertain future. The predicted heating under all but the lowest emission scenarios is likely to exceed 2 °C by the end of the century (Collins et al. 2013). With this, global mean surface air temperature will likely surpass even the highest temperatures found in reconstructions of the climate of the past two million years (Masson-Delmotte et al. 2013). To ensure effective adaptation to these drastic changes, comprehensive observation and modeling of the Earth's climate is indispensable.

The subject of this thesis are observational methods for clouds and precipitation using microwave radiation. These observations provide a monitoring system for the climate on Earth and are crucial ingredients in today's weather forecasting systems. In addition to this, they provide a reference for the evaluation and improvement of climate models. More specifically, the research presented here focuses on observations of clouds at sub-millimeter wavelengths. Such observations will become available with the upcoming second generation of European operational weather satellites (Metop-SG). The aim of the presented research is to develop the methodology and know-how, which is necessary to make effective use of these novel observations. The two presented projects focus on the combination of observations from passive sub-millimeter radiometers with those from a radar and the question how these can be used to more accurately determine the properties of clouds.

The remainder of this section provides an overview over the relevance of observations of clouds for both weather and climate applications and closes with a discussion of currently available observation methods. The following chapters then provide an introduction to the physical and mathematical principles upon which these observations are founded. Chapter 2 provides an introduction to cloud formation and establishes what properties of clouds can be observed. Chapter 3 introduces the theory of radiative transfer which is necessary to understand the observable effects that clouds have on microwave radiation. Chapter 4 introduces the mathematical methods that are used to infer relevant properties of clouds from remote sensing observations.

A brief note on the terminology: The term “hydrometeor” will be used frequently in the following chapter to denote the aqueous particles that make up clouds and precipitation. Moreover, the viewpoint adopted here is that precipitation is a byproduct of cloud formation and therefore the terms *observations of clouds* or *cloud observations* are used to denote observations of both clouds and, if present, precipitation.

1.1 The role of clouds and precipitation in numerical weather prediction

Clouds and precipitation are responsible for many of the phenomena that are considered as weather. The most prominent example for this are certainly storms which can bring strong winds and heavy precipitation. It is clear that accurate representation clouds in numerical weather prediction (NWP) models is an essential requirement for reliable forecasts. But clouds, more specifically observations of clouds, can impact weather forecasts in another, more nuanced way.

The forecasting systems which are used to generate weather forecasts make use of satellite observations to determine an optimal initial state from which a forecast run is started. This process is called data assimilation. In a clear atmosphere, satellite observations from infrared and microwave sensors provide direct information on the temperature and humidity field of the atmosphere. By assimilating observations over multiple time steps, these observations can provide additional information on the dynamical state of the atmosphere (Geer et al. 2018).

Clouds form where warm and moist air is transported upwards in the atmosphere. Because of this relation to the dynamics of the atmosphere, clouds act as a tracer from which a data assimilation system can extract valuable information on the state of the atmosphere. Indeed, owing to recent developments in data assimilation methodology, microwave observations sensitive to humidity and clouds have become a main contributor to short-term forecast skill (Geer et al. 2017).

1.2 The role of clouds and precipitation in the climate system

Clouds are an integral part of the global hydrological cycle in which they deliver water from the atmosphere to the surface of the Earth. They are also tightly coupled to the dynamics of the atmosphere through the effects of latent heat and the modulation of atmospheric heating profiles (Bony et al. 2015). Their principal impact on the climate system, however, is through their interaction with the incoming solar radiation and the outgoing long-wave radiation.

1.2.1 The global energy budget

The short-wave radiation emitted by the sun that reaches the earth is the energy source that drives the climate system. To remain at a stable temperature, the Earth needs to emit the same amount of incoming energy in the form of outgoing long-wave radiation. From an energy balance perspective, clouds have two opposing effects on the global energy budget: Firstly, a cooling effect caused by the reflection of incoming short-wave radiation back to space, and secondly, a warming effect caused by the blocking of outgoing long-wave radiation that would be emitted to space in a cloud-free atmosphere. Overall, the reflection of incoming sunlight dominates, so that clouds exercise a net cooling effect on the climate system.

1.2.2 Cloud radiative effect and climate sensitivity

Since both the cooling and warming effects of clouds are relatively strong, changes in cloud properties or occurrence have the potential to cause significant feedbacks in a changing climate. These effects, however, are difficult to quantify. This is because the strength and the type of the interaction between clouds and the incoming or outgoing radiation depends on where these clouds form in the atmosphere. In addition to this, they are affected also by the microphysical properties of the cloud, e.g. particle shape, phase and size distribution.

An additional difficulty in representing the effect of clouds in the general circulation models (GCMs) that are used for climate prediction is that their formation and evolution involves processes at size-ranges beginning at the nanometer scales of aerosol particles on which cloud drops form up to several thousands of kilometers, which is the size of synoptic-scale cyclones. Since such a range of size-scales cannot be represented explicitly in a GCM, models have to rely on approximate representations of cloud processes.

Regarding predictions of future climate, it is indeed the strength of feedback effects involving clouds that exhibit the largest spread between different models. Clouds are therefore recognized as one of the major sources of uncertainty in current climate models and contribute significantly to the spread in predicted changes of global mean surface temperature that is observed between different GCMs (Boucher et al. 2013).

1.3 Global observations of clouds

The two previous sections described the relevance of cloud observations for weather and climate applications. From this we now turn to a brief review of currently available observation methods for clouds. The focus here is on satellite-based systems, since these are the only ones that can simultaneously provide observations at global scale and sufficiently high temporal sampling.

1.3.1 Frequency domains

Hydrometeors can be observed from the optical domain down to microwave frequencies around 10 GHz. The strength of their interaction with radiation depends on the relation of their size to the wavelength of the radiation. The interaction is strongest when the wavelength is close to the size of the particles.

In the optical domain, cloud droplets and ice crystals are large compared to the wavelength of the radiation, which is why they efficiently scatter of radiation at these wavelengths. The high number concentrations of these particles present in clouds make most of them opaque. For observations in the infrared, the wavelength approaches the size of the smallest hydrometeors around $5\ \mu\text{m}$. Since this further increases the strength of the interaction between the cloud particles of the radiation, clouds become even more opaque at these frequencies.

This has important implications for cloud observations using optical or infrared radiation. Due to the opacity of most clouds, the observed radiation is sensitive only to the upper-most regions of the cloud. Observational techniques based on these wavelengths have therefore no direct sensitivity to precipitation and large parts of the mass of thick clouds.

At microwave frequencies, the wavelength of the radiation is much larger than the size of the hydrometeors, which renders it insensitive to all but the largest hydrometeors. The advantage of microwave observations, however, is that they can directly sense precipitation, which occurs at the base of and below clouds that are too thick for optical or infrared radiation to penetrate.

An example of this is given in Fig. 1.1, which shows simultaneous observations of a tropical cloud system in the optical and the microwave domain. Each panel shows a true-color composite overlaid with the isolines of microwave observations at different wavelengths. Considering the lowest microwave frequency (Panel (a)), 10 GHz, it can be seen that the microwave observation exhibits structure in those regions where the optical image is saturated, i.e. only the white cloud top is visible. As the frequency increases (Panel (b) and (c)), the structures observed in microwave image become more complex, since the sensitivity of the radiation to hydrometeors as well as water vapor increases. At 183 GHz (Panel (d)), the sensitivity to atmospheric humidity is so large that the radiation cannot sense the lower troposphere anymore. A signal from the cloud is therefore only observed where it reaches high enough altitudes for its ice particles to scatter the up-welling thermal radiation. We will turn back to this scene for a more detailed discussion of the observable effects of clouds and

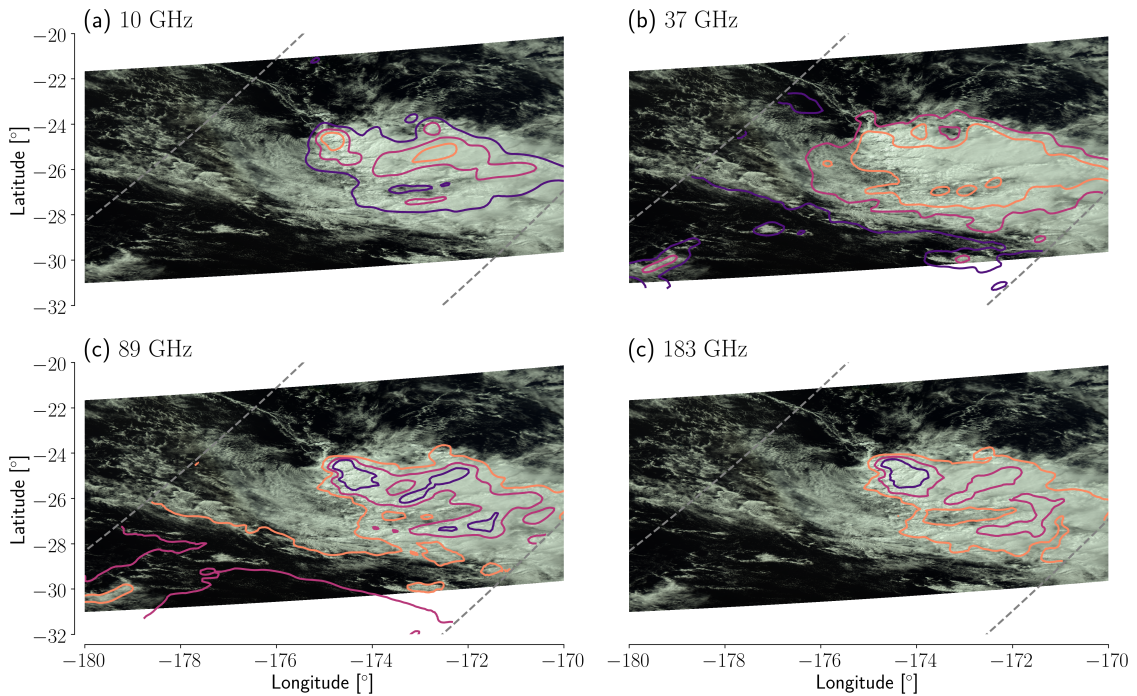


Figure 1.1: The background image in each panel shows true-color composites of observations from the MODIS sensor. Plotted on top are the contours of the radiances of different channels of the GMI (Draper et al. 2015) radiometer. Dashed, gray lines mark the boundaries of the GMI swath.

precipitation on microwave radiation in Chapter 3, which explains the principles of radiative transfer in the presence of clouds and precipitation.

1.3.2 Active and passive sensors

So far, only observations from passive sensors have been discussed. Passive sensors are sensors that measure the radiation emitted by the sun or the earth system. The signal observed by passive sensors at wavelengths shorter than $5 \mu\text{m}$ is dominated by sunlight that was scattered or reflected by the Earth or its atmosphere. At longer wavelengths, i.e. in the thermal infrared and microwave regions of the electromagnetic spectrum sensors measure the thermal emission from the Earth's surface or atmosphere.

In contrast to this, active sensors emit radiation themselves and measure the amount of if that is reflected back to the sensor. The two types of active sensors that are relevant for studying clouds are radars and lidars. The main difference between radar and lidars are the frequencies at which they operate: While a radar uses microwaves, lidars operate at infrared, optical or UV wavelengths. The advantage of active sensors is that they can provide vertically resolved observations and generally have greater sensitivity than their passive counterparts. The vertical resolution, however, generally comes at the cost of a decreased horizontal coverage. Active sensors therefore typically provide significantly lower temporal sampling of specific locations on Earth than their passive counterparts.

As an example for observations from an active sensor, radar observations of the

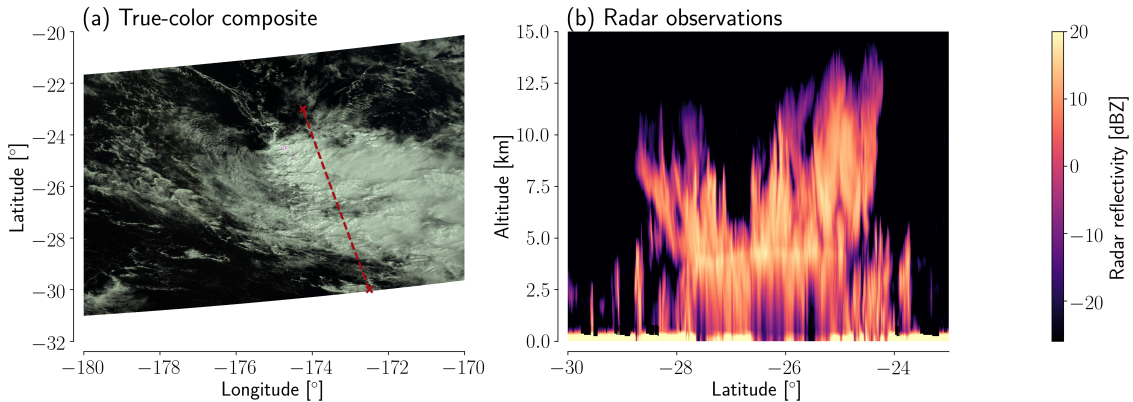


Figure 1.2: Radar observations of the tropical cloud system shown in Fig. 1.1. Panel (a) displays once again the observations from the optical domain together with the ground track of the radar observations (dashed, red line). Panel (b) displays the radar reflectivities observed by the Cloud Profiling Radar on the CloudSat satellite (Tanelli et al. 2008) along the track marked in Panel (a).

tropical scene considered above are displayed in Fig. 1.2. Shown in Panel (a) of the figure are once again the passive observations in the optical together with the ground track of the radar observations. The radar observations along the ground track are displayed in Panel (b) of the figure. The radar observations nicely reveal the intricate vertical structure of the cloud. In the northernmost part of the cloud system, the cloud reaches up to altitudes of almost 15 km, a sign of strong convective activity. Moreover, a radar signal that reaches down to the surface is observed almost everywhere in the cloud, indicating the presence of precipitation.

1.3.3 A look into the future

There is a considerable gap in the available wavelengths for the observations of clouds between the shortest microwave wavelengths around 2 mm and the longest infrared wavelength at around 15 μm . This gap is partly due to the strength of the water vapor continuum in this region of the electromagnetic spectrum, which effectively makes the troposphere invisible for large parts of the range, as well as technological difficulties in the development of sensors for these wavelengths.

Nonetheless, progress is underway to narrow down this wavelength gap. The Ice Cloud Imager (ICI, Buehler et al. (2012)) is a new type of sensor that will be flown on the upcoming second generation of European operational meteorological satellites (Metop-SG). It will provide observations of the atmosphere at frequencies up to 664 GHz corresponding to a wavelength of less than 0.5 mm. These observations at sub-millimeter wavelengths will considerably increase the sensitivity to small particles and lower hydrometeor masses. Moreover, ICI is expected to also provide increased sensitivity to the shape of ice particles.

Since ICI will be the first sensor of its kind to provide observations of clouds at sub-millimeter wavelengths, the development of new methodology and know-how is required to fully exploit their potential. ICI's sensitivity to the microphysical properties of hydrometeors requires improvements of their representation in radiative

transfer models and better knowledge of their characteristic distribution in the atmosphere to accurately simulate and understand the impact of ice particles on sub-millimeter observations. Contributing to these preparations for the ICI sensor are the principal aims of the research project that led to this thesis.

Chapter 2

The physics of clouds and precipitation

Clouds consist of large numbers of water droplets and ice crystals that are suspended in the air. When these drops grow sufficiently in mass they eventually fall out of the cloud to form precipitation. This chapter gives an overview over the processes that lead to the formation of clouds and ultimately precipitation. Moreover, the typical properties of the hydrometeors that make up clouds and precipitation are presented. This knowledge is required to understand the capabilities and limitations of the observational approaches considered in the remainder of this thesis. The presentation given below is based on the book by Lohmann et al. (2016).

The discussion of clouds presented here focuses on their microphysical properties and therefore distinguishes between warm and cold clouds. Warm clouds exist below the 0 °C isotherm and consist solely of liquid water droplets. Cold clouds extend above the 0 °C isotherm and consist at least in part of ice particles. Although, typically, the liquid phase is present also in cold clouds, this classification allows the slightly different formation processes of liquid and frozen hydrometeors to be discussed separately. Although it is common to further classify clouds according to their structure and the dynamical context of their formation, this only indirectly affects their interaction with radiation and is therefore neglected here.

This chapter begins with a brief overview over the different hydrometeor types and sizes present in clouds. Thereafter, phase transitions are introduced which form the basis of cloud formation processes. This is followed by a description of the formation and growth processes in warm and cold clouds. The chapter closes with a brief discussion of the general properties of precipitation.

2.1 Types of hydrometeors

Liquid cloud droplets form through the activation of solution droplets, which are aerosols that have taken up humidity from their environment. The typical sizes of cloud droplets range from 5 μm to 20 μm and they are the smallest particles that can be found in tropospheric clouds. If cloud droplets grow by colliding with other cloud droplets they eventually become drizzle drops, which have typical sizes starting

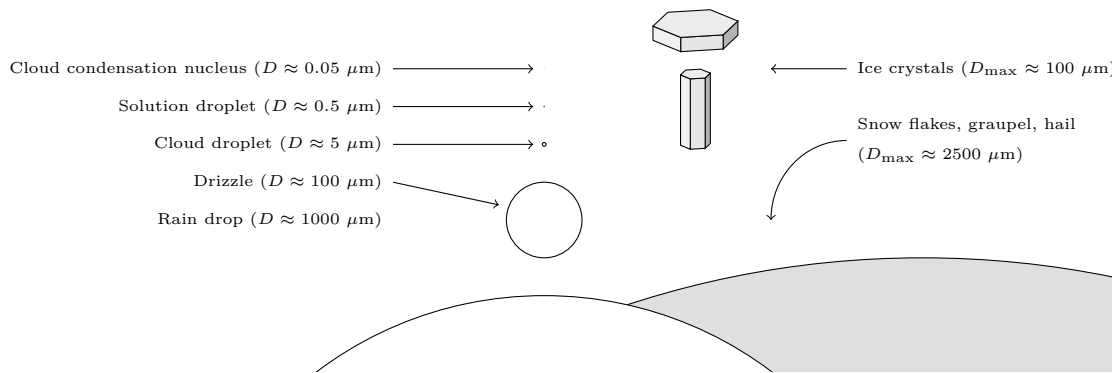


Figure 2.1: Types of hydrometeors and their sizes. The figure schematically displays the different particles formed inside clouds. The particles are drawn to scale with an enlargement factor of 1000.

from $100 \mu\text{m}$ and are heavy enough to fall out of the cloud and reach the ground. When sufficiently many other droplets are available, drizzle droplets can continue to grow to form rain drops which have sizes from 1 to about 4 mm.

Ice crystals are the frozen counterpart to cloud droplets and typically have sizes around $100 \mu\text{m}$ but can become significantly larger and even fall out of the cloud to reach the ground. Graupel is created when ice crystals collide with cloud droplets that freeze upon the ice crystal. This process is called riming. When an ice crystal grows to sizes larger than 2.5 mm through riming it is called a hailstone (Ch. 11, Lohmann et al. (2016)). Snow flakes consist of aggregates of ice crystals and range in sizes from millimeters to centimeters.

The different types of hydrometeors and their respective sizes are summarized in Fig. 2.1. It should be noted that the size given in the figure as well as the above paragraphs are only indications of size range corresponding to each particle type. Their exact sizes can vary greatly from particle to particle and from cloud to cloud.

2.2 The physics of cloud formation

Cloud hydrometeors form when water vapor contained in the air undergoes a phase change from the gas phase to the liquid or frozen phase. This process is denoted as condensation, for the change from the gas to the liquid phase, and deposition, for the change from the gas to the ice phase.

A necessary condition for condensation to occur is that the air is supersaturated with respect to liquid water. This means that the partial pressure of water vapor exceeds the saturation vapor pressure with respect to liquid water. Similarly, supersaturation with respect to the ice phase is required for the formation of ice particles. The supersaturation required for cloud formation is reached when comparably warm and moist air is lifted in the atmosphere. The resulting adiabatic cooling of the air leads

to a decrease in the saturation vapor pressures of water and ice and the air eventually becomes supersaturated.

When water vapor reaches supersaturation with respect to either the liquid or ice phase it enters a metastable state. This means that although the liquid state is energetically favorable the transition is inhibited by an energy barrier. Due to the random nature of the movements of water vapor molecules, some of them eventually overcome the energy barrier by forming clusters of the new stable phase inside the metastable gas phase. In the context of phase transitions, this process of forming clusters of the stable state inside the metastable parent state is referred to as nucleation. More specifically, two types of nucleation are distinguished: Homogeneous nucleation refers to the process of forming a new, pure cluster of molecules in the stable phase whereas heterogeneous nucleation refers to the formation of a cluster of molecules in the stable phase on or around a cluster of a different molecular species. After a sufficiently large nucleus has formed, it will grow due to the condensation or deposition of water molecules as long as its environment is supersaturated with respect to its phase. Eventually, differences in fall velocities between particles of different sizes will cause them to collide and stick together.

Due to the different molecular properties of water and ice, slightly different processes are involved in the formation of liquid cloud droplets and ice particles. These together with the corresponding growth mechanism are explained in more detail in the following two sections.

2.3 Warm clouds

As mentioned above, warm clouds are clouds that do not extend above the 0 °C-isotherm and consist solely of liquid cloud droplets.

2.3.1 Formation

The formation of cloud droplets by homogeneous nucleation is highly unlikely due to the height of the energy barrier separating the metastable gas phase from the liquid phase. Instead, cloud droplets form through the activation of cloud condensation nuclei (CCN). CCN are soluble aerosol particles, which take up water molecules and grow even in environments that are not super-saturated. The droplets which are formed by hygroscopic growth of aerosol particles are called solution droplets (c.f. Fig. 2.1). For sufficiently high supersaturations, the energy barrier for the transition to larger cloud drops vanishes leading to immediate condensation of all water molecules onto the droplet which are available in its surroundings. The theory describing the activation of CCN and their growth to cloud droplets is known as Köhler theory (Köhler 1936).

2.3.2 Growth processes

The condensation of water molecules onto the newly formed cloud droplet causes a gradient in the concentration of water molecules initiating a diffusive flow of water

vapor towards the droplet. The water vapor flowing towards the droplet condenses onto it causing it to grow in size and mass. This process is called growth by diffusion and condensation. The rate of diffusional growth decreases with increasing droplet radius. For sizes larger than $20 \mu\text{m}$ it has become so inefficient that another growth process takes over.

When the cloud droplets have grown sufficiently in mass, differences in fall speed between droplets of different size or turbulence may cause droplets to collide. If these droplets coalesce the resulting droplet will have grown compared to the two colliding droplets. The newly-formed larger particle will fall even faster through the cloud. Since heavier particles typically are more efficient in collecting other cloud droplets, this illustrates why collision-coalescence is a very efficient growth process. Only collision-coalescence can explain the onset of rain only 20-30 minutes after the formation of a cumulus cloud which can be observed in the atmosphere (Ch. 7, Lohmann et al. (2016)).

2.4 Cold clouds

Cold clouds extend above 0°C -isotherm and are characterized by the presence of frozen hydrometeors.

2.4.1 Formation

In contrast to liquid droplets, both homogeneous and heterogeneous nucleation are relevant for the formation of ice particles in the atmosphere. In agreement with Oswald's rule of stages, homogeneous nucleation occurs only through the liquid phase due to the prohibitively high energy barrier associated with the formation of an ice nucleus directly from the vapor phase. This means that ice particles are formed by homogeneous nucleation through the formation of an ice nucleus inside an existing cloud or solution droplet and subsequent complete freezing of the droplet. Nonetheless, the energy barrier for homogeneous nucleation of ice particles remains so high that these processes occur only at temperatures below -36°C for solution droplets and -38°C for cloud droplets.

Heterogeneous nucleation of ice particles involves aerosol particles, so called ice nucleating particles (INP), which provide a surface onto which the water molecules can form aggregates with ice-like structure. Heterogeneous nucleation is thought to occur both directly from the gas to the ice phase as well as indirectly through an intermediate liquid phase particle. Heterogeneous freezing, that is heterogeneous nucleation from the liquid phase, occurs when a cloud droplet or a solution droplet comes in contact with an INP upon which the droplet freezes. Heterogeneous freezing may also occur when water vapor condenses directly onto the INP followed by freezing of the liquid nucleus formed on the INP.

Alternatively, heterogeneous nucleation may occur directly from the vapor phase by deposition of water molecules onto the INP. It is, however, still debated whether this process really occurs directly from the vapor phase or whether an intermediate liquid nucleus is formed on the INP.

2.4.2 Growth processes

In principle, the growth processes for ice particles are the same as for liquid droplets. However, due the potential coexistence of particles in the liquid phase these processes have slightly different characteristics as will be explained below.

Due to the lower saturation vapor pressure of ice compared to that of water, a newly-formed ice nucleus experiences a much higher ratio of supersaturation after its formation than a cloud droplet would. This leads to a diffusional growth of ice crystals much faster rates than that of cloud droplets. The rapid growth of the ice particles will deplete the surrounding air of water vapor. This depletion may cause the environment to become sub-saturated with respect to water while it remains saturated with respect to ice. If this is the case, potentially present supercooled cloud droplets evaporate and their molecules deposit onto the ice particles. This is known as the Wegener-Bergeron-Findeisen process.

Similar as for cloud droplets, an ice crystal that grows sufficiently in mass eventually starts to sediment. Size differences between different particles as well as turbulence may cause particles to collide and potentially stick together to form larger particles thus initiating growth by accretion. Accretion is the general term for the growth of hydrometeors caused by the collision of two particles resulting in a permanent union of the two particles. For ice particles, growth by accretion can happen in two ways: The collision of two ice particles, which is called aggregation, or the collision of an ice particle with a liquid particle, which is called riming. Aggregation produces aggregates of snow crystals that, if they don't melt, fall to the ground in the form of snow. Particles produced by riming are known as graupel, when their diameter remains below 2.5 mm, and hail for sizes above that.

2.4.3 Ice habits

Ice crystals exhibit a fascinating range of different forms. Their crystal structure depends on the thermodynamic conditions of their formation. This is because the anisotropic surface tension of a newly formed ice nucleus depends on the temperature and supersaturation.

It is common to distinguish three class of frozen hydrometeors: Pristine ice crystals, aggregates and rimed particles. Common shapes for ice crystals are plates and columns (c.f. Fig 2.1). But also other shapes such as dendrites, stellar plates or needles can be observed. Snow aggregates are usually made up of 10 to 100 or more single crystals. They often consist of dendrites and thin plates. Finally, rimed particles are typically spherical with densities slightly lower than that of solid ice due air inclusions.

2.5 Precipitation

Precipitation occurs when the hydrometeors inside a cloud have grown sufficiently for their fall speeds to exceed the updraft velocity. Due to the ineffectiveness of diffusional growth for cloud droplets and ice crystals at larger particle sizes, growth

by collision-coalescence and growth by accretion are required to form precipitation at the rates observed in the atmosphere.

The exception to this rule is a phenomenon called cloud-less ice precipitation which refers to ice particles that grow large enough to sediment and reach the ground. This, however, occurs only in very cold climates with clean air such as the Arctic and is therefore not relevant at global scales.

Since the transition between suspended cloud hydrometeors and precipitating hydrometeors is continuous no explicit distinction will be made in the following between the two. Instead ice hydrometeors will be considered as a single species of particles include ice crystals, snowflakes, graupel and hail.

Chapter 3

Microwave radiative transfer in the atmosphere

The underlying physical mechanism that allows cloud and precipitation to be remotely sensed is their interaction with electromagnetic radiation that can be measured from afar using suitable detectors. These interactions are described by the theory of radiative transfer. Since this theory is essential for the understanding and development of retrieval methods, this section provides an introduction to radiative transfer of microwaves in the atmosphere. The focus is put on the interaction of radiation with clouds. This presentation is mostly based on the more comprehensive texts by Mishchenko et al. (2002), Thomas and Stamnes (2002), and Wallace and Hobbs (2006).

3.1 The theory of radiative transfer

Radiative transfer theory describes radiation as monochromatic beams that transport radiant energy through the atmosphere. One of the fundamental quantities of the theory is the spectral intensity I_ν defined as the rate at which a beam consisting of radiation from an infinitesimal frequency interval $d\nu$ centered at ν , with angular extent $d\omega$ and propagating into direction $\hat{\mathbf{n}}$, transports energy through an infinitesimal area dA :

$$I_\nu = \frac{d^5 E}{\cos(\theta) dA dt d\omega d\nu} \quad (3.1)$$

where $\cos(\theta)$ is the incidence angle between the surface normal of A and the direction of propagation of the beam. In addition to that, a monochromatic beam of radiation has a polarization state, which describes how the energy flux is split up between the two components of the electric field perpendicular to the propagation direction as well as their respective phase. The intensity of a beam and its polarization state are

described by the Stokes vector

$$\mathbf{I} = \begin{bmatrix} I_\nu \\ Q \\ U \\ V \end{bmatrix} \quad (3.2)$$

The four components I_ν, Q, U and V of the Stokes vector fully characterize an electromagnetic plane wave to the extent that it can be measured using traditional detectors. This means that all measurable quantities of the radiation can be derived from the corresponding Stokes vector.

The Stokes vector can be directly related to the electromagnetic field strength of an electromagnetic plane wave allowing it to be derived from the more fundamental theory of electromagnetism. The key advantage of radiative transfer theory, however, is that it allows a simplified treatment of the problems relevant to atmospheric remote sensing which are too complex to be solved by direct application of the laws of electrodynamics.

3.1.1 Interactions with matter

The Stokes vector provides a full description of the radiation measured by any passive remote sensing instrument. To model the radiation reaching the detector, a suitable description how this radiation is created as well as how it changes as it propagates through the atmosphere is required. A common approach in radiative transfer theory is to distinguish three fundamental types of such interactions of radiation with matter: The emission of radiation, its absorption, and the scattering of radiation away from and into its propagation path.

Emission

At temperatures above absolute zero, all matter emits radiation through the process of thermal emission. Thermal emission occurs when matter transitions from a quantum mechanical state of higher energy to one of lower energy which causes the surplus of energy to be emitted in the form of radiation. When considering radiation in the lower atmosphere, the relevant emitters of radiation are the ocean or land surface as well as gas molecules or suspended particles.

A fundamental concept for the description of emission is that of a black body. A black body is a piece of matter that absorbs all incoming radiation. At a given temperature T , the emission of a black body is isotropic and un-polarized. Its spectral intensity is given by Planck's law:

$$B_\nu(\nu, T) = \frac{2h\nu^3}{c^2} \frac{1}{\exp(\frac{h\nu}{k_B T}) - 1} \quad (3.3)$$

where c is the speed of light in the medium, h is the Planck constant and k_B is the Boltzmann constant. The Stokes vector describing the emission from a black body is

given by

$$\mathbf{I} = \begin{bmatrix} B_\nu \\ 0 \\ 0 \\ 0 \end{bmatrix}. \quad (3.4)$$

The concept of the black body is used to define the emission from other forms of matter using the emissivity vector $\boldsymbol{\epsilon}$:

$$\mathbf{I} = \boldsymbol{\epsilon} \cdot B_\nu \quad (3.5)$$

The main difference between the treatment of emission from a volume compared to that of a surface is the unit of the emission vector $\boldsymbol{\epsilon}$. For a volume, it is defined per unit length of the path through the volume, while for a surface this is not necessary. Due to the distinct orientation that surfaces have with respect to the viewing geometry, the emissivity vector generally depends on the emission angle. For particles this is generally also the case, but since most particles in the atmosphere are randomly oriented it is often neglected. Although black-body radiation is unpolarized, emission from general emitters can be polarized. An important example is the ocean surface, which is highly polarized around the Brewster angle at 53°.

Absorption

Absorption refers to the process of radiation being converted into internal energy of the matter it interacts with. Mathematically, this process is described by the absorption vector $\boldsymbol{\alpha}$, defined as the fraction of the incoming radiation that is absorbed along an infinitesimal distance ds along the propagation path:

$$\mathbf{I}_{\text{absorbed}} = (\boldsymbol{\alpha} \cdot ds) \odot \mathbf{I} \quad (3.6)$$

Here \odot denotes the element-wise product of the absorption vector and the Stokes vector \mathbf{I} of the incoming radiation. Absorption may be understood as the inverse process of thermal emission. Formally, this is expressed by Kirhoff's law of radiation

$$\boldsymbol{\alpha} = \boldsymbol{\epsilon}, \quad (3.7)$$

which states that the absorption vector is identical to the emissivity vector defined in Eq. 3.5. This law is applicable to all matter in the atmosphere given that it is in a state of local thermal equilibrium (LTE). LTE occurs when the density of matter is sufficiently high so that the population rates of energy states above the ground state are determined by thermal collisions rather than the absorption of radiation. This decouples the emission of radiation from the radiation field, allowing the simplified treatment of matter as thermal emitters with the emission rates independent of the radiation field. LTE is a valid assumption for radiative transfer in the lower atmosphere.

Scattering

When a beam of radiation impinges upon a particle, their interaction may cause a deviation of parts of the beam from the original propagation path. To first order, scattering decreases the intensity of the beam. This particular process is referred to as single scattering. As it propagates through the atmosphere, the intensity of a beam is decreased by the effects of absorption and single scattering. The combination of these two processes is referred to as attenuation or extinction. As the rate of scattering increases, also the effect radiation that is being scattered into the beam has to be taken into account.

Mathematically, the scattering of a beam of light propagating in direction \mathbf{n} into the direction $\hat{\mathbf{n}}$ is described by the phase matrix $\mathbf{Z}(\hat{\mathbf{n}}, \mathbf{n})$:

$$\mathbf{I}_{\text{scattered}}(\hat{\mathbf{n}}) = \mathbf{Z}(\hat{\mathbf{n}}, \mathbf{n})\mathbf{I}(\mathbf{n}) \quad (3.8)$$

The combined, attenuating effects of scattering and absorption are given by the attenuation matrix \mathbf{K} , which is the sum of the absorption vector $\boldsymbol{\alpha}$ and the fraction of radiation scattered away from the propagation path:

$$\mathbf{K} = \begin{bmatrix} | & | & | & | \\ \boldsymbol{\alpha} & \mathbf{0} & \mathbf{0} & \mathbf{0} \\ | & | & | & | \end{bmatrix} + \int_{\hat{\mathbf{n}}} d\hat{\mathbf{n}} \mathbf{Z}(\hat{\mathbf{n}}, \mathbf{n}) \quad (3.9)$$

3.1.2 The radiative transfer equation

The previous section introduced the fundamental interactions of radiation with matter and how they are described mathematically in radiative transfer theory. Combining the three processes of emission, absorption and scattering, the change that a beam undergoes as it travels a distance ds along its propagation path through the atmosphere is described the vector radiative transfer equation (VRTE):

$$\frac{d\mathbf{I}(\mathbf{n})}{ds} = -\mathbf{K}\mathbf{I}(\mathbf{n}) + \boldsymbol{\alpha} \cdot \mathbf{B}_\nu(T) + \int_{\hat{\mathbf{n}}} d\hat{\mathbf{n}} \mathbf{Z}(\mathbf{n}, \hat{\mathbf{n}})\mathbf{I}(\hat{\mathbf{n}}). \quad (3.10)$$

The radiation field for an arbitrary atmosphere can be computed by solving Equation (3.10). What is required for this are the values of temperature, absorption vector $\boldsymbol{\alpha}$ and phase matrices \mathbf{Z} throughout the atmosphere as well as a suitable method for solving the radiative transfer equation. The values of $\boldsymbol{\alpha}$ and \mathbf{Z} describe how a specific volume element of the atmosphere absorbs and scatters radiation. Their values therefore depend on the concentrations of gases and particulate matter in the atmosphere.

Approximate values of $\boldsymbol{\alpha}$ and \mathbf{Z} for different materials in the atmosphere can be measured experimentally or in special cases even derived from first principles. Typically they depend on local properties of the atmosphere such as temperature, pressure or concentration of gases or particles. Numerical models for $\boldsymbol{\alpha}$ and \mathbf{Z} together with the VRTE thus allow the radiation field observed by remote sensing instruments to be related to the state of the atmosphere. Together with the methods described in Section 4, this forms the basis of atmospheric remote sensing.

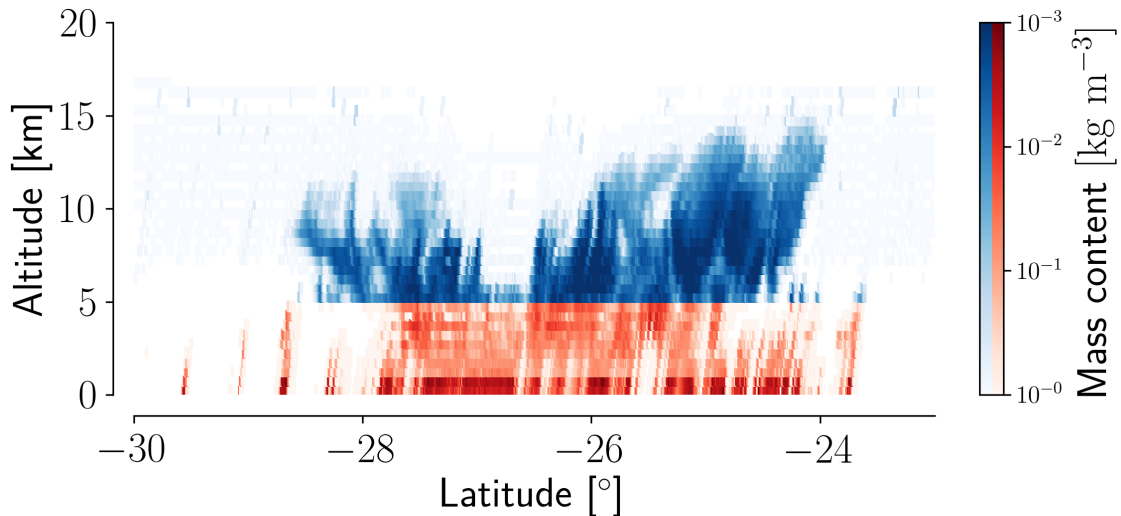


Figure 3.1: Mass content of frozen (blue) and liquid hydrometeors retrieved from the radar reflectivities show in Fig. 1.2

3.2 Microwave observations of clouds and precipitation

To illustrate the application of radiative transfer theory to observations of clouds and precipitation, we now turn back to the example cloud scene considered in Sec. 1.3. A simple hydrometeor retrieval has been performed to estimate the mass concentrations of frozen and liquid hydrometeors in the observed cloud using the radar observations displayed in Fig. 1.2. For simplicity, it was assumed that all hydrometeors below (in altitude) the $0\text{ }^{\circ}\text{C}$ -isotherm are in the liquid phase and the ones above in the ice phase. The retrieved mass concentrations are displayed in Fig. 3.1. Since a standard tropical atmosphere has been assumed to retrieve the cloud properties, the melting layer and hence the boundary between liquid and ice hydrometeors is at a constant altitude across the whole scene. Although this is certainly not a very accurate assumption especially since the radar reflectivities show signs of convective activity, it is sufficient to illustrate the basic interaction of microwave radiation with clouds and precipitation. The simplified cloud model obtained in this way is can now by used to simulate the signatures of liquid and frozen hydrometeors in the passive microwave observations.

3.2.1 Liquid hydrometeors

We start by investigating the effect of liquid hydrometeors on passive microwave observations. For this, all frozen hydrometeors in the scene are ignored and observations are simulated of the four passive microwave frequencies considered in Fig. 1.2. The results of these simulations are displayed in Fig. 3.2. Shown is the signal from clouds and precipitation defined as the difference in the simulated microwave signal

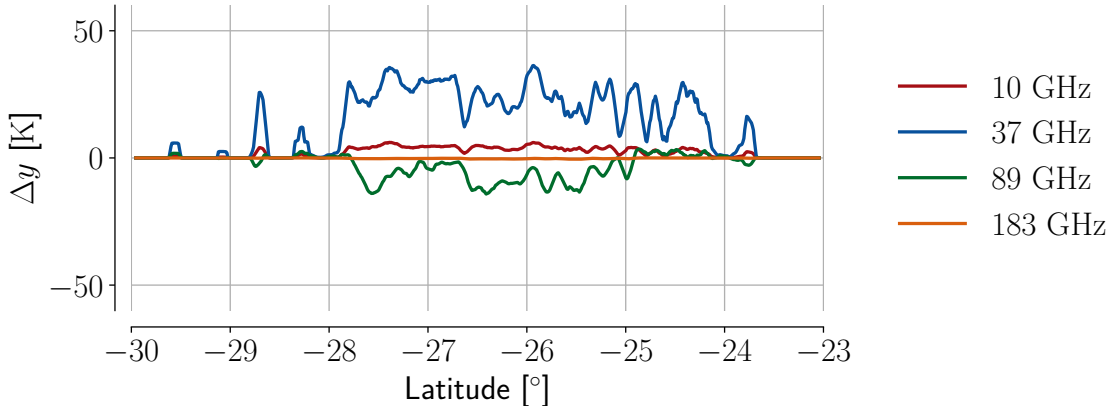


Figure 3.2: Simulated differences in observed passive radiances with respect to a cloud-free reference observation Δy for different microwave frequencies when only liquid hydrometeors are considered.

with respect to a cloud-free reference observation:

$$\Delta y = y_{\text{cloudy}} - y_{\text{clear}} \quad (3.11)$$

At frequencies as low as 10 GHz, the signal observed from the rain is positive. At these frequencies, rain drops interact with radiation mostly through absorption. Above the sea surface, which acts as a cold background, the rain is therefore observed as a warm signal. At 37 GHz, an even stronger positive signal is observed from the precipitation. The increase in the strength of the signal is due to the increased absorption at shorter wavelengths. As the frequency is increased to 89 GHz, the precipitation signal switches sign from positive to negative. This is because the sensitivity to water vapor causes the background to become warmer, while at the same time the rain drops become more effective scatters. The observed rain signal is therefore due to radiation that is being scattered away from the line of sight by the rain drops, leading to a negative signal.

At 183 GHz, finally, the precipitation signal has fully disappeared. This is because these frequencies the sensitivity to water vapor is so high that the sensor is essentially blind to the lower parts of the troposphere in which the rain is located.

3.2.2 Frozen hydrometeors

To now assess the additional effects of frozen hydrometeors, the simulations are run once again but this time including also the frozen hydrometeors in the simulations. The resulting cloud signals are displayed in Fig. 3.3.

First of all, it can be noticed that the precipitations signals observed at 10 GHz and 37 GHz are not affected by the presence of frozen hydrometeors. Although frozen precipitating particles are of similar sizes as rain drops, differences in their dielectric constants cause the ice to interact less strongly with the radiation than water. At 89 and 183 GHz, however, a clear negative signal from the ice particles is observed. At 183 GHz, all of the observed cloud signal is due to the scattering from frozen hydrometeors.

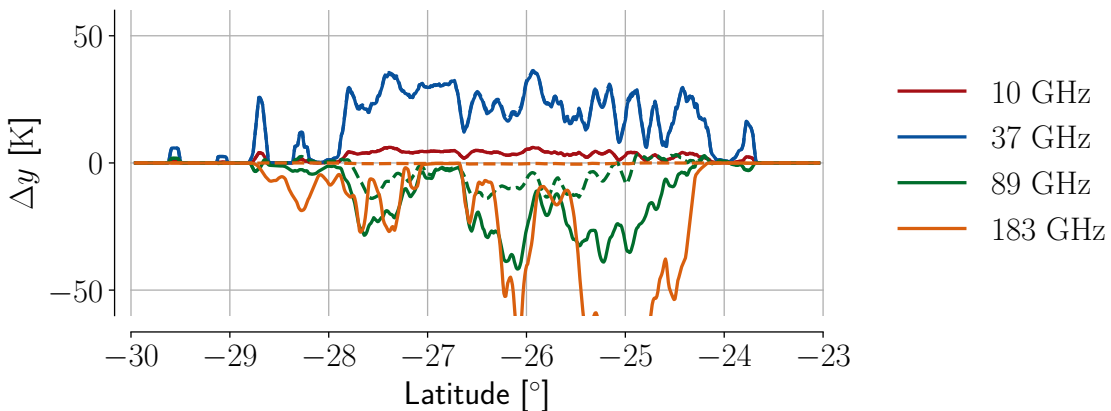


Figure 3.3: Simulated differences in observed passive radiances with respect to a cloud-free reference observation Δy when both liquid and frozen hydrometeors are considered. Dashed lines show the corresponding signal due to rain only (c.f. Fig. 3.2).

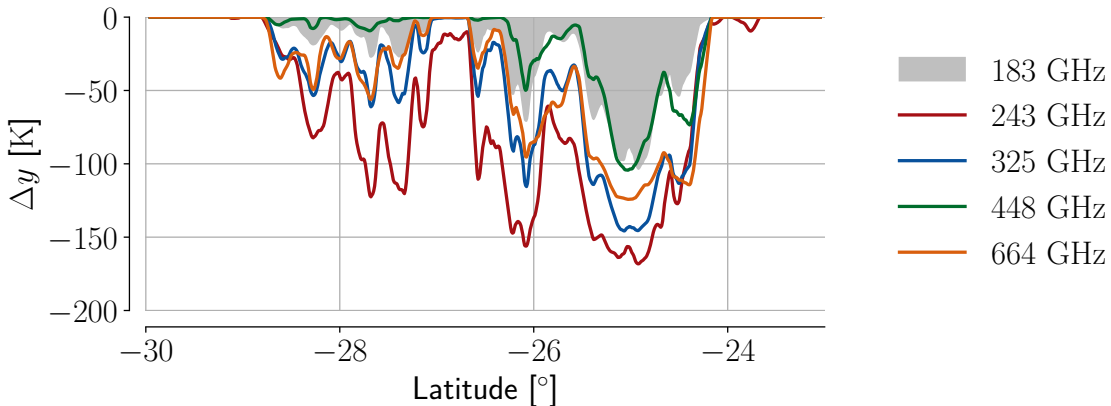


Figure 3.4: Signature of clouds in microwave observations. The plot shows the simulated cloud signal as it would be observed by the reference observation when both liquid and frozen hydrometeors are considered.

3.2.3 Sub-millimeter wavelengths

Finally, the simple cloud model can be used to demonstrate the benefits of sub-millimeter wavelengths for cloud observations. For this, we consider the cloud signal observed by four of the channels of the upcoming ICI instrument located at 248, 325, 448 and 664 GHz. The simulated cloud signals are displayed in Fig. 3.4. The cloud signal in all of the considered channels is considerably stronger than that at 183 GHz. In particular in the left part of the scene, the cloud signals at sub-millimeter wavelength are significantly stronger than that observed at 183 GHz. Since observations at 183 GHz are sensitive only to particles large enough to be considered snow, the signal observed here indicates the presence ice clouds. This shows that ICI will bring immense benefits for observations of clouds using microwave radiation.

Chapter 4

Inverse problems

The previous chapters provided an overview over the general properties of clouds and their interaction with electromagnetic radiation which is used to observe them. This chapter describes the mathematical methods that are used to infer properties of clouds from their signatures in the observed electromagnetic radiation. Mathematically, this task is formulated as an inverse problem. This is because inferring the cloud properties from observations can be viewed as the inverse of the problem of predicting the observations given the cloud properties, which is referred to as the forward problem. How the forward problem can be solved using radiative transfer theory has been described in the previous chapter. In this chapter we now turn to the task of solving the inverse problem.

4.1 Formulation

Mathematically, the general inverse problem of remote sensing is formulated as follows: Let $\mathbf{x} \in \mathbb{R}^n$ be an arbitrary vector that describes the state of the atmosphere. The vector space of all possible states is referred to as the state space and for simplicity assumed to be given by \mathbb{R}^n . The state atmospheric state \mathbf{x} is observed through an observations system, which produces the observation vector $\mathbf{y} \in \mathbb{R}^m$. Furthermore, it is assumed here that a forward model $\mathbf{F} : \mathbb{R}^n \rightarrow \mathbb{R}^m$ exists that allows computing the observation $\mathbf{y} = \mathbf{F}(\mathbf{x})$ corresponding to any given state vector \mathbf{x} . The inverse problem consists of determining the state vector \mathbf{x} corresponding to a given the observation vector \mathbf{y} , hence to invert the forward model \mathbf{F} .

The general difficulty with inverse problems is that they do not admit a unique solution. This is because, at least in atmospheric remote sensing, the problem is generally underconstrained. This means that the amount of information in the observations \mathbf{y} is not sufficient to uniquely determine a state \mathbf{x} . Examples are different cloud configurations that result in the same measurement vector such as for example a low-level cloud covered by an opaque high-level cloud. From the measurement vector \mathbf{y} alone it is impossible to determine a unique state \mathbf{x} as it will be the same independent of the presence or properties of the low-level cloud.

Simultaneously to being underconstrained, the problem may be overconstrained. This happens when different components of the measurement vector provide seemingly

contradictory information on the measurement state \mathbf{x} due errors random errors in \mathbf{y} .

4.2 Solution

A common approach in atmospheric remote sensing to solve inverse problems is the application of Bayesian statistics. This means that instead of searching a unique solution to the inverse problem, the solution is found in the form of a probability distribution that describes how likely it is that any of the elements of the state space has produced a given observation \mathbf{y} .

The approach that will be presented in the following is known as the optimal estimation method (OEM, Rodgers (2000)). The method makes three basic assumptions in order to solve the inverse problem:

1. That the forward model \mathbf{F} is linear or at most weakly non-linear,
2. that the knowledge available about \mathbf{x} can be described by a Gaussian distribution, with mean \mathbf{x}_a and covariance matrix \mathbf{S}_a^{-1}
3. that the errors affecting \mathbf{y} are Gaussian with covariance matrix \mathbf{S}_ϵ .

Under these assumptions, both the a priori distribution for \mathbf{x} as well as the conditional probability of observing the measurement \mathbf{y} given the state \mathbf{x} are Gaussian:

$$p(\mathbf{x}) = \frac{1}{(2\pi)^{\frac{-n}{2}} \det(\mathbf{S}_a)^{-\frac{1}{2}}} \exp \left\{ -\frac{1}{2} (\mathbf{x} - \mathbf{x}_a)^T \mathbf{S}_a^{-1} (\mathbf{x} - \mathbf{x}_a) \right\} \quad (4.1)$$

$$p(\mathbf{y}|\mathbf{x}) = \frac{1}{(2\pi)^{\frac{-m}{2}} \det(\mathbf{S}_e)^{-\frac{1}{2}}} \exp \left\{ -\frac{1}{2} (\mathbf{y} - \mathbf{F}(\mathbf{x}))^T \mathbf{S}_e^{-1} (\mathbf{y} - \mathbf{F}(\mathbf{x})) \right\} \quad (4.2)$$

In the Bayesian framework the solution of the inverse problem is simply the a posteriori distribution $p(\mathbf{x}|\mathbf{y})$ of \mathbf{x} given the observation vector \mathbf{y} . It is found by applying Bayes theorem

$$p(\mathbf{y}|\mathbf{x}) = \frac{p(\mathbf{y}|\mathbf{x})p(\mathbf{x})}{p(\mathbf{y})} \quad (4.3)$$

$$\propto p(\mathbf{y}|\mathbf{x})p(\mathbf{x}) \quad (4.4)$$

to the probabilities (4.1) and (4.2).

As a specific solution of the retrieval problem, generally the most likely state is chosen, denoted as the maximum a posteriori (MAP) estimator for \mathbf{x} . It can be found by minimizing the log-likelihood of the posterior distribution, which has the form:

$$-\mathcal{L} \propto (\mathbf{F}(\mathbf{x}) - \mathbf{y})^T \mathbf{S}_\epsilon^{-1} (\mathbf{F}(\mathbf{x}) - \mathbf{y}) + (\mathbf{x} - \mathbf{x}_a)^T \mathbf{S}_a^{-1} (\mathbf{x} - \mathbf{x}_a) \quad (4.5)$$

Solving the retrieval problem has thus been reduced to minimizing the negative log-likelihood of the posterior distribution. When the forward model is non-linear, minimizing Eq. (4.5) must be performed iteratively using suitable optimization methods such as the Gauss-Newton or Levenberg-Marquardt methods (Boyd and Vandenberghe 2004).

4.3 Error estimation

A major advantage of the OEM formalism is that it allows precise characterization of the errors that affect the retrieved state. Given below is a derivation of the retrieval error from the formulation of the OEM for a linear forward model and in the absence of forward model errors. How these results can be generalized to a non-linear forward model and the presence of forward modeling errors are outlined afterwards.

4.3.1 The idealized case

We start by defining a retrieval operator $\hat{\mathbf{x}} = \mathbf{R}(\mathbf{y})$ which represents the application of the retrieval to an observation vector \mathbf{y} yielding the retrieved state $\hat{\mathbf{x}}$. If the forward model is assumed to be exact, then \mathbf{y} can be written as the sum of the forward model evaluated at the true state \mathbf{x} and a random vector of measurement noise:

$$\mathbf{y} = \mathbf{F}(\mathbf{x}) + \boldsymbol{\epsilon}. \quad (4.6)$$

Inserting this into \mathbf{R} and linearizing the forward model \mathbf{F} about the a priori state \mathbf{x}_a yields

$$\mathbf{R}(\mathbf{y}) = \mathbf{R}(\mathbf{F}(\mathbf{x}_a) + \mathbf{K}(\mathbf{x} - \mathbf{x}_a) + \boldsymbol{\epsilon}), \quad (4.7)$$

where $\mathbf{K} = \frac{d\mathbf{F}}{d\mathbf{x}}$ is the Jacobian of the forward model. Now, linearizing the retrieval operator about \mathbf{y} allows us to write

$$\hat{\mathbf{x}} = \mathbf{R}(\mathbf{F}(\mathbf{x}_a)) + \frac{d\mathbf{R}}{d\mathbf{x}} \mathbf{K}(\mathbf{x} - \mathbf{x}_a) + \frac{d\mathbf{R}}{d\mathbf{x}} \boldsymbol{\epsilon}. \quad (4.8)$$

Assuming an unbiased retrieval operator, i.e. $\mathbf{R}(\mathbf{F}(\mathbf{x})) - \mathbf{x}_a = 0$, the retrieved information on the state \mathbf{x} may be written as

$$\hat{\mathbf{x}} - \mathbf{x}_a = \frac{d\mathbf{R}}{d\mathbf{x}} \mathbf{K}(\mathbf{x} - \mathbf{x}_a) + \frac{d\mathbf{R}}{d\mathbf{x}} \boldsymbol{\epsilon}. \quad (4.9)$$

The derivative of the retrieval operator \mathbf{R} with respect to the observation vector \mathbf{y} is referred to as the gain matrix \mathbf{G} and is found to be given by

$$\mathbf{G} = (\mathbf{K}^T \mathbf{S}_\epsilon^{-1} \mathbf{K} + \mathbf{S}_a^{-1})^{-1} \mathbf{K}^T \mathbf{S}_\epsilon^{-1}. \quad (4.10)$$

We further define the so-called averaging kernel matrix $\mathbf{A} = \mathbf{GK}$. With this, the retrieval error can be written as

$$\hat{\mathbf{x}} - \mathbf{x} = \underbrace{(\mathbf{A} - \mathbf{I})(\mathbf{x} - \mathbf{x}_a)}_{\text{Smoothing error}} + \underbrace{\frac{d\mathbf{R}}{d\mathbf{x}} \boldsymbol{\epsilon}}_{\text{Error due to noise}}. \quad (4.11)$$

This shows that the retrieval error can be written as the sum of two contributions. The first term on the right hand side is the so called smoothing error. It can be

interpreted as the retrieval error that occurs because of the limited resolution of the observation system. Its covariance matrix is given by

$$\mathbf{S}_s = (\mathbf{A} - \mathbf{I})\mathbf{S}_\epsilon(\mathbf{A} - \mathbf{I}). \quad (4.12)$$

The second term on the right-hand side of Eq. (4.11) is the error caused by the noise in the observations. Its covariance matrix is given by

$$\mathbf{S}_m = \mathbf{G}_y \mathbf{S}_\epsilon \mathbf{G}_y^T. \quad (4.13)$$

4.3.2 Handling forward model error and non-linearity

The derivation presented above assumed an ideal forward model, which is of course rarely the case in reality. It is possible to generalize the formulation of the retrieval error, if the forward model error can be assumed to be bias free and described using a Gaussian distribution with covariance matrix \mathbf{S}_e . In this case the general retrieval error can be obtained by simply replacing \mathbf{S}_ϵ in Eq. (4.13) with $\mathbf{S}_\epsilon + \mathbf{S}_e$.

If the forward model is non-linear, the forward model in the above derivation has to be linearized about the most recent state in the retrieval iteration \mathbf{x}_i . In this case the bias term $\mathbf{R}(\mathbf{F}(\mathbf{x}_i)) - \mathbf{x}_a$ can no longer be assumed to be zero, and the retrieval results will become biased.

Chapter 5

Summary of appended papers and outlook

After introducing the physical and mathematical principles of the remote sensing of clouds, this chapter now turns towards the research that has been carried out under the general aim of preparations for the upcoming ICI sensor. The two scientific articles appended to this thesis investigate the concept of combining radar and radiometer observations for retrieving ice hydrometeors. The studies were carried out within the context of the study “Scientific Concept Study for Wide-Swath High-Resolution Cloud Profiling” funded by the European Space Agency which investigated the potential benefits of a hypothetical cloud radar mission flying in constellation with ICI to provide co-located radar and sub-millimeter radiometer observations.

5.1 Paper A: Synergistic radar and radiometer retrievals of ice hydrometeors

A synergistic retrieval algorithm is proposed which uses the OEM to retrieve ice hydrometeors from combined radar and sub-millimeter radiometer observations. The study aims to establish the fundamental synergies of the combined observations, i.e. the additional information that can be gained from the observations when they are used simultaneously in the retrieval instead of considering them separately.

5.1.1 Data and methods

The study uses simulated observations from a high-resolution atmospheric model to produce synthetic, co-located observations from a cloud radar and a sub-millimeter radiometer. By applying the retrieval to these synthetic observations its performance is assessed. The combined retrieval is compared to radar-only and passive-only versions of the retrieval algorithm to establish the advantages of the synergistic retrieval approach.

5.1.2 Results

The results obtained in this study show the combination of radar and radiometer observations helps to better constrain the microphysical properties of clouds. The increased sensitivity to microphysical properties of the cloud reduces uncertainties in retrieved ice mass concentrations. In addition to that, the combined retrieval showed improved skill in the detection and retrieval of liquid clouds.

5.1.3 Conclusions

The increased information content of the combined observations allows an additional degree of freedom of the distribution of ice hydrometeors to be retrieved, which helps to reduce uncertainties in the retrieved ice mass concentrations. This information gain could be attributed to the sub-millimeter channels of the ICI sensor. It is therefore concluded that combined retrievals involving radar and sub-millimeter radiometer observations are a promising approach that may help to reduce uncertainties in retrievals of frozen hydrometeors.

5.2 Paper B: Relating microphysical and radiometric properties of cloud hydrometeors at millimeter and sub-millimeter wavelengths

The second paper builds upon the first one by applying the synergistic retrieval algorithm to observations from a recent flight campaign. One of the few currently available sensors that can produce ICI-type sub-millimeter observations of clouds is the International Submillimetre Airborne Radiometer (ISMAR, Fox et al. (2017)), which serves as the airborne demonstrator for the ICI sensor. In 2016, ISMAR took part in a joint flight campaign in which three research aircraft performed a simultaneous overpass of a mid-latitude cloud system and observed it using a wide range of remote sensing sensors. Since cloud radars were present on the other two aircraft, the observations made during the campaign provide a unique opportunity to apply and test the synergistic retrieval algorithm.

5.2.1 Data and method

The study uses observations acquired by the joint flight of the High Altitude and Long Range Research Aircraft (HALO), the Facility for Airborne Atmospheric Measurements (FAAM) and the Service des Avions Francais Instrumentations pour la Recherche en Environnement (SAFIRE) research aircraft. The data consists of remote sensing observations from the overpass and in-situ data collected by the FAAM aircraft.

The in-situ data available from the flight are used to characterize the microphysical properties of the hydrometeors in the observed cloud. Since assumption on these

properties affect the results of the retrieval, this characterization is necessary for their analysis.

Following this, the synergistic retrieval algorithm is applied to the observations from the flight. The fits of the forward model to the observations are evaluated to check the consistency of the radiative transfer modeling upon which the retrieval is based. The retrieved hydrometeor profiles are compared to those derived from the in-situ data. Finally, the consistency of the retrieved hydrometeor distributions with the other observations from the flight is assessed by comparing them to simulations obtained from the retrieval results.

5.2.2 Results

An important result of this study is that the retrieval does achieve a good fit to the observations over large parts of the scene, which shows that the applied radiative transfer scheme is able to consistently model the observations over the wide range of microwave frequencies that was considered here. Two regions in which the retrieval does not fit the observations show signs of convective activity indicating the presence of a signal from the specific microphysical properties of the hydrometeors in the updraft.

Although dependent on the employed particle model, the retrieval results show generally good agreement with the in-situ measurements. This dependency, however, is found to be consistent with the microphysical characterization derived from the in-situ measurements, which speaks in favor of the validity of the retrieval method. Moreover, the simulated observations of an additional radar operating at a different frequency show good agreement with the real observations.

5.2.3 Conclusions

The results presented in this study validate the implementation of the developed synergistic retrieval algorithm and thus confirm the results from the first study. Moreover, the good fit to the observations obtained in the retrieval demonstrates the consistency of the radiative transfer modeling through clouds at millimeter and sub-millimeter wavelengths. The results therefore provide an important validation case for the modeling of radiative transfer at sub-millimeter wavelengths.

5.3 Outlook

5.3.1 Relevance of the results

The focus of the presented research were combined retrievals using radar and sub-millimeter radiometer observations. Since such observation are currently not available from any ongoing satellite missions, this research is relevant to prospective satellite missions involving radar and sub-millimeter observations. In addition to that, the second study demonstrated the usefulness of the approach also for the application in

field campaigns where it may be used to validate the radiative transfer modeling of clouds and possibly even to study their microphysical properties.

The presented results also have a more general relevance with respect to the upcoming ICI mission. Since currently available sub-millimeter observations of clouds are limited, the radiative transfer modeling at these frequencies is still afflicted with considerable uncertainties. These uncertainties will need to be addressed in order to put the observations from ICI to proper use. The application of the combined retrieval described in Paper B validated the radiative transfer modeling at sub-millimeter wavelengths but also highlighted remaining modeling issues regarding the properties of hydrometeors in regions of strong convective activity.

5.3.2 Future work

Although the presented work established the basic consistency of radiative transfer modeling of clouds at sub-millimeter wavelengths, there remain a number of challenges that should be addressed. One of them is certainly the representation of the ice particles in radiative transfer simulations at sub-millimeter wavelengths. This could be further investigated by making use of other field campaigns involving the ISMAR radiometer. Alternatively, co-locations of currently available satellite observations could be used as has been attempted in ekelund19. This work could be further extended by including infrared observations and by using directly co-located observations such as the ones shown in Sec. 1.3.

A more specific line of future work that arises from the results of the second study is to investigate the radiometric properties of hydrometeors in convective updrafts. The observations from the flight campaign could serve as a case study to establish the basic radiometric properties of the hydrometeors present in these updrafts. These could then be used to investigate the effect of the derived properties on already available microwave observations of clouds.

Finally, since the ability to model the radiative transfer at sub-millimeter wavelengths is the foundation for understanding and making use of the observations that will be provided by ICI, the general consolidation of radiative transfer models at sub-millimeter wavelengths remains an essential issue. An important resource for this are the air-borne observations from the ISMAR sensor, which should be used for continued validation studies for the radiative transfer modeling at these wavelengths.

Bibliography

- Bony, S., B. Stevens, D. M. Frierson, C. Jakob, M. Kageyama, R. Pincus, T. G. Shepherd, S. C. Sherwood, A. P. Siebesma, A. H. Sobel, et al. (2015). “Clouds, circulation and climate sensitivity”. In: *Nat. Geosci.* 8.4, p. 261 (cit. on p. 5).
- Boucher, O., D. Randall, P. Artaxo, C. Bretherton, G. Feingold, P. Forster, V.-M. Kerminen, Y. Kondo, H. Liao, U. Lohmann, P. Rasch, S. Satheesh, S. Sherwood, B. Stevens, and X. Zhang (2013). “Clouds and Aerosols”. In: *Climate Change 2013: The Physical Science Basis. Contribution of Working Group I to the Fifth Assessment Report of the Intergovernmental Panel on Climate Change*. Ed. by T. Stocker, D. Qin, G.-K. Plattner, M. Tignor, S. Allen, J. Boschung, A. Nauels, Y. Xia, V. Bex, and P. Midgley. Cambridge, United Kingdom and New York, NY, USA: Cambridge University Press. Chap. 7, pp. 571–658. ISBN: ISBN 978-1-107-66182-0. DOI: [10.1017/CBO9781107415324.016](https://doi.org/10.1017/CBO9781107415324.016) (cit. on p. 5).
- Boyd, S. and L. Vandenberghe (2004). *Convex optimization*. Cambridge university press (cit. on p. 26).
- Buehler, S., E. Defer, F. Evans, S. Eliasson, J. Mendrok, P. Eriksson, C. Lee, C. Jiménez, C. Prigent, S. Crewell, et al. (2012). “Observing ice clouds in the submillimeter spectral range: the CloudIce mission proposal for ESA’s Earth Explorer 8”. In: *Atmos. Meas. Tech.* 5.7, pp. 1529–1549 (cit. on p. 8).
- Collins, M., R. Knutti, J. Arblaster, J.-L. Dufresne, T. Fichefet, P. Friedlingstein, X. Gao, W. Gutowski, T. Johns, G. Krinner, M. Shongwe, C. Tebaldi, A. Weaver, and M. Wehner (2013). “Long-term Climate Change: Projections, Commitments and Irreversibility”. In: *Climate Change 2013: The Physical Science Basis. Contribution of Working Group I to the Fifth Assessment Report of the Intergovernmental Panel on Climate Change*. Ed. by T. Stocker, D. Qin, G.-K. Plattner, M. Tignor, S. Allen, J. Boschung, A. Nauels, Y. Xia, V. Bex, and P. Midgley. Cambridge, United Kingdom and New York, NY, USA: Cambridge University Press. Chap. 12, pp. 1029–1136. ISBN: ISBN 978-1-107-66182-0. DOI: [10.1017/CBO9781107415324.024](https://doi.org/10.1017/CBO9781107415324.024) (cit. on p. 3).
- Coronese, M., F. Lamperti, K. Keller, F. Chiaromonte, and A. Roventini (2019). “Evidence for sharp increase in the economic damages of extreme natural disasters”. In: *Proceedings of the National Academy of Sciences* 116.43, pp. 21450–21455. ISSN: 0027-8424. DOI: [10.1073/pnas.1907826116](https://doi.org/10.1073/pnas.1907826116) (cit. on p. 3).
- Draper, D. W., N. D. A., F. J. Wentz, S. Krimchansky, and G. M. Skofronick-Jackson (2015). “The Global Precipitation Measurement (GPM) Microwave Imager (GMI): Instrument Overview and Early On-Orbit Performance”. In: *IEEE Journal of*

- Selected Topics in Applied Earth Observations and Remote Sensing* 8.7, pp. 3452–3462. ISSN: 2151-1535. DOI: 10.1109/JSTARS.2015.2403303 (cit. on p. 7).
- Fox, S., C. Lee, B. Moyna, M. Philipp, I. Rule, S. Rogers, R. King, M. Oldfield, S. Rea, M. Henry, H. Wang, and R. C. Harlow (2017). “ISMAR: an airborne submillimetre radiometer”. In: *Atmos. Meas. Tech.* 10.2, pp. 477–490. DOI: 10.5194/amt-10-477-2017 (cit. on p. 30).
- Geer, A. J., F. Baordo, N. Bormann, P. Chambon, S. J. English, M. Kazumori, H. Lawrence, P. Lean, K. Lonitz, and C. Lupu (2017). “The growing impact of satellite observations sensitive to humidity, cloud and precipitation”. In: *Q. J. R. Meteorol. Soc.* 143.709, pp. 3189–3206. DOI: 10.1002/qj.3172 (cit. on p. 4).
- Geer, A. J., K. Lonitz, P. Weston, M. Kazumori, K. Okamoto, Y. Zhu, E. H. Liu, A. Collard, W. Bell, S. Migliorini, P. Chambon, N. Fourrié, M.-J. Kim, C. Köpkens-Watts, and C. Schraff (2018). “All-sky satellite data assimilation at operational weather forecasting centres”. In: *Q. J. R. Meteorol. Soc.* 144.713, pp. 1191–1217. DOI: 10.1002/qj.3202 (cit. on p. 4).
- Grinsted, A., P. Ditlevsen, and J. H. Christensen (2019). “Normalized US hurricane damage estimates using area of total destruction, 1900–2018”. In: *Proceedings of the National Academy of Sciences*. ISSN: 0027-8424. DOI: 10.1073/pnas.1912277116 (cit. on p. 3).
- Hellmann, G. (1908). “The dawn of meteorology”. In: *Quarterly Journal of the Royal Meteorological Society* 34.148, pp. 221–232. DOI: 10.1002/qj.49703414802 (cit. on p. 3).
- Köhler, H. (1936). “The nucleus in and the growth of hygroscopic droplets”. In: *Transactions of the Faraday Society* 32, pp. 1152–1161 (cit. on p. 13).
- Lohmann, U., F. Lüönd, and F. Mahrt (2016). *An introduction to clouds: From the microscale to climate*. Cambridge University Press (cit. on pp. 11, 12, 14).
- Masson-Delmotte, V., M. Schulz, A. Abe-Ouchi, J. Beer, A. Ganopolski, J. González Rouco, E. Jansen, K. Lambeck, J. Luterbacher, T. Naish, T. Osborn, B. Otto-Btiesner, T. Quinn, R. Ramesh, M. Rojas, X. Shao, and A. Timmermann (2013). “Information from Paleoclimate Archives”. In: *Climate Change 2013: The Physical Science Basis. Contribution of Working Group I to the Fifth Assessment Report of the Intergovernmental Panel on Climate Change*. Ed. by T. Stocker, D. Qin, G.-K. Plattner, M. Tignor, S. Allen, J. Boschung, A. Nauels, Y. Xia, V. Bex, and P. Midgley. Cambridge, United Kingdom and New York, NY, USA: Cambridge University Press. Chap. 5, pp. 383–464. ISBN: 978-1-107-66182-0. DOI: 10.1017/CBO9781107415324.013 (cit. on p. 3).
- Mishchenko, M. I., L. D. Travis, and A. A. Lacis (2002). *Scattering, absorption, and emission of light by small particles*. Cambridge university press (cit. on p. 17).
- Rodgers, C. D. (2000). *Inverse methods for atmospheric sounding: theory and practice*. Vol. 2. World scientific (cit. on p. 26).
- Tanelli, S., S. L. Durden, E. Im, K. S. Pak, D. G. Reinke, P. Partain, J. M. Haynes, and R. T. Marchand (2008). “CloudSat’s Cloud Profiling Radar After Two Years in Orbit: Performance, Calibration, and Processing”. In: *IEEE T. Geosci. Remote* 46.11, pp. 3560–3573. ISSN: 0196-2892. DOI: 10.1109/TGRS.2008.2002030 (cit. on p. 8).

- Thomas, G. E. and K. Stamnes (2002). *Radiative transfer in the atmosphere and ocean*. Cambridge University Press (cit. on p. 17).
- Wallace, J. M. and P. V. Hobbs (2006). *Atmospheric science: an introductory survey*. Vol. 92. Elsevier (cit. on p. 17).

Part II

Appended papers

Paper 1

Synergistic radar and radiometer retrievals of ice hydrometeors

S. Pfreundschuh, P. Eriksson, S. A. Buehler, M. Brath, D. Duncan, R. Larsson, R. Ekelund

Atmospheric Measurement Techniques Discussions

In review

Paper 1. Synergistic radar and radiometer retrievals of ice hydrometeors

S. Pfreundschuh, P. Eriksson, S. A. Buehler, M. Brath, D. Duncan, R. Larsson,
R. Ekelund

Synergistic radar and radiometer retrievals of ice hydrometeors

Simon Pfreundschuh¹, Patrick Eriksson¹, Stefan A. Buehler², Manfred Brath², David Duncan⁴, Richard Larsson³, and Robin Ekelund¹

¹Department of Space, Earth and Environment, Chalmers University of Technology, 41296 Gothenburg, Sweden

²Meteorologisches Institut, Fachbereich Geowissenschaften, Centrum für Erdsystem und Nachhaltigkeitsforschung (CEN), Universität Hamburg, Bundesstraße 55, 20146 Hamburg, Germany

³Max Planck Institute for Solar System Research, Justus-von-Liebig-Weg 3, 37077 Göttingen, Germany

⁴European Centre for Medium-Range Weather Forecasts, Shinfield Park, Reading RG2 9AX, United Kingdom

Correspondence: Simon Pfreundschuh (simon.pfreundschuh@chalmers.se)

Abstract. The upcoming Ice Cloud Imager (ICI) radiometer, to be launched on board the second generation of European operational meteorological satellites (Metop-SG), will be the first microwave imager to provide sub-millimeter observations of the atmosphere. The Microwave Imager (MWI) radiometer will be flown on the same satellites and complement the ICI sensor with observations at traditional millimeter wavelengths. The addition of these two new passive microwave sensors to the

5 global system of earth observation satellites opens up opportunities for synergistic satellite missions aiming to maximize the scientific return of the Metop-SG program. This study analyzes the potential benefits of combining observations of the MWI and ICI radiometers with a 94-GHz cloud radar for the retrieval of frozen hydrometeors. Starting from a simplified numerical experiment, it is shown that the complementary information content in the radar and radiometer observations can help to better constrain the particle size distribution of ice particles in the atmosphere. The feasibility of the combined retrieval is demonstrated by applying a one-dimensional, variational cloud-retrieval algorithm to simulated observations from a high-resolution atmospheric model. Comparison of the results with passive- and radar-only versions of the retrieval algorithm confirms that synergies between the active and passive observations allow an improved retrieval of microphysical properties of frozen hydrometeors. The effect of the assumed ice particle shape on the results is analyzed and found to be critical for obtaining good retrieval performance. In addition to this, the synergistic retrieval shows improved sensitivity to liquid water in both warm
10 and supercooled clouds. The results of this study clearly demonstrate the potential of the combined observations to constrain the microphysical properties of ice hydrometeors, which can help to reduce errors in retrieved profiles of mass- and number densities.

1 Introduction

Ice clouds play an important role in many weather- and climate-related processes in the atmosphere. They interact with incoming and outgoing radiation and thus influence the Earth's energy budget. Moreover, as part of the global hydrological cycle and due to their relation to the dynamics of the atmosphere (Bony et al., 2015), observations of ice clouds provide important information to constrain the state of the atmosphere in numerical weather prediction (NWP) models (Geer et al., 2017) as well as to validate predictions from climate models (Waliser et al., 2009).

Despite the importance of observations of ice clouds for climate and weather prediction, today's global observing system
25 cannot provide accurate information on the global distribution of ice in the atmosphere (Eliasson et al., 2011; Duncan and Eriksson, 2018). The main difficulty in sensing atmospheric ice from space is the large variability of sizes and concentrations in which ice particles occur in the atmosphere. The wide spectrum of ice crystal sizes, which ranges from micro- to millimeter scales, can only be partially resolved by currently available space-borne sensors.

The sensitivity of a remote sensing system to ice particles of a given size is determined mainly by its observing frequencies.
30 The scattering of radiation by ice particles is strongest for sizes roughly equal to the wavelength, λ , of the radiation. For particles with sizes much smaller than λ , the sensitivity decreases rapidly, making them practically invisible to the sensor. Although the strength of the interaction between particles and radiation decreases as the wavelength becomes much larger than the particle size, it remains strong enough for the cloud signal to saturate in the presence of thicker clouds, leading to loss of sensitivity further down the line of sight.

35 The observing frequencies that are currently available for measuring ice from space are limited to the microwave, infrared and optical domain. Infrared and optical sensors provide sensitivity to small ice particles but cannot sense significant parts of the ice mass of thicker clouds due to saturation of the signal. Microwave observations, in contrast, provide sensitivity throughout the whole atmospheric column but are insensitive to small ice particles. Although radars and lidars generally provide greater sensitivity than their passive counterparts, they are ultimately limited by the same principles.

40 To narrow the size-sensitivity gap between the infrared and traditional microwave sensors, the upcoming Ice Cloud Imager (ICI) will extend the microwave frequencies available for studying clouds with channels at 243, 325, 448 and 664 GHz (Eriksson et al., 2019). This extension of the smallest currently available microwave wavelength from 1.6 mm at 183 GHz down to the sub-millimeter domain (0.45 mm at 664 GHz) will significantly improve the size-sensitivity of space-borne microwave observations of clouds.

45 Together with ICI, also the newly developed Microwave Imager (MWI) will be flown on the satellites of the Metop-SG program. MWI will complement ICI's observations with measurements at traditional millimeter wavelengths. The observations of MWI, which cover the frequency range from 19 GHz up to 183 GHz, will provide additional sensitivity to liquid and frozen precipitation as well as water vapor.

The advent of space-borne sub-millimeter radiometry of clouds brings with it great potential for the study ice in the atmosphere.
50 The information content and retrieval performance from radiometer observations alone has been studied in detail for column-integrated ice mass (Jiménez et al., 2007; Wang et al., 2017; Brath et al., 2018) as well as for the vertical distribution of ice in the atmosphere (Birman et al., 2017; Grützun et al., 2018; Aires et al., 2019). Also the concept of combining millimeter and sub-millimeter radiometer observations with active observations from a cloud radar has been investigated (Evans et al., 2005; Jiang et al., 2019).

55 This work applies the concept of synergistic radar and sub-millimeter radiometer retrievals to the upcoming ICI and MWI sensors by combining them with a conceptual W-band cloud radar. It extends previous studies on this observational technique by providing an in-depth analysis of the fundamental synergies between the active and passive observations that help to improve the retrieval ice in the atmosphere. In particular, this study investigates to which extent the combined active and passive

observations can constrain the microphysics of ice particles in the atmosphere. Starting from a simplified numerical experiment,
60 the complementarity of the information content of the active and passive observations is demonstrated. In addition to this, simulated results from a synergistic, variational cloud-retrieval algorithm are presented. The algorithm is applied to synthetic observations of cloud scenes from a high-resolution atmospheric model and used to further explore the synergies between the active and passive observations.

The presented research has been conducted as part of a larger study funded by the European Space Agency, which evaluated
65 the concept of a future radar mission to fly in constellation with ICI on board the satellites of the Metop-SG program. Inspired by the concept of the Global Precipitation Measurement (GPM, Hou et al. (2014)) mission, the approach of this tentative mission is to perform vertically-resolved, high-accuracy retrievals of hydrometeors from the co-located active and passive observations at the swath center of the passive imager. The results of combined retrieval could then be used to constrain
70 passive-only profile retrievals with the aim of extending the profiling capabilities of the radar to the wide swath of the passive imager.

Following this introduction, Section 2 introduces the test data, sensor configuration and the developed retrieval algorithm on which the study is based. This is followed by the experimental results on the information content of the combined observations and the retrieval results of the joint retrieval on selected test scenes in Section 3. The article closes with a discussion of the results in Section 4 and conclusions in Section 5.

75 2 Methods and data

The synergistic retrieval is tested using simulated observations of cloud scenes from a high-resolution atmospheric circulation model. This section presents the selected reference cloud scenes, sensor configuration and basic modeling assumptions used in the radiative transfer simulations. In addition to this, the theoretical formulation of the combined cloud-retrieval algorithm is introduced.

80 2.1 Reference cloud scenes

The cloud scenes that will be used for the testing of the retrieval were produced by Environment and Climate Change Canada using a high-resolution NWP configuration of the Global Environmental Multiscale (GEM) Model (Côté et al. (1998)). For this study, we restrict ourselves to two designated, two-dimensional test scenes, which are displayed in Fig. 1. The test scenes have a horizontal resolution of 1 km and both extend over 800 km. The scenes were chosen with the aim of covering a large
85 range of cloud structures and compositions so as to ensure a realistic assessment of the retrieval. The first test scene, shown in panel (a), is located in the tropical Pacific and contains a convective storm system in the right half of the scene and its anvil that extends into the left half of the scene. The second scene, shown in panel (b), is located in the North Atlantic and contains an ice cloud in the first quarter and a low-level, mixed-phase cloud in the remainder of the scene.

The GEM model uses six types of hydrometeors to represent clouds and precipitation (Milbrandt and Yau, 2005): Two
90 classes of liquid hydrometeors (rain and liquid cloud) and four of frozen hydrometeors (cloud ice, snow, hail and graupel).

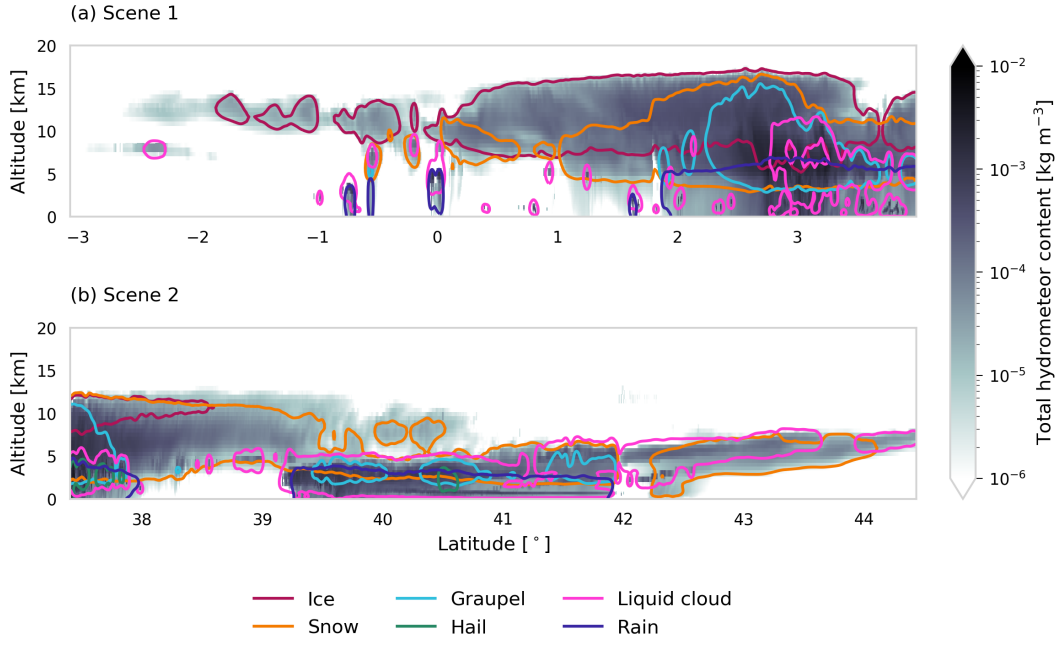


Figure 1. The distribution of total hydrometeor mass content in the two cloud scenes used to test the retrieval. Colored lines show the $m = 10^{-5} \text{ kg m}^{-3}$ contour for different hydrometeor species.

Table 1. Particle-model names, IDs and parameters α, β of the mass-size relationships $m = \alpha D_{\max}^{\beta}$, where D_{\max} is the maximum diameter of the particle. The ID column contains the particle shape identifier of the particle model in the Eriksson et al. (2018) scattering database.

Hydrometeor species	Particle shape	ID	α	β
Cloud ice	GemCloudIce	31	440	3
Snow	GemSnow	32	52.4	3
Graupel	GemGraupel	33	209.4	3
Hail	GemHail	34	471.2	3
Rain	LiquidSphere	25	523.6	3
Liquid cloud	LiquidSphere	25	523.6	3

The particle size distribution (PSD) of each hydrometeor type is parametrized by its particle number concentration and mass density. The full particle size distribution can be prognosed from the two moments using a species-dependent parametrization and mass-size relationship. The parameters of the mass-size relationship are given in Tab. 1. As shown in the table, the masses of all ice particles in the model are assumed to scale with a power of three, which leads to high densities for large particles.

95 Examples of particle size distributions of frozen hydrometeors are displayed in Fig. 2. The four panels display the prognosed particle size distributions for the four frozen hydrometeor types together with renderings of the particle shapes used in the

forward simulations. As these plots show, the assumed particle size distributions across different ice species vary mostly in their horizontal and vertical scaling, whereas the function shape shows less variability. Furthermore, an important characteristic of the model can be identified here, which will help to better understand the retrieval results presented later: Cloud ice in the model 100 is characterized by high particle number densities and small particle sizes, whereas snow exhibits lower number concentrations and larger particles.

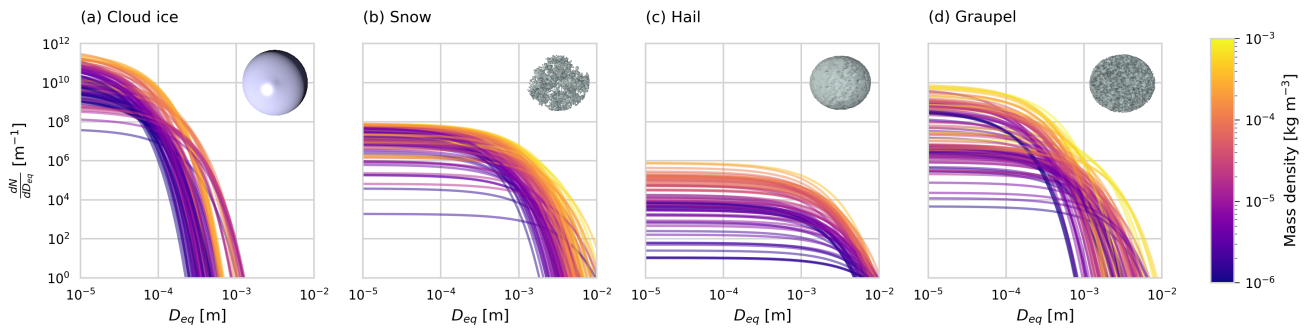


Figure 2. Realizations of particle size distributions from the cloud scenes used in this study. The number particle density is plotted with respect to the volume-equivalent diameter D_{eq} . Shown are the PSDs corresponding to 100 randomly chosen grid points with a mass concentration higher than $10^{-6} \text{ kg m}^{-3}$. Line color encodes the corresponding mass density.

2.2 Simulated cloud observations

A simulated observation is generated for each vertical profile in the model test scenes. The simulations apply the same micro-physics scheme as the model, which means that they use the same six hydrometeor classes and PSD parametrizations.

105 2.2.1 Sensor configuration

Simulations of observed passive brightness temperatures are performed for the 11 highest-frequency channels of the MWI radiometer and all channels of the ICI radiometer. The passive observations are combined with a W-band cloud radar similar to the CloudSat Cloud Profiling Radar (CPR) (Stephens et al., 2002; Tanelli et al., 2008).

A number of simplifications are applied for the generation of the synthetic cloud observations: Firstly, the beams of all three 110 sensors are modeled as perfectly coincident pencil beams. Secondly, a synthetic observation is generated for each vertical profile from the model scenes by simulating a one-dimensional, plane-parallel atmosphere, the properties of which are taken from the corresponding model profile. It follows from these modeling decisions that the atmosphere is assumed to be homogeneous across the beams of the active and passive sensors and that they all sense the same atmospheric volume. This is certainly not the case for space-borne observations and will incur a forward modeling error that is not accounted for in this study. Since the 115 focus of this study are the fundamental synergies between the active and passive observations, quantifying the impact of beam width and inhomogeneity is left for future investigation.

Observations from the ICI radiometer are simulated by performing a single, non-polarized radiative transfer simulation located at the centers of the pass bands of each channel and averaging the resulting brightness temperatures. For channels with multiple polarizations, only a single simulation is performed. To compensate for this, the noise of the corresponding channel is 120 reduced by a factor of $\sqrt{2}$. The simulated ICI channels and assumed noise levels are presented in Tab. 2. The off-nadir viewing angle of ICI is assumed to be 48° at the sensor.

Observations from the MWI radiometer are simulated in a similar manner as those from ICI. However, from MWI only channels with frequencies larger than or equal to 89 GHz are used. The reason for this is that the footprints of the channels with frequencies lower than 89 GHz have full-width at half maximum of 50 km compared to only 10 km for the higher-125 frequency channels. Due to the very small overlap of the footprints of these low-frequency channels with that of the radar, it is assumed they would not be beneficial for a synergistic retrieval and are therefore disregarded here. The included MWI channels are listed in Tab. 2.

Table 2. Channels of the MWI and ICI radiometers used in the retrieval.

MWI			ICI		
Channel	Freq. [GHz]	Noise [K]	Channel	Freq. [GHz]	Noise [K]
MWI-8	89	1.1	ICI-1	183.31 ± 7.0	0.8
MWI-9	118.75 ± 3.2	1.3	ICI-2	± 3.4	0.8
MWI-10	± 2.1	1.3	ICI-3	± 2.0	0.8
MWI-11	± 1.4	1.3	ICI-4	243 ± 2.5	$\frac{1}{\sqrt{2}} \cdot 0.7$
MWI-12	± 1.2	1.3	ICI-5	325.15 ± 9.5	1.2
MWI-13	165.5 ± 0.75	1.3	ICI-6	± 3.5	1.3
MWI-14	183.31 ± 7.0	1.2	ICI-7	± 1.5	1.5
MWI-15	± 6.1	1.2	ICI-8	448 ± 7.2	1.4
MWI-16	± 4.9	1.2	ICI-9	± 3.0	1.6
MWI-17	± 3.4	1.2	ICI-10	± 1.4	2.0
MWI-18	± 2.0	1.3	ICI-11	664 ± 4.2	$\frac{1}{\sqrt{2}} \cdot 1.6$

The frequency of the the cloud radar is chosen to be 94 GHz similar to CloudSat CPR. The vertical resolution of the radar observations is assumed to be 500 m ranging from 0.5 to 20 km in altitude. The minimum sensitivity is set to be -30 dBZ 130 and the noise at each range gate is modeled to be independent with standard deviation 0.5 dBZ. As mentioned above, the same incidence angle as for the passive radiometers is assumed also for the radar. In practice, this could be achieved by remapping the radar observations to the lines of sights of the passive beams.

2.2.2 Radiative transfer simulations

All simulations presented in this study were performed using Version 2.3.1245 of the Atmospheric Radiative Transfer Simulator (ARTS, Buehler et al. (2018)). Radar reflectivities are computed using ARTS' built-in single-scattering radar solver. For the 135

simulation of passive radiances, a hybrid solver is used which combines the DISORT (Stamnes et al., 2000) scattering solver with the ARTS standard scheme for pencil beam radiative transfer. The hybrid solver has been added to ARTS specifically for this study and provides approximate, analytical Jacobians, which are required for the variational retrievals of hydrometeors.

All simulations are performed assuming an ocean surface with emissivities calculated using the Tool to Estimate Sea-Surface Emissivity from Microwaves to sub-Millimeter waves (TESSEM, Prigent et al. (2017)). Polarization is neglected in all simulations performed in this study. Particle scattering data are taken from the ARTS scattering data base (hereafter ARTS SSDB, Eriksson et al. (2018)). Gaseous absorption is modeled using the absorption models from Rosenkranz (1993) for N_2 , O_2 and from Rosenkranz (1998) for H_2O .

2.3 Retrieval algorithm

A one-dimensional, variational cloud retrieval algorithm is proposed to retrieve distributions of frozen hydrometeors from the combined active and passive observations. The algorithm uses the optimal estimation method (OEM) developed by Rodgers (2000). The retrieved state $\mathbf{x} \in \mathbb{R}^n$ is determined by fitting a forward model $\mathbf{F} : \mathbb{R}^n \rightarrow \mathbb{R}^m$ to a set of observations $\mathbf{y} \in \mathbb{R}^m$. The best fit is determined by minimizing a cost function of the form

$$\mathcal{L}(\mathbf{x}, \mathbf{y}) \propto (\mathbf{F}(\mathbf{x}) - \mathbf{y})^T \mathbf{S}_e^{-1} (\mathbf{F}(\mathbf{x}) - \mathbf{y}) + (\mathbf{x} - \mathbf{x}_a)^T \mathbf{S}_a^{-1} (\mathbf{x} - \mathbf{x}_a). \quad (1)$$

The cost function $\mathcal{L}(\mathbf{x}, \mathbf{y})$ corresponds to the negative log-likelihood of the a posteriori distribution of the state \mathbf{x} under the assumptions of Gaussian a priori distribution with mean \mathbf{x}_a and covariance matrix \mathbf{S}_a as well as zero-mean Gaussian measurement error with covariance matrix \mathbf{S}_e .

To assess the quality of a retrieved state $\hat{\mathbf{x}}$ and corresponding simulated observation $\hat{\mathbf{y}} = \mathbf{F}(\hat{\mathbf{x}})$, we define the following diagnostic quantity

$$155 \quad \chi_y^2 = \delta\mathbf{y}^T \mathbf{S}_e^{-1} \delta\mathbf{y}, \quad (2)$$

where $\delta\mathbf{y} = \mathbf{y} - \hat{\mathbf{y}}$. The quantity χ_y^2 is here used to approximate a χ^2 -test for the misfit between the observations \mathbf{y} and the retrieval fit $\hat{\mathbf{y}}$. Although a formally correct χ^2 -test for $\delta\mathbf{y}$ should apply a different covariance matrix (c.f. Chapter 12 in Rodgers (2000)), such tests were found to yield very high values that deviate strongly from the expected chi-square distribution. The χ_y^2 value used here provides a less strict test in the sense that it will generally be smaller than if the formally correct covariance matrix was used.

The amount of information contained in a retrieval can be quantified by computing the degrees of freedom for signal (DFS). Let $\mathbf{K} \in \mathbb{R}^{m \times n}$ be the Jacobian of the forward model \mathbf{F} . Then the DFS of the observations can be computed as the trace of the averaging kernel matrix

$$\mathbf{A} = (\mathbf{K}^T \mathbf{S}_e^{-1} \mathbf{K} + \mathbf{S}_a^{-1})^{-1} \mathbf{K}^T \mathbf{S}_e^{-1} \mathbf{K}. \quad (3)$$

165 **2.3.1 Measurement space**

The input for the retrieval algorithm is the combined observation vector \mathbf{y} consisting of the concatenated single-instrument observations from the cloud radar and the two radiometers. Measurement errors are assumed to be independent and Gaussian distributed with standard deviations according to the noise characteristics given in Section 2.2.1.

2.3.2 State space

- 170 The proposed retrieval solves for distributions of one frozen and one liquid hydrometeor species in the atmospheric column together with profiles of atmospheric humidity and liquid-cloud mass density. The retrieval uses the same vertical grid as the model scenes, which have a vertical resolution of about 500 m throughout the troposphere. If not specified otherwise, retrieval quantities are retrieved at this resolution.

Distributions of hydrometeors in the atmospheric column are represented using the normalized particle size distribution 175 formalism proposed by Delanoë et al. (2005). The PSD of a hydrometeor species at a given height level is represented by a vertical and a horizontal scaling parameter, the mass-weighted mean diameter D_m and the normalized number density N_0^* . Alternative parametrizations using mass density and D_m or the mass density and N_0^* have been tested but no considerable effect on retrieval performance has been observed.

- The retrieval computes vertical profiles of the two scaling parameters D_m and N_0^* for each of the two hydrometeor species. 180 The remaining shape of each PSD is described by the shape parameters α and β , not to be confused with the parameters of the mass-size relationship shown in Tab. 1. The shape parameters are set to fixed, species-specific values. This principle is illustrated in Fig. 3. The plot displays the a-priori-assumed shapes of the particle size distribution of frozen and liquid 185 hydrometeors. The retrieved horizontal and vertical scaling parameters, D_m and N_0^* , are used as units for the axes of the plot so that the shape of the PSD becomes independent of the retrieved mass density and number concentration. For frozen hydrometeors, the values of the shape parameters α and β are chosen identical to version 3 of the DARDAR-CLOUD product (Cazenave et al., 2018). For liquid hydrometeors, the shape parameters are chosen so that they are equivalent to the shape used by the GEM model for rain drops. All calculations involving particles size distributions use the volume-equivalent diameter D_{eq} as size variable.

The temperature-dependent a priori profile for N_0^* of frozen hydrometeors is determined using the relation from Delanoë 190 et al. (2014)

$$N_0^* = \exp(-0.076586 \cdot (T - 272.5) + 17.948), \quad (4)$$

where T is in K. The a priori profile for D_m for frozen hydrometeors is chosen so that the a priori mass density is equal to $10^{-6} \text{ kg m}^{-3}$. For liquid hydrometeors, a fixed value for N_0^* of 10^6 m^4 is assumed and the a priori profile for D_m is determined similarly as for frozen hydrometeors. Values of the mass-weighted mean diameter D_m for both hydrometeor 195 species are retrieved in linear space, whereas the normalized number concentration parameter N_0^* is retrieved in \log_{10} space. As additional constraints, the retrieval of frozen hydrometeors is restricted to the region between the freezing layer and the tropopause, whereas the retrieval of liquid hydrometeors is restricted to below the freezing layer.

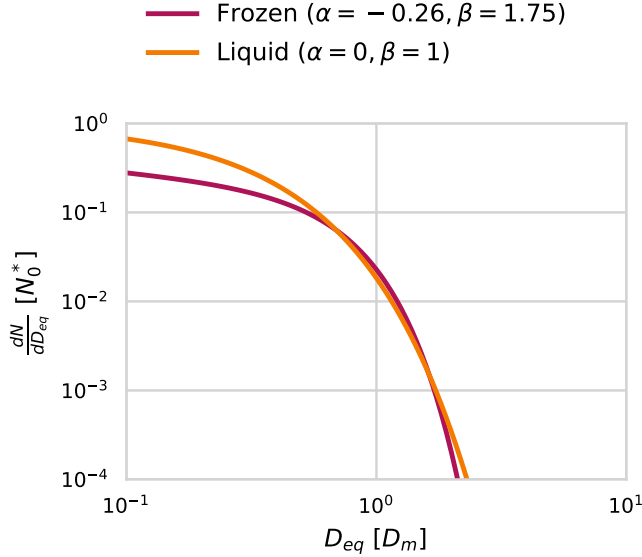


Figure 3. PSD parametrizations for frozen and liquid hydrometeors used in the cloud retrieval.

To further regularize the retrieval, N_0^* for ice is retrieved at only 10 equally-spaced grid points between freezing layer and the tropopause. Similarly, D_m and N_0^* for rain are retrieved at 10 respectively 4 points between surface and freezing layer.

200 This was necessary to avoid the retrieval from getting stuck in spurious local minima. An approach similar to this one is also taken in the GPM combined precipitation retrievals (Grecu et al., 2016).

Humidity in the atmospheric column is retrieved in units of relative humidity at a vertical resolution of 1 km. However, instead of retrieving relative humidity directly, an inverse hyperbolic tangens transformation is applied to the relative humidity profile ϕ :

$$205 \quad x = \operatorname{arctanh}\left(\frac{2\phi}{1.1} - 1.0\right) \quad (5)$$

The transformation restricts the retrieved relative humidity values to the range of [0.0, 1.1]. The a priori profile for relative humidity is arbitrarily chosen as

$$\phi(t) = \begin{cases} 0.7 & , 270 \text{ K} < t \\ 0.7 - 0.01 \cdot (t - 270) & , 220 < t \leq 270 \text{ K} \\ 0.2 \cdot (t - 270) & , t < 220 \end{cases}. \quad (6)$$

The retrieval of liquid cloud mass density, here referred to as liquid water content (LWC), is performed at seven equally spaced 210 altitude levels between the surface and the 230 K isotherm. In contrast to frozen and liquid hydrometeors, cloud water is modeled in the retrieval forward model to be purely absorbing using the absorption model by Liebe et al. (1993) for suspended

liquid cloud droplets. Liquid cloud mass density is retrieved in \log_{10} -space and the a priori profile is set to a fixed value of $10^{-6} \text{ kg m}^{-3}$ in the permitted region of the atmosphere.

The a priori distributions of the 6 retrieval quantities (N_0^* and D_m for frozen and liquid hydrometeors, relative humidity ϕ , cloud water) are assumed to be independent so that the overall a priori covariance matrix \mathbf{S}_a has block-diagonal structure. Within each block, vertical correlations between the values of a given retrieval quantity at different altitudes are assumed to be exponentially decaying. Hence, the correlation of the values of retrieval quantity q at points i and j of the retrieval grid is computed as

$$(\mathbf{S}_{a,q})_{i,j} = \sigma_{q,i}\sigma_{q,j} \cdot \exp\left(-\frac{d(i,j)}{l_q}\right), \quad (7)$$

where $\sigma_{q,i}$ is the a priori uncertainty assumed for retrieval quantity q at grid point i , $d(i,j)$ the distance between the grid points and l_q the quantity-specific correlation length. The assumed a priori uncertainties and correlation lengths for the retrieval quantities are summarized in Tab. 3.

Table 3. A priori uncertainties and correlation lengths used in the retrieval.

Quantity q	σ_q	$l_q [\text{km}]$
$\log_{10}(N_{0,\text{frozen}}^*)$	2	5
$D_{m,\text{ice}}$	$300 \mu\text{m}$	5
$\log_{10}(N_{0,\text{liquid}}^*)$	2	2
$D_{m,\text{liquid}}$	$500 \mu\text{m}$	2
$\operatorname{arctanh}\left(\frac{2 \cdot \phi}{1.1} - 1.0\right)$	2	2
$\log_{10}(m_{\text{liquid cloud}})$	1	2

As baselines for the assessment of the combined retrieval, also a radar-only and a passive only-retrieval are performed. The radar-only retrieval uses the same implementation as the combined retrieval, but only retrieves frozen and liquid hydrometeors.

For the radar-only retrieval, perfect knowledge of the atmospheric humidity profile is assumed but liquid cloud is ignored in the retrieval forward model.

The setup and retrieval quantities of the passive-only retrieval are similar to the combined retrieval, with the only difference being that frozen and liquid hydrometeors are retrieved at reduced resolution. For ice, N_0^* is retrieved at three equally spaced grid points between freezing layer and troposphere, while D_m is retrieved at five. For liquid hydrometeors, the retrieval grids for N_0^* and D_m are reduced to two equally spaced points between surface and freezing layer. Relative humidity is retrieved at a vertical resolution of 2 km.

3 Results

The first part of this section presents results from a numerical experiment that investigates the complementary information content of the active and passive microwave observations. Results of the combined and the baseline retrievals applied to the reference cloud scenes are presented in the remaining part of this section.

3.1 Complementary information content

A fundamental question regarding the benefit of combining two remote sensing observations in a retrieval is to what extent the observations contain non-redundant information. The degree of non-redundancy in the combined observations is what we refer to here as complementary information content. In order to explore this complementary information content in the radar and radiometer observations, an idealized, homogeneous cloud layer with a thickness of 4 km located at an altitude of 10 km in a tropical atmosphere is considered. The cloud is assumed to consist of a single species of frozen hydrometeors represented using the PSD parametrization which is also used in the retrieval and described in Sec. 2.3.2. As particle model, the 8-ColumnAggregate (ID 8) from the ARTS SSDB is used.

The question that is addressed here is whether the combination of active and passive observations is able to constrain both the horizontal and the vertical scaling factors of the PSD of the ice particles in the cloud. To investigate this, the N_0^* and D_m parameters of the homogeneous cloud layer are varied and observations of the cloud layer are simulated. Figure 4 displays the simulated passive cloud signal, i.e. the brightness temperature difference between clear sky and cloudy sky simulation, as filled contours for a selection of channels of the MWI and ICI sensors. For given values of N_0^* and D_m , the corresponding ice mass density is given by the relation

$$m = \frac{\pi\rho}{4^4} N_0^* D_m^4. \quad (8)$$

In the figure, the cloud signal is displayed in D_m -mass density space and thus shows how the measured passive cloud signal varies with the horizontal and vertical scaling parameters of the PSD. Overlaid onto the contours of the passive cloud signal are the isolines of the maximum radar reflectivity returned from the cloud.

The contours of the measured active and passive cloud signals show the ambiguity of the single-instrument measurements with respect to the parameters of the PSD: Along these contours the signal does not change, while the cloud composition does. A necessary condition for a combined cloud retrieval to be able to resolve this ambiguity is that the contours of the active and passive signals cross each other. The panels in Fig. 4 thus provide an indication to what extent the information in the radar measurement and the corresponding passive radiometer channel provide complementary information on the parameters of the PSD. Considering the panels corresponding to the MWI channels, the results show that the observations contain complementary information only for very dense clouds consisting of very large particles. In contrast to that, the ICI observations exhibit crossing contours already at lower m and D_m values, indicating that the complementary information content in these observations is higher for less dense clouds consisting of smaller particles.

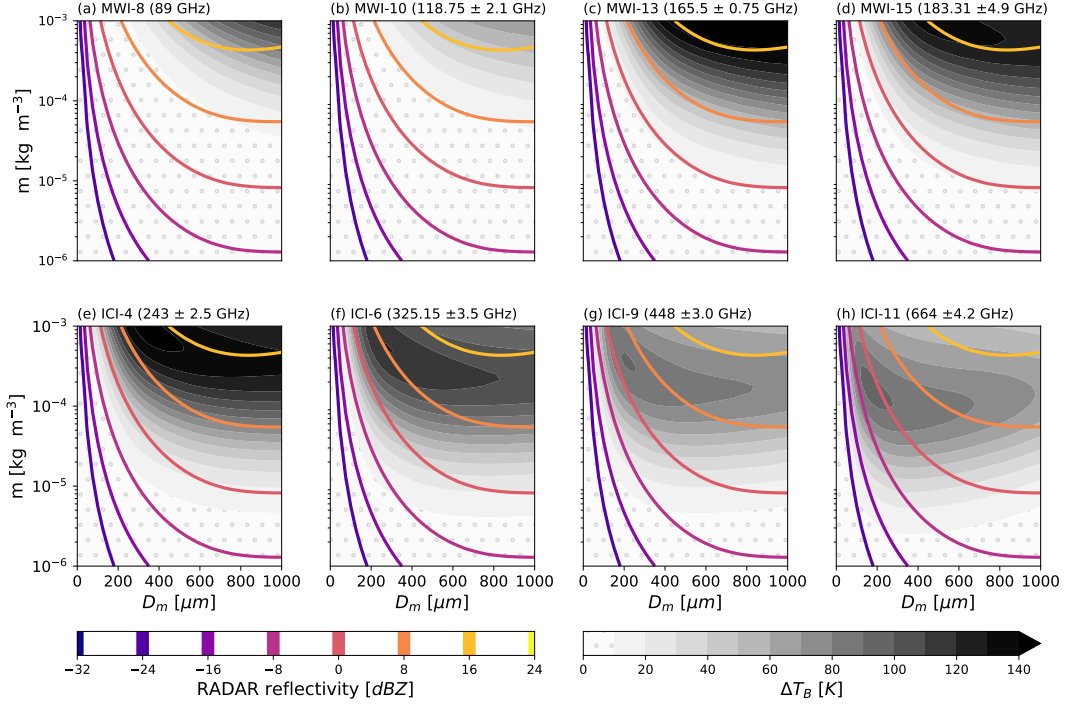


Figure 4. Simulated observations of a homogeneous cloud layer with varying mass density m and mass-weighted mean diameter D_m . The panels display the maximum radar reflectivity in dBZ overlaid onto the cloud signal measured by selected radiometer channels of the MWI (first row) and ICI radiometers (second row).

3.2 Retrieval results

To assess the performance of the combined cloud retrieval, the developed algorithm has been applied to the two designated 265 cloud scenes. The same retrievals have been performed with a radar-only and a passive-only version of the algorithm to serve as baselines for the combined retrieval. Each retrieval was performed multiple times using different ice particle models. The tested particle shapes are listed together with the corresponding mass size relations and ARTS SSDB identifier in Tab. 4. Since the results for both test scenes are qualitatively similar, not all analyses are shown for both scenes. Instead, these are provided as a digital supplement to this article.

270 The forward-simulated observations that were generated to test the retrievals are shown for the first test scene in Fig. 5. Independent Gaussian noise with standard deviations according to sensor specifications has been added to the simulated observations to account for sensor noise. It is important to note, that the simulated observations which are used to test the retrieval assume different microphysics than what is assumed in the retrieval: The synthetic observations are computed using the six hydrometeor classes from the GEM model, while the retrieval forward model assumes only two classes of hydrometeors.

Table 4. Particle model name, ARTS scattering database ID and parameters α, β of the mass-size relationships of the particle habits used in the retrieval.

Name	ID	α	β
GemCloudIce	31	440	3
GemSnow	32	24.0072	2.8571
GemGraupel	33	172.7527	2.9646
8-ColumnAggregate	8	65.4480	3
PlateType1	9	2.4770	0.7570
LargePlateAggregate	20	2.2571	0.2085

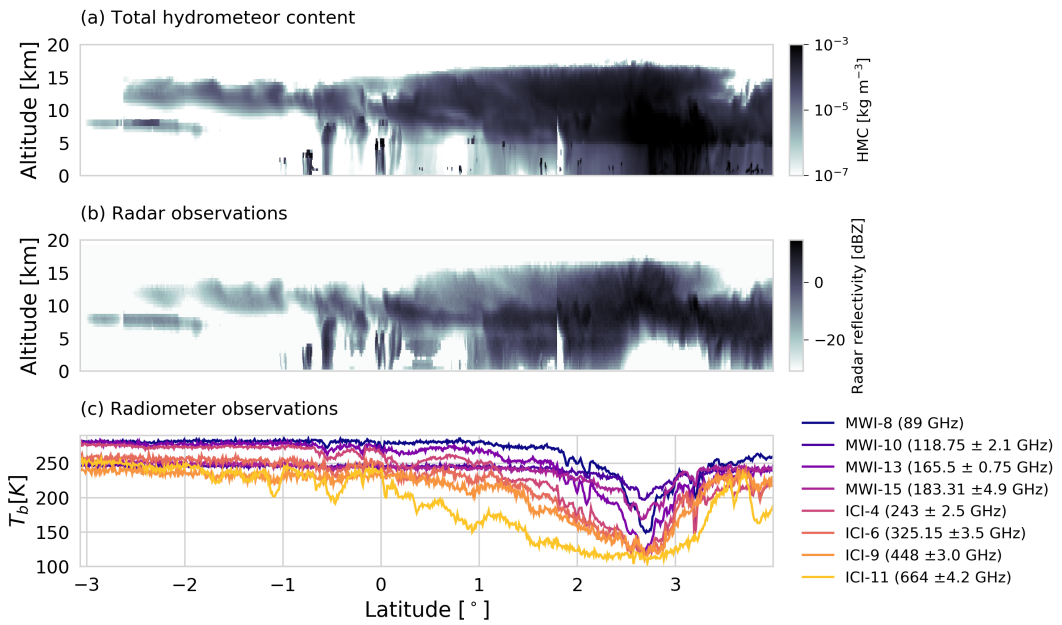


Figure 5. Total hydrometeor content (HMC) and simulated observations for the first test scene. Panel (a) displays the total hydrometeor content in the scene, i.e. the sum of the mass densities of all hydrometeor species of the GEM model. Panel (b) shows the simulated radar reflectivities. Panel (c) displays the simulated brightness temperatures for a selection of the channels of the MWI and ICI radiometers.

275 **3.2.1 Mass concentrations**

To provide an overview over how well the different retrieval methods are able to reproduce the cloud structures in the test scene, the retrieved ice water content (IWC) for the first test scene is shown in Figure 6. IWC is defined here as the sum of the mass densities of all frozen hydrometeor species. This means that the reference IWC is the sum of the four frozen hydrometeor species represented in the GEM model, whereas the retrieved IWC is simply the mass density of the single frozen hydrometeor species assumed in the retrieval. The results shown here were obtained using the LargePlateAggregate as particle model, which was found to be one of the best performing particle models.

280 Panel (a) of the figure displays the χ_y^2 value (normalized by the dimension of the measurement space) for each profile in the scene. A high value of χ_y^2 indicates that the retrieved state is not consistent with the input observations. The χ_y^2 value for the radar-only retrieval is remarkably low throughout most of the scene. This may indicate that the retrieval is insufficiently regularized, allowing it to fit the noise in the observations. The passive-only and combined retrieval, on the contrary, have a normalized χ_y^2 value around 1 over most of the scene. Since the presented values are normalized, the value 1 corresponds to the expected value of the approximated chi-square distribution of χ_y^2 . All three retrievals exhibit a region of elevated χ_y^2 values near the core of the convective system. In particular the high values of the passive-only and combined retrievals indicate that the retrieval was not able to find a good fit to the observations here.

290 Panel (b) displays the retrieved column-integrated IWC, the ice water path (IWP). The IWP is given in dB relative to the reference IWP since, owing to the high dynamic range of the reference values, the curves could otherwise not be distinguished. Although all methods reproduce the reference IWP fairly well, the combined retrieval yields the best overall agreement with the reference values. Exceptions are the regions of high χ_y^2 values where the retrieval failed to find a good fit to the observations.

295 Panel (c) shows the IWC field retrieved using the passive-only retrieval. Despite a certain resemblance in the overall structure between the retrieved and reference IWC field, the results do not reproduce the vertical structure of the cloud very well. It should be noted, however, that the displayed mass-density range extends below the sensitivity limit of the passive-only observations around 10^{-5} kg m⁻³ (c.f. Fig. 4), which explains the smeared-out appearance of the results to some extent.

300 The radar-only results, shown in panel (d), reproduce the vertical structure of the cloud well. Nonetheless, when compared to the reference IWC field, certain discrepancies are visible: The radar-only retrieval tends to overestimate the mass density at the bottom of the cloud and underestimate the mass concentrations at the top of the cloud.

The results of the combined retrieval are displayed in panel (e). Although some artifacts are clearly visible in the retrieved IWC field, the retrieval reproduces the vertical structure well. In particular, the combined retrieval succeeds to correct some of the systematic deviations of the radar-only retrieval: The mass density at cloud base is reduced and increased at cloud top.

305 To make the assessment of the retrieval performance more quantitative, the reference mass concentrations are plotted against the retrieved values in Fig. 7 and 8. The plots show the results for all different retrieval configurations and tested particle models. Markers in the plots are color-coded according to the prevailing hydrometeor type (by mass density) in the reference scene in order to allow assessment of the retrieval performance for the different hydrometeor types of the GEM model.

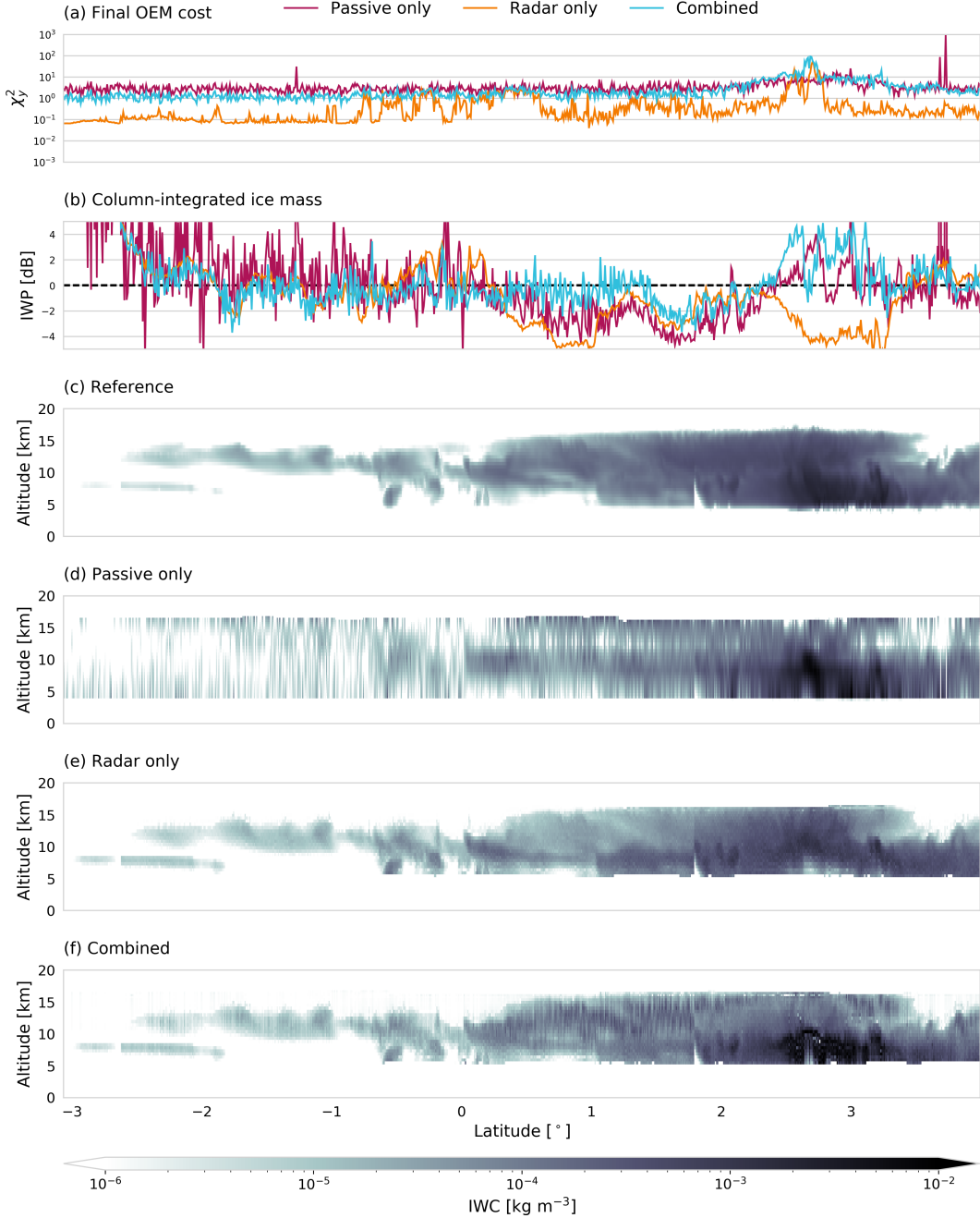


Figure 6. Results of the ice hydrometeor retrieval for the first test scene. Panel (a) displays the value of the χ^2_y diagnostic normalized by the dimension of the measurement space of the corresponding retrieval. Panel (b) displays retrieved IWP in dB relative to the reference IWP. Panel (c) shows the reference IWC from the model scene. Panel (d), (e) and (f) display the retrieval results for the passive-only, radar-only and combined retrieval, respectively.

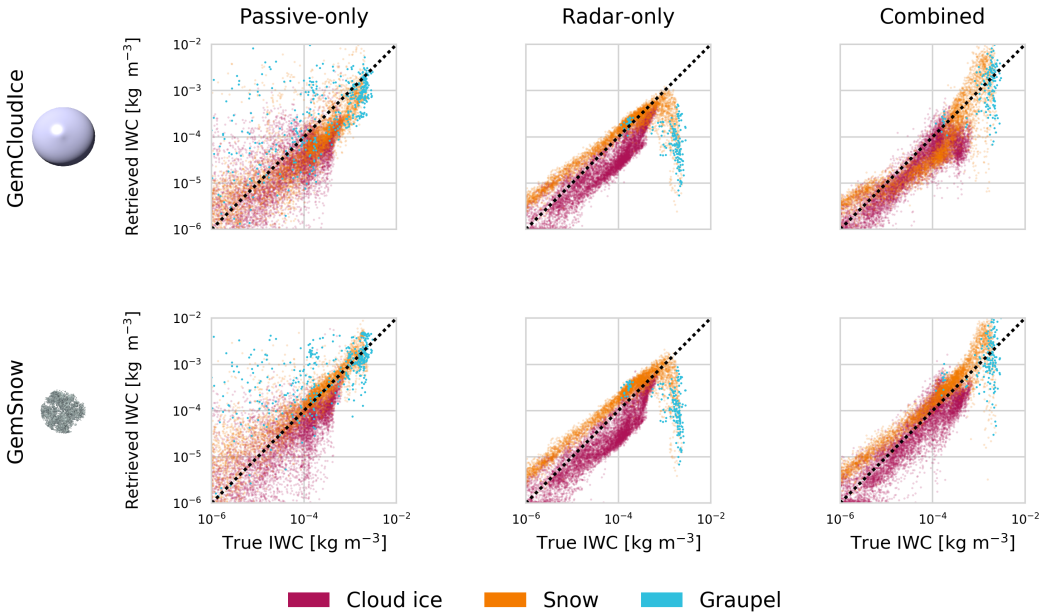


Figure 7. Reference IWC plotted against retrieved IWC for the tested retrieval configurations. Each row shows the retrieval results for the particle shape shown in the first panel. The following panels show the retrieval results for the passive only (first column), the radar only (second column) and the combined retrieval (third column). Markers are colored according to the prevailing hydrometeor type at the corresponding grid point in the test scene. Due to their sparsity, markers corresponding to graupel are drawn at twice the size of the other markers.

Not surprisingly, the results from the passive-only retrieval exhibit the strongest deviations from the diagonal. Since the passive channels alone contain only limited information on the vertical distribution of ice in the atmosphere, the retrieval cannot
310 be expected to yield accurate results at the resolution considered here. Although rather weak, a certain effect of the ice particle model on the retrieval results can be observed. In particular, the GemCloudIce model leads to a systematic underestimation of ice mass densities, which are less pronounced for the other particle models.

The results from the radar-only retrieval are more accurate than the passive-only retrieval, with almost all retrieval results located fairly close to the diagonal. The most distinct feature of the radar-only results, however, is the emergence of two
315 clusters that extend along the diagonal but are displaced above respectively below it. The color coding of the markers reveals that these clusters correspond to grid points dominated by ice for the cluster below the diagonal and snow for the cluster located above the diagonal. This indicates that the radar-only retrieval systematically underestimates mass densities for cloud ice but overestimates the mass density of snow. The effect is observed for all tested particle shapes and thus likely independent of it. In general, the radar-only results exhibit only very weak dependency on the particle model, making the results for different
320 particle shapes virtually indistinguishable.

Another feature that stands out in the radar-only results is that the retrieval does not work for graupel. This, however, can be understood by comparing the radar reflectivities shown in Fig. 5 with the cloud structure displayed in Fig. 1. It becomes apparent that graupel in this scene is located where the radar signal is fully attenuated. Since there is no signal to retrieve the mass density from, this explains the bad performance of the radar-only retrieval for these grid points.

325 Similar to the radar-only retrieval, the results of the combined retrieval are located close to the diagonal. But the clusters observed in the radar-only results are to large extent merged in the combined results. Moreover, except for the results obtained with the GemCloudIce particle shape, the two clusters move in closer towards the diagonal. The combined retrieval thus improves the IWC retrieval for the specific hydrometeor species in the scene.

Nonetheless, the results for the GemCloudIce particle stand out in the results. Even though the systematic deviations observed in the radar-only retrieval are reduced for most particle shapes, for this specific shape they are instead increased. 330 The retrieval error is particularly large for snow, which is strongly underestimated for reference mass concentrations around $10^{-4} \text{ kg m}^{-3}$.

The results for the second test scene obtained using the LargePlateAggregate particle model are shown in Fig. 9. As mentioned above, the results are qualitatively very similar to those of the first scene. Also here, the final OEM cost, shown in 335 Panel (a), displays a region of increased cost for the passive-only and combined retrievals. This is again a region of very dense cloud which consists of graupel and snow. Also similar to the first scene, the passive only retrieval does not reproduce the structure of the cloud well. Although the cloud top is placed at the right position, neither the vertical structure of the cloud nor its base are resolved. The radar-only retrieval resolves the vertical structure of the cloud well, but overestimates the ice mass density in the scene. The combined retrieval also resolves the vertical structure of the cloud well and corrects the overestimation 340 observed in the radar-only results to some extent.

Scatter plots for the retrieval results from the second scene are shown in Fig. 10. Except for the lack of cloud ice in the scene, the results are similar to what has been observed in the first scene: The radar-only retrieval overestimates the mass density of snow in the scene. This effect is corrected by the combined retrieval for most of the tested particle shapes. The exception is the GemCloudIce particle for which the retrieval of snow particle deteriorates quite drastically.

345 To summarize retrieval performance for all tested retrieval methods and particle shapes, the logarithmic error

$$E_{\log_{10}} = \log_{10} \left(\frac{x_{\text{retrieved}}}{x_{\text{reference}}} \right) \quad (9)$$

for the retrieved IWC and IWP are displayed in Fig. 11. The logarithmic error in the IWC retrieval has been computed only for grid points where either reference or retrieved IWC is larger than $10^{-6} \text{ kg m}^{-3}$. Considering first the results of the IWC retrieval, shown in Panel (a) and (b), the plots confirm the findings from the analysis above: The combined retrieval generally 350 yields the smallest retrieval errors. Although the spread of the retrieval errors of the radar-only retrieval is lower in the second scene, the combined retrieval yields smaller systematic errors.

Compared in terms of IWP, however, the results are different. Especially the passive-only retrieval yields much lower errors for the retrieved IWP, making the results comparable if not better than those of the other methods. For the radar-only and

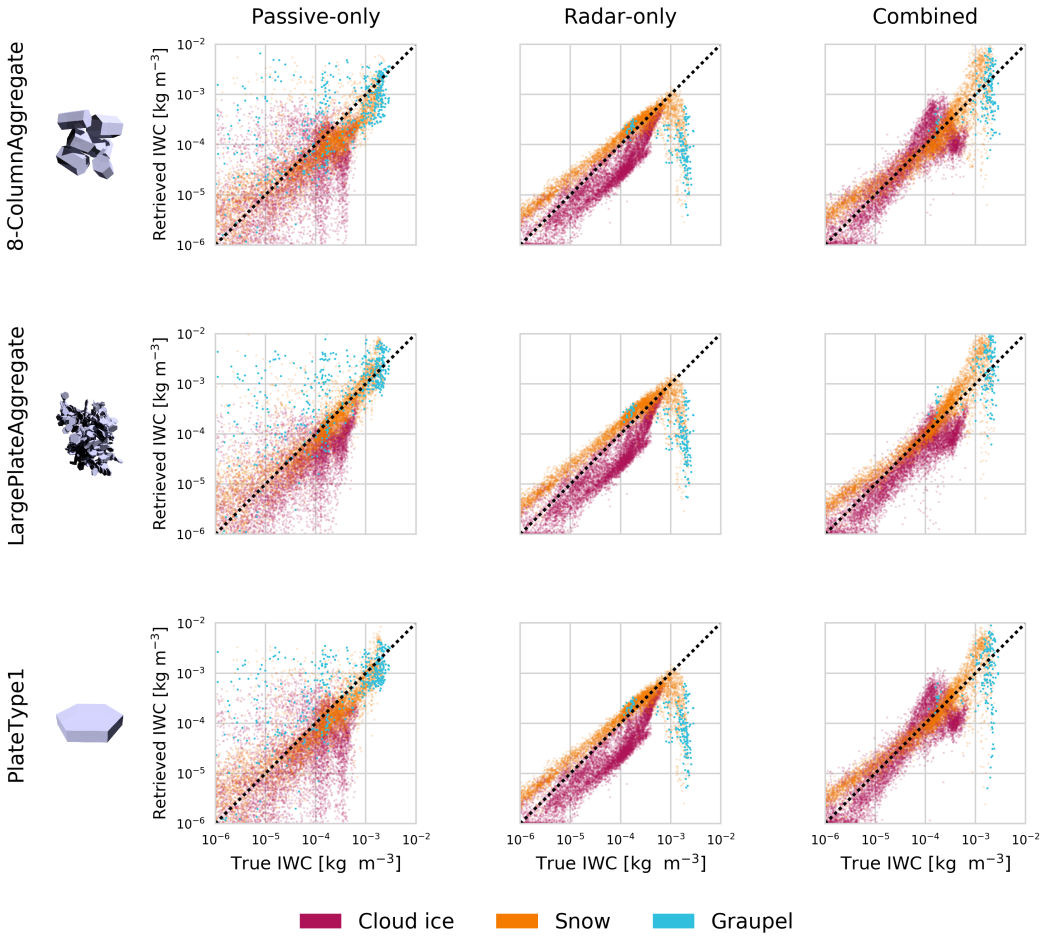


Figure 8. Same as Fig. 7 but for the remaining particle shapes.

combined retrievals the precision is generally increased but systematic deviations observed in the IWC persist. This leads,
 355 particularly for the second test scene, to significant systematic errors in the radar-only-retrieved IWP.

In addition to this, the passive-only and the combined retrieval exhibit a strong dependence of the retrieval error on the applied particle model. Especially the GemCloudIce and GemSnow particle models yield large retrieval errors for IWC and IWP. The other three particle models, however, consistently yield smaller retrieval than the GemCloudIce and GemSnow models.

360 3.2.2 Particle number densities

Particle number densities of frozen hydrometeors have been derived from the retrieved N_0^* and D_m parameters by computing the zeroth moment of the corresponding PSD. The resulting particle number density fields are displayed together with the

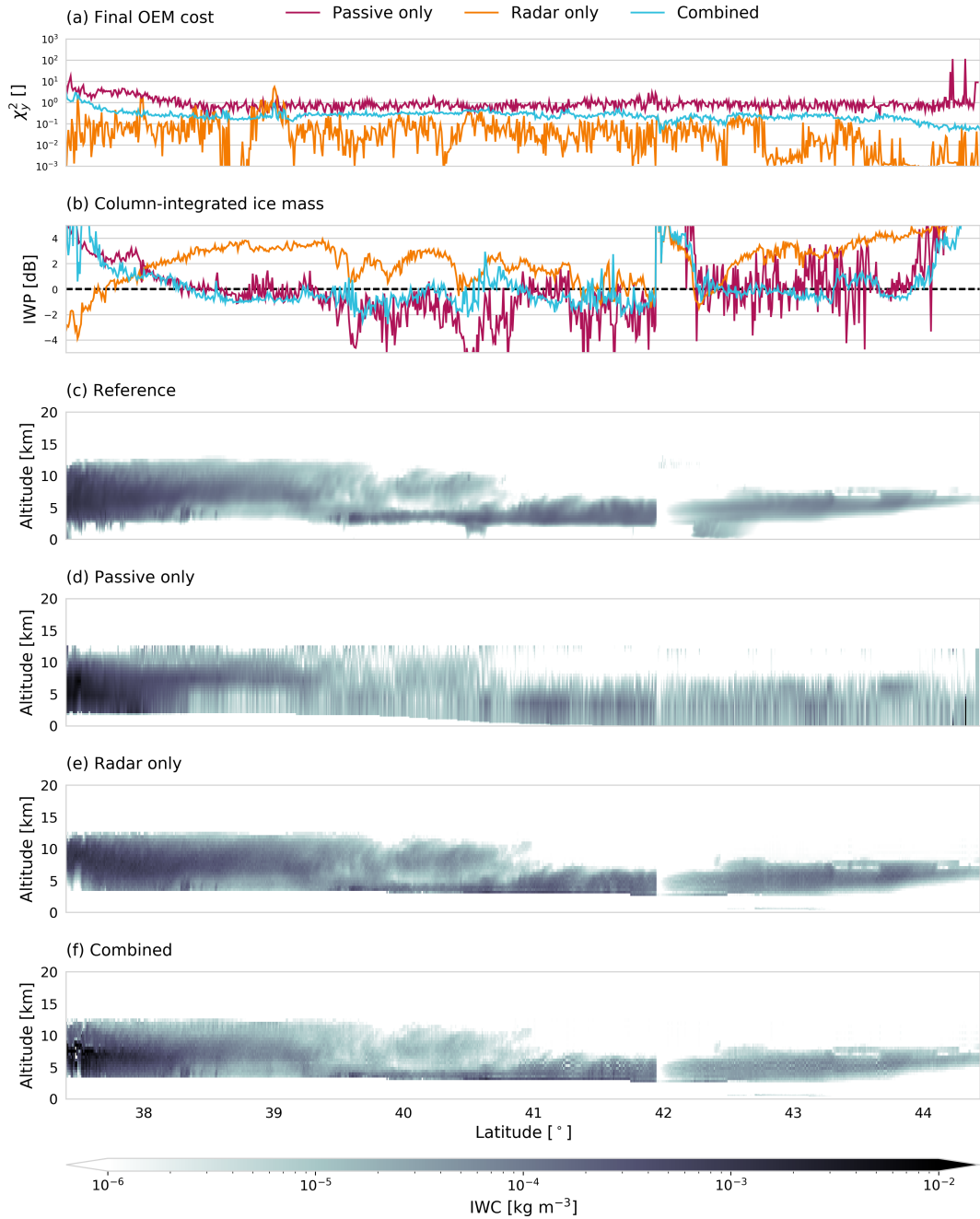


Figure 9. Results of the ice hydrometeor retrieval for the second test scene. Panel (a) displays the value of the χ^2_y diagnostic normalized by the dimension of the measurement space of the corresponding retrieval. Panel (b) shows retrieved IWP in dB relative to the reference IWP. Panel (c) displays the reference mass concentrations from the model scene. Panel (d), (e) and (f) display the retrieval results for the passive-only, radar-only and combined retrieval, respectively.

Figure 10. Scatter plots of the reference and retrieved ice mass densities for the second test scene. The rows show the retrieval results for a given assumed ice particle model. The first column of each row displays a rendering of the particle model. The following rows display the results for the passive-only, the radar-only and the combined retrieval.

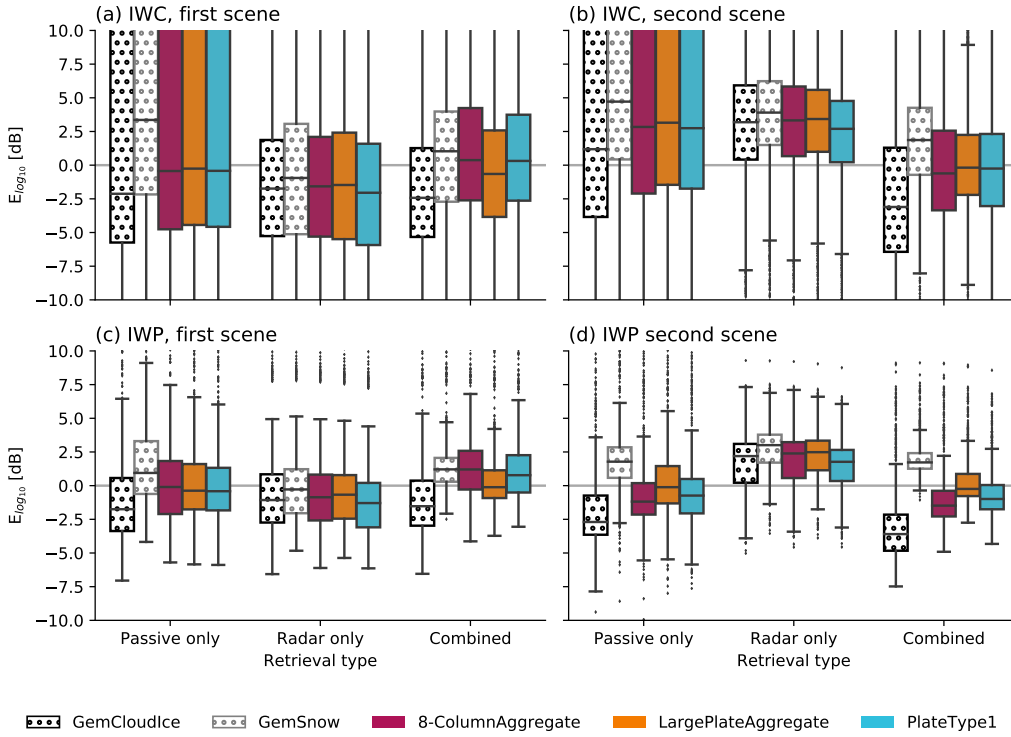


Figure 11. Distributions of the logarithmic retrieval error in IWC and IWP for all tested retrieval methods and particle shapes displayed as box plots. Colored boxes display the interquartile range (IQR) while whiskers show full range of all points not considered outliers. Points whose distance to the IQR is larger than 1.5 times the width of the IQR are considered outliers and drawn as markers.

reference field in Fig. 12. To simplify the comparison number densities are displayed only where the corresponding reference or retrieved IWC is larger than $10^{-6} \text{ kg m}^{-3}$.

Comparing the passive-only and the radar-only retrieval to the reference field shows that both methods have little to no skill in predicting number density concentrations. Although the passive-only retrieval partly captures the gradient between very high concentrations at the top of the cloud and the low concentrations at the bottom, it is not at all resolved in the radar-only retrieval. The combined retrieval, however, manages to reproduce this gradient in some parts of the scene. Although its exact structure is not fully reproduced, this clearly shows sensitivity of the retrievals to particle number concentrations.

370 The combined retrieval shows the strongest deviations from the reference field between 2 and 3° latitude. Here, the results
strongly underestimate the true number concentrations. Comparison with the cloud composition displayed in Panel (a) of Fig. 1
shows that this region contains large amounts of both cloud ice and snow. Since the retrieval uses only a single hydrometeor
species to represent ice in the atmosphere it is not able to represent such heterogeneous conditions. Since snow will have the
stronger impact on the observations, the retrieval in these regions tends to predict snow rather than ice, which leads to the low
375 retrieved number densities.

To further investigate this, Fig. 13 displays scatter plots of the reference and retrieved number density concentrations for
all three methods and two particle models from the first test scene. Markers in the plot are color coded according to their
homogeneity in the reference scene, here defined as the ratio of the maximum mass density of any of the frozen hydrometeor
species and total IWC.

380 These results confirm that the passive-only retrieval possesses certain sensitivity to the particle number density since the clus-
ter at low reference number densities corresponding to snow is placed correctly on the diagonal. The radar-only retrieval does
not exhibit any retrieval skill, hardly reproducing any of the variation of the references values. Contrary to this, the combined
385 retrieval moves both clusters towards the diagonal, indicating that it is capable of distinguishing the microphysical properties of
cloud ice and snow. Furthermore, the color coding shows that the strongest deviations between retrieved and reference number
densities occur for grid points where the cloud composition is heterogeneous. Even for the combined retrieval, however, the
accuracy of a single retrieval value remains fairly low.

The effect of particle shape on the retrieval results is somewhat similar to what has been observed for IWC. For the passive-
only and combined retrieval, the GemCloudIce model again yields the worst retrieval results, leading to a general underestima-
390 tion of the true particle number density. For the radar-only retrieval no noticeable differences are observed between different
particle models. Only the results for the GemCloudIce and LargePlateAggregate particle models are shown here since the
results for the other particles are mostly similar to those obtained with the LargePlateAggregate model.

3.2.3 Information content

The retrieval results presented above show that the combined observations allow a more accurate retrieval of both mass and
395 particle number density. This confirms the experimental results from Sec. 3.1, that active and passive observations provide
complementary information on the microphysics of ice particles. The information content of the retrievals can be assessed
more quantitatively using the averaging kernel matrix. The trace of the AVK, commonly referred to as the number of degrees
of freedom for signal (DFS), quantifies the number of independent pieces of information contained in the observations.

The distributions of the degrees of freedom of each retrieved profile in the test scenes are displayed in Fig. 14. Not-
surprisingly, the combined observations exhibit the highest information content. Nevertheless, comparison with the DFS values
400 of the active- and passive-only retrieval shows that the observations contain a certain degree of redundancy leading to a lower
combined DFS value than the direct sum of the two.

The grouping into retrieval quantities furthermore reveals that the largest increase in the information content comes from
water vapor, which is not retrieved in the radar-only retrieval. Although small, a significant increase in information content

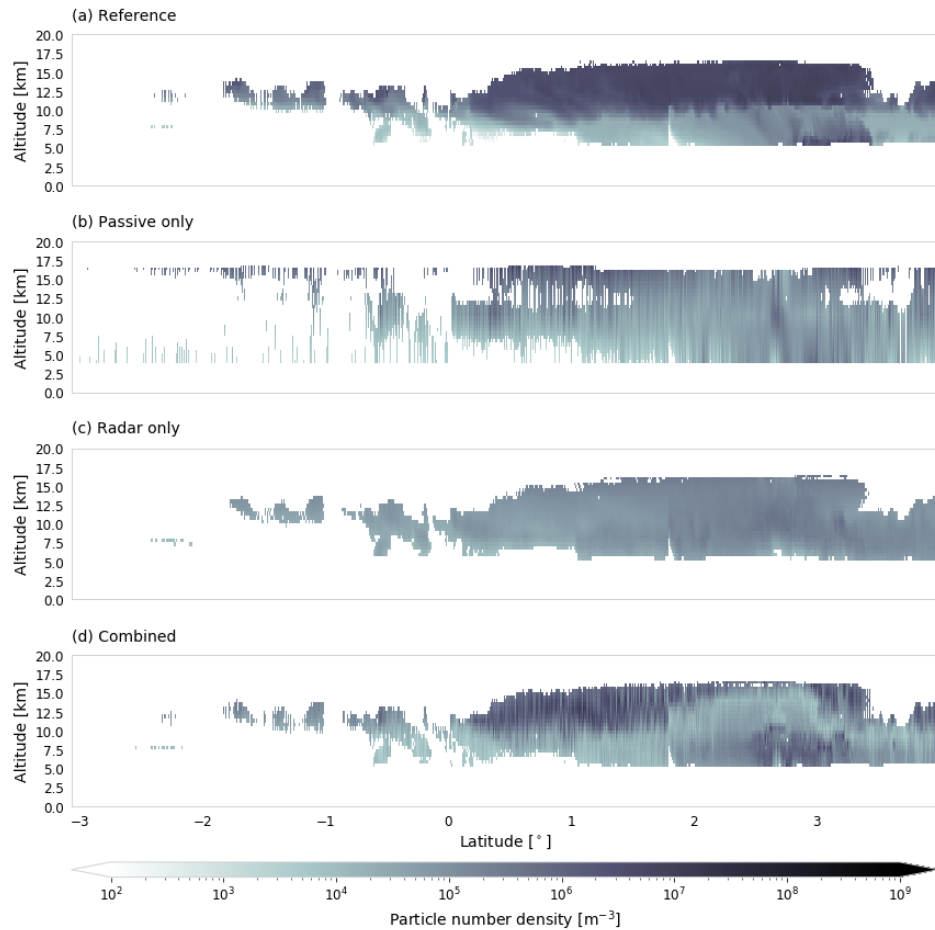


Figure 12. Reference and retrieved particle number concentrations of frozen hydrometeors for the first test scene obtained with the Large-PlateAggregate particle model. Panel (a) displays the reference mass concentrations from the model scene. Panel (b), (c) and (d) display the retrieval results for the passive-only, radar-only and combined retrieval. Only values for which the corresponding reference or retrieved IWC was larger than $10^{-6} \text{ kg m}^{-3}$ are shown here.

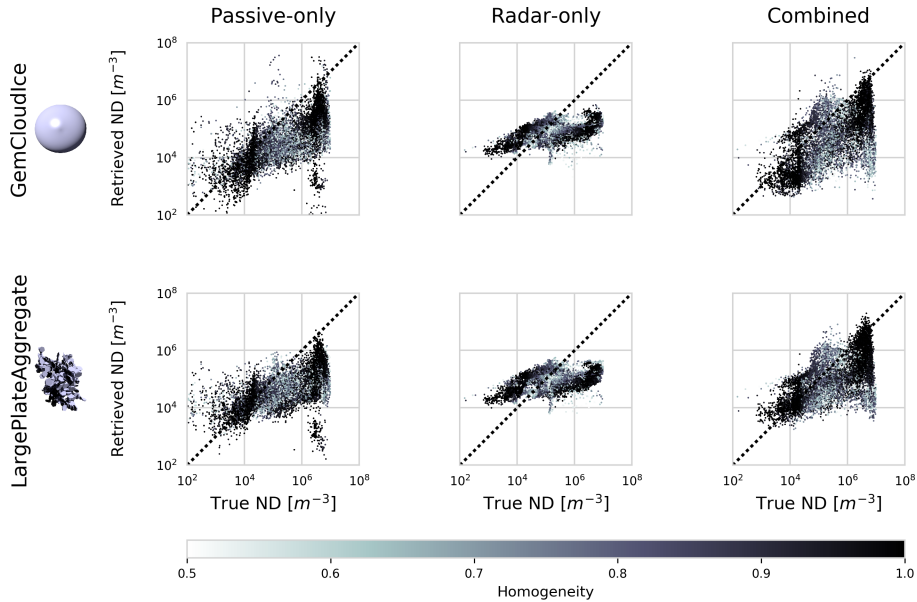


Figure 13. Scatter plots of the retrieved particle number densities at grid points with reference mass density larger than $10^{-5} \text{ kg m}^{-3}$. Rows show the results for the different particle models used in the retrieval while column display the results for the different retrieval methods. The marker color encodes the homogeneity of the corresponding ice mass, which is computed as the ratio of the maximum mass density of any of the frozen hydrometeor species and total IWC.

is observed for both scenes for the N_0^* parameter for ice hydrometeors. Interestingly, this increase is observed even though
 405 the information content in the passive-only observations for N_0^* is close to zero. For the D_m parameter, a small decrease is
 observed with respect to the radar-only retrieval for both scenes. Since the calculation of the AVK involves the forward model
 Jacobian, this effect must be related to the non-linearity of the forward model.

3.2.4 Impact of assumed ice particle shape

To further investigate the effect of the assumed ice particle shape on the retrieval results, the mass density relations for the tested
 410 particle models are displayed in Panel (a) of Fig. 15. As can be seen from this plot, the GemCloudIce particle clearly stands out
 due to its large mass. Except for the fact that the GemSnow particle does not reach down to small particle sizes, the remaining
 particle models have quite similar in mass-size relations. The extreme density of the GemCloudIce particle model for large
 particle sizes likely explains the bad performance observed in the results presented above. Similarly, the bad performance of
 the GemSnow model in terms of retrieved IWC and IWP is likely due to it not covering small particle sizes.

415 Also displayed in Fig. 15 (panel (b) and (c)) are the χ_y^2 values of the combined retrieval obtained for the tested particle
 models. Since the particle shape has considerable effect on sub-millimeter observations (Ekelund et al., 2019), one could
 hope that the retrieval results can be used to infer the prevailing ice particle type based on the how well the retrieval can

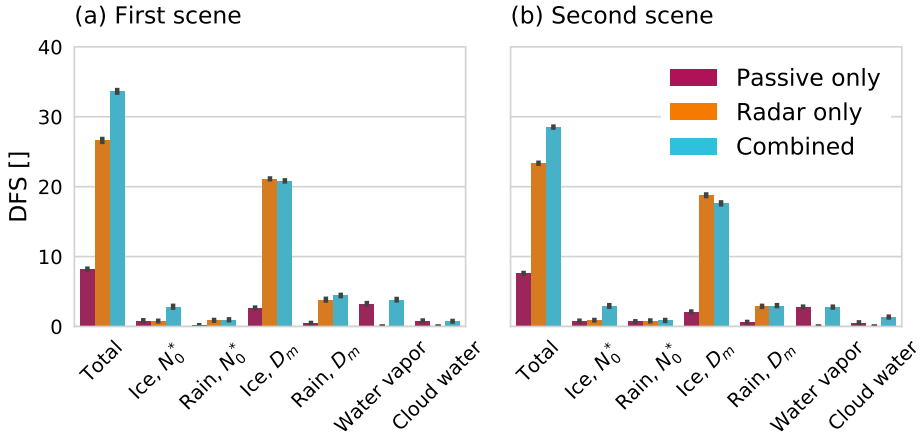


Figure 14. Distributions of degrees of freedom displayed as bar plots grouped by retrieval quantity and method. Results for the first test scene are displayed in Panel (a) and for the second test scene in Panel (b). Markers on the top of bars mark the extent of one standard deviation around the mean of each distribution.

fit the observations. Unfortunately, such clear conclusions cannot be drawn from the results. In the first test scene, the best fit is obtained by the GemSnow, GemCloudIce and the LargePlateAggregate particle models, although the GemSnow and
420 GemCloudIce models quite clearly yield the worst retrieval performance. For the second scene, similar results are observed. Here, the GemSnow particle consistently gives the lowest χ^2_y value but comparison with Fig. 11 clearly shows that it does not yield the best retrieval performance.

3.2.5 Humidity and cloud water

The developed passive and combined retrieval algorithms also retrieve profiles of humidity and liquid cloud mass density. For
425 relative humidity, both retrievals demonstrate sensitivity but no improvement could be observed in the results of the combined retrieval compared to the passive-only retrieval. Moreover, no suitable retrieval setup was found within the scope of this study which would yield throughout satisfactory performance. Since we do not consider our results representative of what could be achieved with the observational approach, they are not included here.

The liquid cloud retrieval, however, revealed an additional synergy of the radar and passive microwave observations. The
430 retrieval results are therefore shown in Fig. 16 to serve as a preview for potential additional applications of the combined retrieval approach. Panel (a) of the figure shows the reference and retrieved column-integrated LWC, here referred to as liquid water path (LWP). Although the total LWC is still underestimated, the combined observations clearly improve the LWP retrieval in all regions except those covered by thick clouds.

Panel (b) displays the reference LWC drawn as contours on top of the total hydrometeor content. Panel (c) and (d) show the
435 retrieved LWC drawn on top of the retrieved IWC for the passive-only and the combined retrieval. These results show clearly that the combined retrieval is able to detect and retrieve liquid clouds even when they overlap with ice clouds. Although some

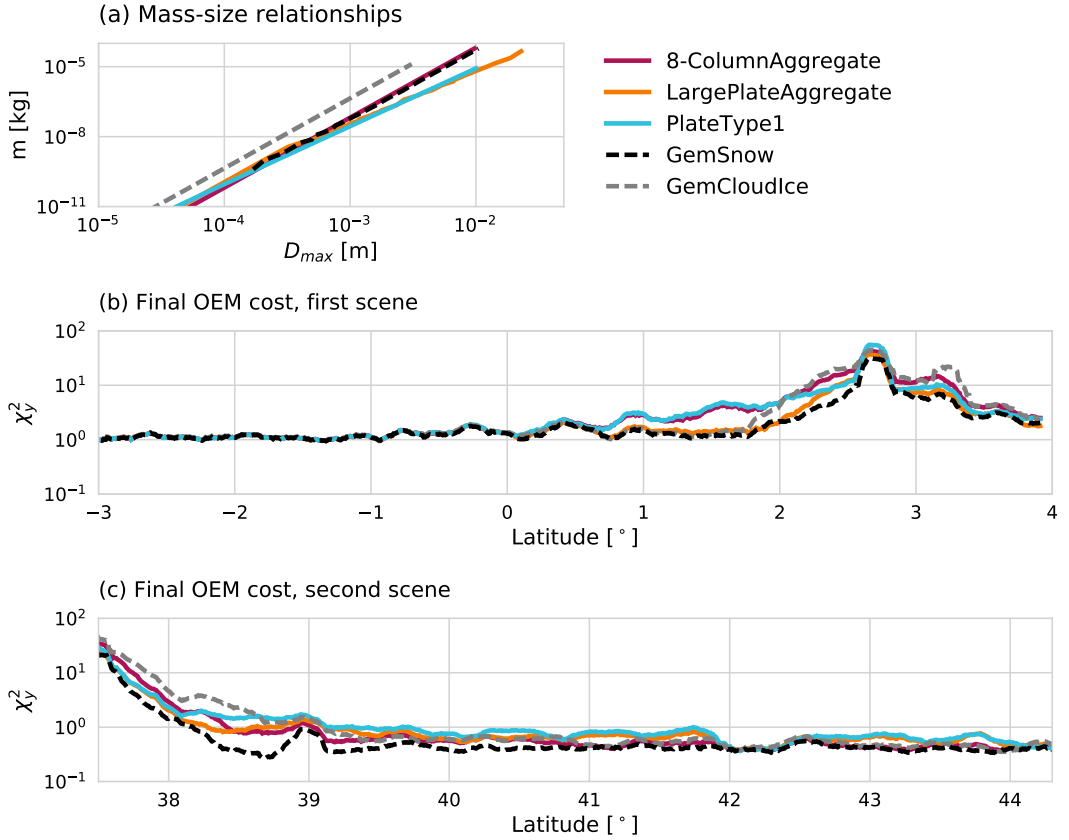


Figure 15. Mass-size relations (Panel (a)) and χ_y^2 values for the two test scenes (Panel (b) and (c)). The final cost curves were smoothed using a running average filter of a width of 20 profiles.

sensitivity of the passive-only retrieval to LWC can be observed as well, the retrieval puts the cloud too high in the troposphere and underestimates its LWC. This indicates that the radar reflectivity profile contains useful information for the retrieval to better locate cloud water in the atmospheric column.

440 4 Discussion

The principal aim of this study was to investigate the synergies between radar and passive sub-millimeter observations. To this end, a simplified numerical experiment has been presented, that qualitatively demonstrates the existence of complementary information in the radar and passive microwave observations. Furthermore, a combined retrieval algorithm has been developed to demonstrate the feasibility of the synergistic retrievals and further explore their potential as well as current limitations.

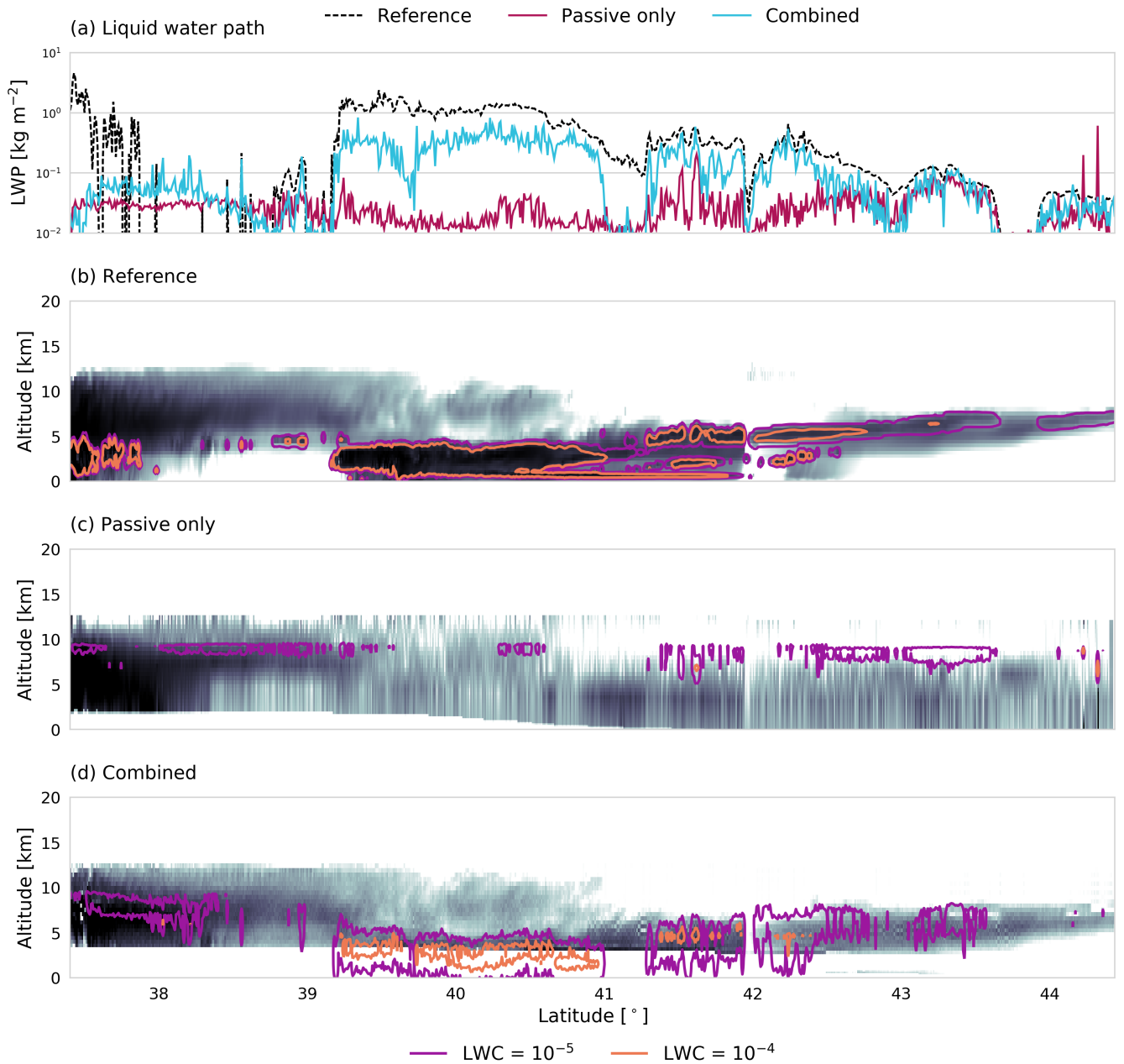


Figure 16. Reference and retrieved LWC. Panel (a) shows the reference and retrieved LWP for each profile. Panel (b) displays reference LWC contours drawn on top of the total hydrometeor content. Retrieval results for passive-only and combined retrieval are given in Panel (c) and (d).

445 **4.1 Fundamental synergies**

The experiment presented in the first part of this study aimed to establish the fundamental synergies of the active and passive microwave observations. It compared the cloud signals observed by a radar, a millimeter-wave radiometer and a sub-millimeter-wave radiometer. The results show that the combined observations can simultaneously constrain the horizontal and vertical scaling of the particle size distribution. However, the complementary information content between the active and passive observations depends on both the properties of the observed cloud and the frequency of the observations. For the lower frequencies considered in this study, i.e. the highest channels of the MWI radiometer, the regions where both observations provide complementary information on the particle size distribution of the cloud are limited to very high mass densities and particle sizes. It should be noted, however, that since the radar simulations neglect multiple scattering, the results are likely less accurate in this region of the cloud-parameter space. As the passive observing frequency increases, the regions of complementary information content extend down to smaller particle sizes and cloud mass density. Especially the highest-frequency channels of the ICI radiometer can therefore be expected to provide additional information on the particle size distribution of ice clouds.

450 **4.2 Combined cloud retrieval**

In the second part of the study, we have presented results from a combined, variational cloud retrieval applied to synthetic observations from two test scenes from a high-resolution atmosphere model. The results of the combined retrieval were compared to that of a passive- and a radar-only version of the retrieval algorithm. The simulated observations neglected potential errors caused by different or non-overlapping antenna beams as well as inhomogeneity of the atmosphere across the beams. On the other hand, a source of forward model error was included by applying a more complex microphysics scheme in the simulations than the one used in the retrieval. This allows assessing the retrieval error caused by the simplified modeling of cloud microphysics in the retrieval.

460 **4.2.1 Retrieval performance**

Of the three considered retrieval implementations, the passive-only retrieval clearly performs worst in terms of retrieved IWC. It should be noted, however, that the passive only retrieval presented here has not been fully optimized and should therefore not be taken as representative of the potential performance of the MWI and ICI radiometers for IWC retrievals. To ensure a fair comparison, the retrieval uses almost the same a priori assumptions as the other two retrievals, which in the presented case provide only very limited information on the vertical structure of the cloud. As has been shown also by other studies, the passive observations do provide information on the vertical distribution of ice in the atmospheric column (Wang et al., 2017; Grützun et al., 2018), but the information content is limited to a few degrees of freedom. It is therefore unlikely that the vertical resolution of the passive-only retrieval can be improved drastically without further constraining it a priori, as it is typically done in retrievals that use Monte Carlo integration or neural networks (Pfreundschuh et al., 2018).

With respect to IWP, however, the passive retrieval can perform as well or even better than the radar-only and the combined retrieval. Furthermore, the results in Figure 12 indicate that the passive observations provide some information on the particle number concentrations, which is not the case for the radar observations. This in itself is an interesting result as it shows that even when considered separately, observations from active and passive microwave sensors should be considered complementary to each other in their information content.

As expected, the radar-only retrieval provides much better IWC retrievals than the passive-only version. However, the results exhibit systematic deviations from the reference values in certain regions of the cloud. The analysis of the retrieval performance shown in Figure 7, 8 and 10 revealed that these are caused by systematic errors in the retrieval of specific hydrometeor species from the GEM model. A likely explanation for this is that the priori assumptions applied in the retrieval do not fit the specific microphysical properties of the species in the model. This hypothesis is confirmed by the radar-retrieved number density fields shown in Fig. 12 and Fig. 13. While the reference distribution has two modes corresponding to ice and snow, the retrieved values are nearly the same throughout the whole scene. Viewed from an information content perspective, this is plausible since the radar provides only one piece of independent information at each range gate, which is insufficient to determine the two degrees of freedom (N_0^* and D_m) of the PSD. The information on the second degree of freedom must therefore come from the a priori assumptions.

The a priori assumptions which were used in this study were similar but not identical to what is used in the DARDAR retrievals. Also here it should be noted, that the presented results should not be taken to be representative for the DARDAR product. Rather than this, the DARDAR a priori settings were chosen since they represent well established and validated assumptions for ice cloud retrievals and therefore should provide a reasonable starting point for the development of a combined cloud retrieval. The fact that the a priori assumptions used in the DARDAR retrieval do not agree with the microphysical properties of ice and snow in the GEM model, does not say much about the general validity of these assumptions.

Despite the certain visible artifacts in the retrieved IWC field (Fig. 6), the analysis of the results of the combined retrieval presented in Figs. 7, 8 and in particular 11 shows that it yields, at least for most of the tested particle models, the best retrieval performance for IWC and IWP. The benefit of the combined observations is even more pronounced in the retrieved number density fields (Fig. 12). Here, the passive- and radar-only retrieval showed little to no skill in retrieving the particle number concentrations. The combined retrieval, however, was able to reproduce the general structure of the number concentration fields in regions where the cloud composition is homogeneous (Fig. 13). In particular this showed that the combined retrieval is able to distinguish the microphysical properties of ice and snow in the model.

4.2.2 Impact of the assumed particle shape

Although the combined retrieval can reduce systematic errors in the retrieved IWC and IWP, its performance can even degrade if an unrealistic particle habit is used, as observed in Fig. 11. In general, the passive-only and the combined retrievals display stronger sensitivity to the assumed particle shape than the radar-only retrieval. This is plausible since the increased sensitivity especially of the sub-millimeter radiometer channels has been highlighted in several studies (Ekelund and Eriksson, 2019; Fox et al., 2019).

510 Given the increased sensitivity of the passive-only and combined retrieval to the assumed particle shape, it would be desirable to know which of the properties of a particle model are most critical for its representativeness. Five different particle models were tested here: The two most dominant from the GEM model and three additional models taken from the ARTS SSDB. The two GEM particles both showed the worst retrieval performance. For the GemCloudIce model, a likely explanation for its bad performance is its very high density. The GemSnow model has similar density as the 8-ColumnAggregate, but does not
515 reach down to small particle sizes, possibly explaining why it is unsuitable for the retrieval. Nonetheless, small performance differences are observed also for the other three models, but no clear connection to their mass-size relation can be established. This indicates that also its specific scattering properties are important factors that determine representativeness of a particle model.

Furthermore, it has been briefly investigated whether the goodness of the fit to the observations can provide information on
520 the suitability of the chosen particle model. In particular, we aimed to address the question whether the combined observations can constrain the dominant particle shape or whether a good fit to the observations can be obtained regardless of the applied particle model. Unfortunately, no evidence of a relation between the χ^2_y value and the retrieval performance was observed. It thus remains an open question whether and how information on the ice particle shape can be extracted from microwave observations of ice particles.

525 4.2.3 Humidity and cloud water

As an outlook, we have also included results from the liquid cloud retrieval, that clearly shows its capability to retrieve liquid
530 cloud mass densities even within mixed-phase clouds. Although certain sensitivity to cloud water is observed also for the passive-only retrieval, the addition of the radar signal clearly improved the localization of the cloud in the atmosphere. This explains the observed improvement in the retrieved LWP, since at lower altitude a thicker cloud is required to yield the same passive cloud signal. This shows that combined radar and microwave radiometer observations can also be used for the profiling of warm and supercooled liquid clouds.

Although no satisfactory results were obtained from the water vapor retrieval, the retrieval results still indicate sensitivity of this setup for retrieving atmospheric humidity. The full exploration of the potential of the combined observations for liquid cloud and water vapor is out of the scope of this study and is left to future investigation.

535 4.2.4 Retrieval method

The combined retrieval implementation showed robust performance on fairly distinct and complex cloud scenes. Despite this, both scenes that were considered here contained parts where the OEM minimization did not find a state that results in a good fit to the observations. In contrast to that, the radar-only retrieval did converge well in most regions where the final cost of the combined retrieval remained high. The inability of the retrieval to fit the observations indicates additional information that
540 is contained in the combined observations but which the retrieval method cannot disentangle. Furthermore, the results exhibit visible profile-to-profile variability as well as some artifacts in the form of high-frequency vertical oscillation. We have tried to counteract these by increasing the vertical spatial correlation but to no avail.

This raises the question of the suitability of the OEM method applied here. The combined retrieval violates the two fundamental assumptions of the OEM method: The forward model is non-linear and the assumed Gaussian a priori assumptions do not describe reality very well. In addition to that, the current implementation of the retrieval is computationally very expensive. For further development of the combined retrieval concept it may therefore be advisable to revisit the applied retrieval method in search for a potentially more suitable alternative.

4.2.5 Limitations

Finally, it is important to consider the limitations of this study. The results presented here are purely based on simulations and restricted to two selected model test scenes. The validity of the presented results thus to some extent depends on how well cloud microphysics are represented in GEM model. While this may affect the specific performance results for the tested retrieval methods, the main findings of this work, namely that the combined retrieval shows greater sensitivity to the microphysical properties of ice hydrometeors than the radar- or passive-only retrievals, should be independent of the realism of the test scenes.

Furthermore, the forward simulations used to generate the synthetic observations do not consider beam filling issues, assume a slightly unrealistic viewing geometry and neglect multiple scattering in the radar simulations. For a realistic assessment of the potential retrieval performance this should certainly be taken into account. Again, it is important to understand the results presented here as a study of the fundamental synergies of active and passive microwave observations rather than an accurate performance assessment of the combined retrieval.

560 5 Conclusions

The main conclusions from the results presented above are:

1. The complementary information in active and passive microwave observations can constrain two degrees of freedom of the PSD of frozen hydrometeors.
2. This reduces systematic retrieval errors for specific hydrometeor species whose properties are not well described by the a priori assumptions.
3. Especially the sub-millimeter channels of the ICI radiometer contribute to the synergistic information content for ice particles.

In addition to this, the combined retrieval also shows improved profiling capabilities for warm and supercooled liquid clouds.

The results presented in this study particularly highlight the complementarity of the active and passive observations: Although the radar provides observations at high vertical resolution, they contain insufficient information on the microphysical properties of hydrometeors. The passive-only observations, on the contrary, have low vertical resolution, but are more sensitive to cloud microphysics allowing a potentially more accurate IWP retrieval than what can be obtained from the radar alone.

A synergistic retrieval using both types of observations allows combining the high vertical resolution of the radar with the sensitivity to cloud microphysics of the passive observations, which yields more accurate retrievals of IWC, IWP and particle number densities.

Synergistic retrievals from active and passive microwave observations ideally complement currently available observation systems that combine radar with observations in the visible or infrared. The advantage of combined microwave observations is that they provide sensitivity throughout the whole cloud, where visible and infrared observations would be saturated. Where only information from the radar is available, a retrieval based on optical or infrared observations has to rely on a priori assumptions, which may cause similar systematic errors as what has been observed in this study. In addition to this, our results underline the benefits of ICI's sub-millimeter channels, which significantly improve the sensitivity of the passive observations to smaller particle sizes and mass densities and thus narrow the sensitivity gap between the observing frequencies of traditional microwave imagers and observations in the infrared and visible domain.

The upcoming launch of the ICI and MWI radiometers thus provides a great opportunity for a potential synergistic cloud-radar missions. Such a mission would have a unique scientific value for the study of frozen hydrometeors because of its ability to better determine the microphysical properties of hydrometeors even inside of thick clouds. Since such information is currently simply not available at a global scale, such a mission would be valuable not only in itself but also for other earth observation systems by establishing more reliable a priori assumptions on cloud microphysics.

The results presented in this study not only show the potential of the combined retrieval approach but also demonstrate its feasibility. Although further work will be required to fully understand the effect of particle shape and PSD, the concept is mature enough to be applied to real observations. Since airborne demonstrators of sub-millimeter radiometers are available already today, the combined retrievals could be applied in future field campaigns to study ice cloud microphysics.

Overall, the combined active and passive microwave retrievals are a promising concept that deserves further exploration. Regardless whether airborne or spaceborne, combined active and passive microwave observations have great potential to improve the understanding of the microphysical properties of ice hydrometeors.

Code availability. All code used to produce the results in this study is publicly available online. (Simon Pfreundschuh, 2019).

Data availability. Data to reproduce the simulations leading to the presented results will be made available on request.

Author contributions. Simon Pfreundschuh has implemented the retrieval, performed the data analysis and written the manuscript. Patrick Eriksson and Richard Larsson have added code to the ARTS radiative transfer model that was required to perform the presented calculations. Stefan A. Buehler, Patrick Eriksson, Manfred Brath and Simon Pfreundschuh have collaborated on the study that lead to the results presented here. David Duncan and Robin Ekelund have contributed to the conceptualization of the study through comments and advice.

Competing interests. No competing interests are present.

Acknowledgements. The combined and radar-only were developed as part of the ESA-funded study “Scientific Concept Study for Wide-Swath High-Resolution Cloud Profiling” (Contract number: 4000119850/17/NL/LvH). The authors would like to thank study manager Tobias Wehr for his valuable input and guidance.

Furthermore, the authors would like to acknowledge the work of Zhipeng Qu, Howard Barker, and Jason Cole from Environment and Climate Change Canada who produced the model scenes that were used to test the retrieval.

The work of SP, PE and RE on this study was financially supported by the Swedish National Space Agency (SNSA) under grants 150/14 and 166/18.

SB was supported by the Deutsche Forschungsgemeinschaft (DFG, German Research Foundation) under Germany’s Excellence Strategy — EXC 2037 ’Climate, Climatic Change, and Society’ — Project Number: 390683824, contributing to the Center for Earth System Research and Sustainability (CEN) of Universität Hamburg.

The computations for this study were performed using several freely available programming languages and software packages, most prominently the Python language (The Python Language Foundation, 2018), the IPython computing environment (Perez and Granger, 2007), the numpy package for numerical computing (van der Walt et al., 2011) and matplotlib for generating figures (Hunter, 2007).

References

- Aires, F., Prigent, C., Buehler, S. A., Eriksson, P., Milz, M., and Crewell, S.: Towards more realistic hypotheses for the information content analysis of cloudy/precipitating situations – Application to a hyperspectral instrument in the microwave, *Q. J. R. Meteorol. Soc.*, 145, 1–14, <https://doi.org/10.1002/qj.3315>, <https://rmets.onlinelibrary.wiley.com/doi/abs/10.1002/qj.3315>, 2019.
- 620 Birman, C., Mahfouf, J.-F., Milz, M., Mendrok, J., Buehler, S. A., and Brath, M.: Information content on hydrometeors from millimeter and sub-millimeter wavelengths, *Tellus*, 69, 1271562, <https://doi.org/10.1080/16000870.2016.1271562>, <https://doi.org/10.1080/16000870.2016.1271562>, 2017.
- Bony, S., Stevens, B., Frierson, D. M., Jakob, C., Kageyama, M., Pincus, R., Shepherd, T. G., Sherwood, S. C., Siebesma, A. P., Sobel, A. H., et al.: Clouds, circulation and climate sensitivity, *Nat. Geosci.*, 8, 261, <https://doi.org/10.1038/ngeo2398>, 2015.
- 625 Brath, M., Fox, S., Eriksson, P., Harlow, R. C., Burgdorf, M., and Buehler, S. A.: Retrieval of an ice water path over the ocean from ISMAR and MARSS millimeter and submillimeter brightness temperatures, *Atmos. Meas. Tech.*, 11, 611–632, <https://doi.org/10.5194/amt-11-611-2018>, <https://www.atmos-meas-tech.net/11/611/2018/>, 2018.
- Buehler, S. A., Mendrok, J., Eriksson, P., Perrin, A., Larsson, R., and Lemke, O.: ARTS, the Atmospheric Radiative Transfer Simulator – version 2.2, the planetary toolbox edition, *Geosci. Model Dev.*, 11, 1537–1556, <https://doi.org/10.5194/gmd-11-1537-2018>, <https://www.geosci-model-dev.net/11/1537/2018/>, 2018.
- 630 Cazenave, Q., Ceccaldi, M., Delanoë, J., Pelon, J., Groß, S., and Heymsfield, A.: Evolution of DARDAR-CLOUD ice cloud cloud retrieval: new parameters and impacts on the retrieved microphysical properties, *Atmos. Meas. Tech. Discuss.*, 2018, 1–24, <https://doi.org/10.5194/amt-2018-397>, <https://www.atmos-meas-tech-discuss.net/amt-2018-397/>, 2018.
- Côté, J., Gravel, S., Méthot, A., Patoine, A., Roch, M., and Staniforth, A.: The operational CMC–MRB global environmental multi-scale (GEM) model. Part I: Design considerations and formulation, *Mon. Weather Rev.*, 126, 1373–1395, [https://doi.org/10.1175/1520-0493\(1998\)126<1373:TOCMGE>2.0.CO;2](https://doi.org/10.1175/1520-0493(1998)126<1373:TOCMGE>2.0.CO;2), 1998.
- 635 Delanoë, J., Protat, A., Testud, J., Bouniol, D., Heymsfield, A. J., Bansemer, A., Brown, P., and Forbes, R.: Statistical properties of the normalized ice particle size distribution, *J. Geophys. Res.-Atmos.*, 110, <https://doi.org/10.1029/2004JD005405>, 2005.
- Delanoë, J., Heymsfield, A., Protat, A., Bansemer, A., and Hogan, R.: Normalized particle size distribution for remote sensing application, *J. 640 Geophys. Res.-Atmos.*, 119, 4204–4227, <https://doi.org/10.1002/2013JD020700>, 2014.
- Duncan, D. I. and Eriksson, P.: An update on global atmospheric ice estimates from satellite observations and reanalyses, *Atmos. Chem. Phys.*, 18, 11 205, <https://doi.org/10.5194/acp-18-11205-2018>, <https://search.proquest.com/docview/2087361828?accountid=11162>, 2018.
- Ekelund, R. and Eriksson, P.: Impact of ice aggregate parameters on microwave and sub-millimetre scattering properties, *J. Quant. Spectrosc. 645 Radiat. Transfer*, 224, 233 – 246, <https://doi.org/https://doi.org/10.1016/j.jqsrt.2018.11.013>, <http://www.sciencedirect.com/science/article/pii/S0022407318303984>, 2019.
- Ekelund, R., Eriksson, P., and Pfreundschuh, S.: Using passive and active microwave observations to constrain ice particle models, *Atmospheric Measurement Techniques Discussions*, 2019, 1–30, <https://doi.org/10.5194/amt-2019-293>, <https://www.atmos-meas-tech-discuss.net/amt-2019-293/>, 2019.
- 650 Eliasson, S., Buehler, S. A., Milz, M., Eriksson, P., and John, V. O.: Assessing observed and modelled spatial distributions of ice water path using satellite data, *Atmos. Chem. Phys.*, 11, 375–391, <https://doi.org/10.5194/acp-11-375-2011>, <https://www.atmos-chem-phys.net/11/375/2011/>, 2011.

- Eriksson, P., Ekelund, R., Mendrok, J., Brath, M., Lemke, O., and Buehler, S. A.: A general database of hydrometeor single scattering properties at microwave and sub-millimetre wavelengths, *Earth Syst. Sci. Data*, 10, 1301–1326, <https://doi.org/10.5194/essd-10-1301-2018>, 2018.
- Eriksson, P., Rydberg, B., Mattioli, V., Thoss, A., Accadia, C., Klein, U., and Buehler, S. A.: Towards an operational Ice Cloud Imager (ICI) retrieval product, *Atmos. Meas. Tech.*, 2019, 1–30, <https://doi.org/10.5194/amt-2019-312>, <https://www.atmos-meas-tech-discuss.net/amt-2019-312/>, 2019.
- Evans, K. F., Wang, J. R., Racette, P. E., Heymsfield, G., and Li, L.: Ice Cloud Retrievals and Analysis with the Compact Scanning Submillimeter Imaging Radiometer and the Cloud Radar System during CRYSTAL FACE, *J. Appl. Meteorol.*, 44, 839–859, <https://doi.org/10.1175/JAM2250.1>, <https://doi.org/10.1175/JAM2250.1>, 2005.
- Fox, S., Mendrok, J., Eriksson, P., Ekelund, R., O’Shea, S. J., Bower, K. N., Baran, A. J., Harlow, R. C., and Pickering, J. C.: Airborne validation of radiative transfer modelling of ice clouds at millimetre and sub-millimetre wavelengths, *Atmos. Meas. Tech.*, 12, 1599–1617, <https://doi.org/10.5194/amt-12-1599-2019>, <https://www.atmos-meas-tech.net/12/1599/2019/>, 2019.
- Geer, A. J., Baordo, F., Bormann, N., Chambon, P., English, S. J., Kazumori, M., Lawrence, H., Lean, P., Lonitz, K., and Lupu, C.: The growing impact of satellite observations sensitive to humidity, cloud and precipitation, *Q. J. R. Meteorol. Soc.*, 143, 3189–3206, <https://doi.org/10.1002/qj.3172>, <https://rmets.onlinelibrary.wiley.com/doi/abs/10.1002/qj.3172>, 2017.
- Grecu, M., Olson, W. S., Munchak, S. J., Ringerud, S., Liao, L., Haddad, Z., Kelley, B. L., and McLaughlin, S. F.: The GPM Combined Algorithm, *J. Atmos. Oceanic Technol.*, 33, 2225–2245, <https://doi.org/10.1175/JTECH-D-16-0019.1>, <https://doi.org/10.1175/JTECH-D-16-0019.1>, 2016.
- Grützun, V., Buehler, S. A., Kluft, L., Mendrok, J., Brath, M., and Eriksson, P.: All-sky information content analysis for novel passive microwave instruments in the range from 23.8 to 874.4 GHz, *Atmos. Meas. Tech.*, 11, 4217–4237, <https://doi.org/10.5194/amt-11-4217-2018>, <https://www.atmos-meas-tech.net/11/4217/2018/>, 2018.
- Hou, A. Y., Kakar, R. K., Neeck, S., Azarbarzin, A. A., Kummerow, C. D., Kojima, M., Oki, R., Nakamura, K., and Iguchi, T.: The Global Precipitation Measurement Mission, *Bull. Amer. Met. Soc.*, 95, 701–722, <https://doi.org/10.1175/BAMS-D-13-00164.1>, <https://doi.org/10.1175/BAMS-D-13-00164.1>, 2014.
- Hunter, J. D.: Matplotlib: A 2D graphics environment, *Comput. Sce. Eng.*, 9, 90–95, <https://doi.org/10.1109/MCSE.2007.55>, 2007.
- Jiang, J. H., Yue, Q., Su, H., Kangaslahti, P., Lebsack, M., Reising, S., Schoeberl, M., Wu, L., and Herman, R. L.: Simulation of Remote Sensing of Clouds and Humidity From Space Using a Combined Platform of Radar and Multifrequency Microwave Radiometers, *Earth Space. Sci.*, 6, 1234–1243, <https://doi.org/10.1029/2019EA000580>, <https://agupubs.onlinelibrary.wiley.com/doi/abs/10.1029/2019EA000580>, 2019.
- Jiménez, C., Buehler, S., Rydberg, B., Eriksson, P., and Evans, K.: Performance simulations for a submillimetre-wave satellite instrument to measure cloud ice, *Q. J. R. Meteorol. Soc.*, 133, 129–149, <https://doi.org/10.1002/qj.134>, 2007.
- Liebe, H. J., Hufford, G. A., and Cotton, M. G.: Propagation modeling of moist air and suspended water/ice particles at frequencies below 1000 GHz, in: AGARD conference proceedings 542: Atmospheric propagation effects through natural and man-made obscurants for visible to mm-wave radiation, pp. 3.1–3.10, Palma de Mallorca, Spain, 17–20 May 1993, 1993.
- Milbrandt, J. and Yau, M.: A multimoment bulk microphysics parameterization. Part II: A proposed three-moment closure and scheme description, *J. Atmos. Sci.*, 62, 3065–3081, <https://doi.org/10.1175/JAS3534.1>, 2005.
- Perez, F. and Granger, B. E.: IPython: A System for Interactive Scientific Computing, *Computing in Science Engineering*, 9, 21–29, <https://doi.org/10.1109/MCSE.2007.53>, 2007.

- Pfreundschuh, S., Eriksson, P., Duncan, D., Rydberg, B., Håkansson, N., and Thoss, A.: A neural network approach to estimating a posteriori distributions of Bayesian retrieval problems, *Atmos. Meas. Tech.*, 11, 4627–4643, <https://doi.org/10.5194/amt-11-4627-2018>, <https://www.atmos-meas-tech.net/11/4627/2018/>, 2018.
- Prigent, C., Aires, F., Wang, D., Fox, S., and Harlow, C.: Sea-surface emissivity parametrization from microwaves to millimetre waves, *Q. J. R. Meteorol. Soc.*, 143, 596–605, <https://doi.org/10.1002/qj.2953>, <https://rmets.onlinelibrary.wiley.com/doi/abs/10.1002/qj.2953>, 2017.
- Rodgers, C. D.: Inverse methods for atmospheric sounding: theory and practice, vol. 2, World scientific, <https://doi.org/10.1142/3171>, 2000.
- Rosenkranz, P. W.: Absorption of microwaves by atmospheric gases, in: Atmospheric remote sensing by microwave radiometry, edited by Janssen, M. A., pp. 37–90, John Wiley and Sons, Inc., New York, USA, 1993.
- Rosenkranz, P. W.: Water vapor microwave continuum absorption: A comparison of measurements and models, *Radio Sci.*, 33, 919–928, <https://doi.org/10.1029/98RS01182>, 1998.
- Simon Pfreundschuh: mcrf – A microwave cloud retrieval framework, <https://github.com/simonpf/mcrf>, <https://doi.org/10.5281/zenodo.3467316>, 2019.
- Stamnes, K., Tsay, S.-C., Wiscombe, W., and Laszlo, I.: DISORT, a general-purpose Fortran program for discrete-ordinate-method radiative transfer in scattering and emitting layered media: documentation of methodology, Tech. rep., Tech. rep., Dept. of Physics and Engineering Physics, Stevens Institute of . . . , 2000.
- Stephens, G. L., Vane, D. G., Boain, R. J., Mace, G. G., Sassen, K., Wang, Z., Illingworth, A. J., O’connor, E. J., Rossow, W. B., Durden, S. L., Miller, S. D., Austin, R. T., Benedetti, A., and Mitrescu, C. a.: THE CLOUDSAT MISSION AND THE A-TRAIN, *Bull. Amer. Met. Soc.*, 83, 1771–1790, <https://doi.org/10.1175/BAMS-83-12-1771>, <https://doi.org/10.1175/BAMS-83-12-1771>, 2002.
- Tanelli, S., Durden, S. L., Im, E., Pak, K. S., Reinke, D. G., Partain, P., Haynes, J. M., and Marchand, R. T.: CloudSat’s Cloud Profiling Radar After Two Years in Orbit: Performance, Calibration, and Processing, *IEEE T. Geosci. Remote*, 46, 3560–3573, <https://doi.org/10.1109/TGRS.2008.2002030>, 2008.
- The Python Language Foundation: The Python Language Reference, <https://docs.python.org/3/reference/index.html>, 2018.
- van der Walt, S., Colbert, S. C., and Varoquaux, G.: The NumPy Array: A Structure for Efficient Numerical Computation, *Computing in Science Engineering*, 13, 22–30, <https://doi.org/10.1109/MCSE.2011.37>, 2011.
- Waliser, D. E., Li, J.-L. F., Woods, C. P., Austin, R. T., Bacmeister, J., Chern, J., Del Genio, A., Jiang, J. H., Kuang, Z., Meng, H., Minnis, P., Platnick, S., Rossow, W. B., Stephens, G. L., Sun-Mack, S., Tao, W.-K., Tompkins, A. M., Vane, D. G., Walker, C., and Wu, D.: Cloud ice: A climate model challenge with signs and expectations of progress, *J. Geophys. Res.-Atmos.*, 114, <https://doi.org/10.1029/2008JD010015>, <https://agupubs.onlinelibrary.wiley.com/doi/abs/10.1029/2008JD010015>, 2009.
- Wang, D., Prigent, C., Aires, F., and Jimenez, C.: A Statistical Retrieval of Cloud Parameters for the Millimeter Wave Ice Cloud Imager on Board MetOp-SG, *IEEE Access*, 5, 4057–4076, <https://doi.org/10.1109/ACCESS.2016.2625742>, 2017.

Paper 2

Retrieving ice hydrometeors from radar and sub-millimeter observations: Validation of radiative transfer modeling and sensitivity to cloud microphysics

S. Pfreundschuh, P. Eriksson, S. A. Buehler, M. Brath, D. Duncan, S. Fox, F. Ewald, J. Delanoë

Manuscript in preparation

**Paper 2. Retrieving ice hydrometeors from radar
and sub-millimeter observations: Validation of
radiative transfer modeling and sensitivity to
cloud microphysics**

S. Pfreundschuh, P. Eriksson, S. A. Buehler, M. Brath, D. Duncan, S. Fox,
F. Ewald, J. Delanoë

Retrieving ice hydrometeors from radar and sub-millimeter observations: Validation of radiative transfer modeling and sensitivity to cloud microphysics

Simon Pfreundschuh¹, Patrick Eriksson¹, Stefan A. Buehler², Manfred Brath², David Duncan³, Stuart Fox⁴, Florian Ewald⁵, and Julien Delanoë⁶

¹Department of Space, Earth and Environment, Chalmers University of Technology, 41296 Gothenburg, Sweden

²Meteorologisches Institut, Fachbereich Geowissenschaften, Centrum für Erdsystem und Nachhaltigkeitsforschung (CEN), Universität Hamburg, Bundesstraße 55, 20146 Hamburg, Germany

³ECMWF, Shinfield Park, Reading RG2 9AX, United Kingdom

⁴Met Office, FitzRoy Road, Exeter, EX1 3PB, United Kingdom

⁵Institut für Physik der Atmosphäre, Deutsches Zentrum für Luft- und Raumfahrt, Münchener Straße 20, 82234 Oberpfaffenhofen-Wessling

⁶Laboratoire Atmosphère, Milieux, et Observations Spatiales, Guyancourt, France

Correspondence: Simon Pfreundschuh (simon.pfreundschuh@chalmers.se)

Abstract. Clouds in the troposphere and their properties remain badly constrained by the global observational record despite their importance for the validation of climate models and numerical weather prediction. The upcoming launch of the Ice Cloud Imager is designed to improve this situation by providing observations of clouds at sub-millimeter wavelengths. While these sub-millimeter observations provide increased sensitivity to small ice particles and their microphysical properties, they also

5 pose a considerable challenge for the modeling of the radiative transfer through these clouds. In this study a synergistic hydrometeor retrieval using observations from a 35 – GHz cloud radar and passive millimeter and sub-millimeter wave radiometers is applied to observations of a mid-latitude cloud system from the North Atlantic Waveguide and Downstream Impact Experiment. This case study is used to validate the retrieval by comparison to in-situ data and considering the closure with respect to radar observations at 95 GHz. Good agreement is found in the retrieved mass- and number-densities. Although the results
10 are sensitive to the ice particle model employed in the retrieval forward model, this dependence is found to be consistent with the microphysical properties derived from in-situ data. The good fit achieved by the retrieval to the observations for most parts of the scene prove the consistency of the radiative transfer modeling across the millimeter and sub-millimeter domain. Two regions where the forward model fails to fit the observations were identified and indicate the potential presence of a signal from mixed-phase particles in convective updrafts. This study provides an important validation case for the applied synergistic
15 retrieval algorithm as well as the radiative transfer modeling of ice hydrometeors at sub-millimeter frequencies. In addition to that, it points towards potential new applications of combined radar/radiometer observations for studying microphysical properties of hydrometeors in convective updrafts.

1 Introduction

With the upcoming launch of the Ice Cloud Imager (ICI) onboard the second generation of European operational meteorological satellites (Metop-SG), sub-millimeter observations of clouds will reach operational status. These observations will provide valuable information for numerical weather prediction (NWP, Geer et al. (2017)) and improve observational constraints on atmospheric ice in global climate models (Waliser et al., 2009; Eliasson et al., 2011; Duncan and Eriksson, 2018).

Compared to traditional microwave frequencies around 183 GHz and below, observations in the sub-millimeter range are sensitive not only to smaller particle sizes and lower mass concentrations (Buehler et al., 2012), but also to the shape of the hydrometeors in the cloud (Evans et al., 1998). On one hand, this increases the complexity the radiative transfer calculations at these frequencies, but on the other, it should also allow these observations to be used to study the microphysical properties of clouds.

So far the availability of observations of clouds at sub-millimeter wavelengths remains limited. In the upper troposphere, observations have been obtained as by-products of space-borne limb-sounding missions aimed to study gases in the stratosphere. Retrievals of ice mass concentrations using sub-millimeter limb-sounding observations were developed for AURA MLS (Wu et al., 2006), Odin/SMR (Eriksson et al., 2007) and SMILES (Millán et al., 2013; Eriksson et al., 2014). In addition to this, several airborne sensors have been developed and used to study clouds in field campaigns. Examples are the Millimeter-wave imaging radiometer (MIR, Wang et al. (2001)), the Compact Scanning Submillimeter Imaging Radiometer (CoSSIR, Evans et al. (2005)) and the International Sub-Millimeter Airborne Radiometer (ISMAR, Fox et al. (2017)).

Due to the scarcity of cloud observations at sub-millimeter wavelengths, efforts to validate the radiative transfer modeling through clouds at these frequencies have been limited. The only two notable efforts that directly tried to validate the radiative transfer are the study by Evans et al. (2005), who compared the observed column-integrated radar backscatter to values retrieved from sub-millimeter observations, and Fox et al. (2019), who performed a closure study based on lidar and in-situ observations of hydrometeors. Although both of them obtained good agreement between simulations and observations, they were both limited to cirrus clouds. Radiative transfer in cloudy atmospheres at sub-millimeter wavelengths therefore remains afflicted with considerable uncertainties, not only because microphysical properties of clouds are difficult to constrain a priori, but also because of the lack of validation efforts for cloud types other than cirrus clouds.

In this study, a recently developed, variational hydrometeor retrieval (Pfreundschuh et al., 2019) is applied to radar and microwave radiometer observations from a recent flight campaign. The aim of this study is to validate the retrieval algorithm and the radiative transfer modeling upon which its implementation is based. The observations were acquired by the High Altitude and Long Range Research Aircraft (HALO), the Facility for Airborne Atmospheric Measurements (FAAM) and the Service des Avions Francais Instrumentations pour la Recherche en Environnement (SAFIRE) research aircraft during a joint flight performed as part of the North Atlantic Waveguide and Downstream Impact Experiment (NAWDEX, Schäfle et al. (2018)). The remote sensing observations made by the three research aircraft are complemented by in-situ data collected by FAAM during a subsequent descent through the cloud. The flight is one of the rare occasions where sub-millimeter observations from the International Submillimetre Airborne Radiometer (ISMAR, Fox et al. (2017)) are available in combination with radar

observations, in this case from the HALO Microwave Package (HAMP) and Radar Aéroporté et Sol de Télédétection des propriétés nuAgeuses (RASTA) cloud radars.

The data from this flight provides a unique opportunity where in-situ data can be used to directly validate the retrieval
55 algorithm. In addition to validating the retrieval itself, its application to the flight-campaign observations serves as a landmark study, which may help to identify remaining issues regarding sub-millimeter radiative transfer in cloudy atmospheres. Since the variational hydrometeor retrieval fits a radiative transfer model to the observations, it can be applied in the same way as the model-to-satellite approach in data assimilation to identify model inconsistencies (Geer et al., 2018).

The approach taken here to validate the retrieval and the underlying radiative transfer modeling is as follows: As primary
60 consistency check the fits of the retrieval to the observations are assessed to ensure that the radiative transfer model can fit the observations. Following this, the results from the retrieval are compared with the in-situ measurements. Finally, the closure of the retrieved atmospheric states with respect to the observations from the RASTA radar, which has been excluded from the retrieval input, are used as an additional independent source of validation data.

The structure of this paper is as follows. The following section introduces the data and methods used in this study. Section 3
65 presents the microphysical properties of the cloud that are derived from in-situ measurements. Section 4 presents the results from the combined hydrometeor retrieval and the closure with respect to RASTA. The paper closes with a discussion of these results in Sec. 5 and conclusions in Sec. 6.

2 Data and methods

This section presents the joint flight campaign and the measurements from it that are used in this study. Following this, the
70 retrieval algorithm is presented briefly.

2.1 Combined HALO/FAAM/SAFIRE flight

The combined flight of the three research aircraft HALO, FAAM and SAFIRE, took place on 14 October 2016 as part of NAWDEX. The joint campaign consisted of a simultaneous overpass of a cloud system. After the overpass, FAAM performed a descent through the cloud during which in-situ measurement of cloud hydrometeors were collected. The flight path, located
75 off the western coast of Scotland, is displayed in Fig. 1.

A more detailed view of the flight paths of the three aircraft is provided in Fig. 2. Shown in the figure is how the flight paths of the FAAM and SAFIRE aircraft are related to the radar observations made by the HAMP radar on the HALO aircraft. Ellipses mark the locations of the FAAM and SAFIRE aircraft as HALO passed over them. A radar signal from the FAAM aircraft is clearly visible in the measured radar reflectivities confirming that the observations from the three aircraft can be
80 expected to be well co-located. Although much weaker, a similar signal is observed from the SAFIRE aircraft.

Also marked in the figure are the regions where observations were made over a land surface. At this stage, the combined retrieval does not make use of surface-contaminated observations due to the difficulty in estimating the surface emissivity at microwave frequencies. The combined retrieval therefore uses only observations from channels around 183 GHz and upwards

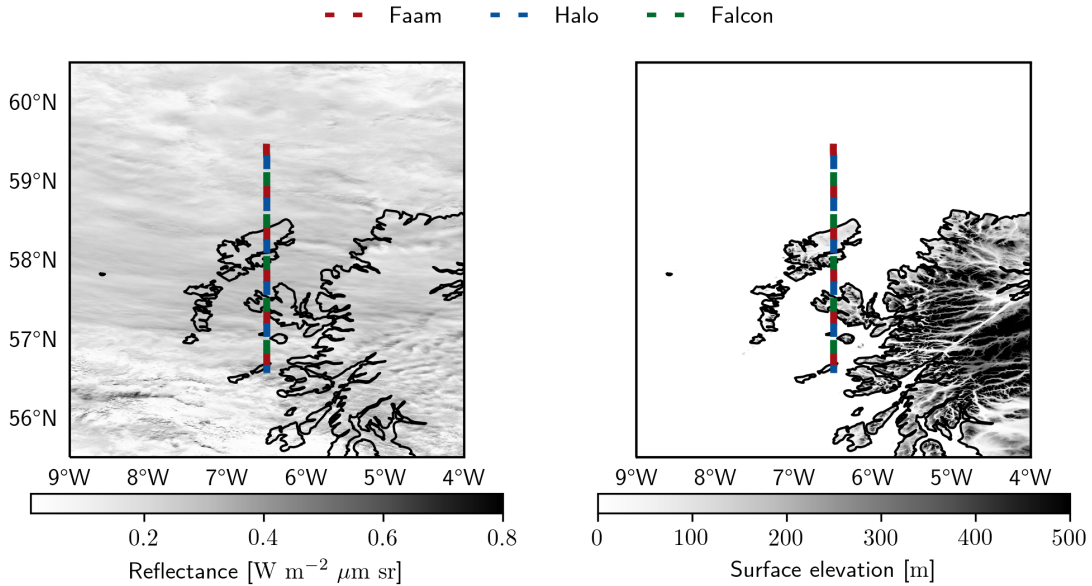


Figure 1. Flight paths of the coordinated cloud overpass. Panel (a) shows the flight paths of the three aircraft plotted onto the reflectivities at 650 nm measured by MODIS during the closest overpass of the TERRA satellite at 11:00 UTC. Panel (b) displays the flight paths overlaid onto the surface topography.

over land. Somewhat unfortunately, a considerable fraction of the observations of the cloud were performed over land, which
85 prevented making use of the full range of available radiometer channels for the affected profiles.

2.2 Remote sensing observations

During the overpass, the cloud system was observed using a wide range of sensors on each of the three aircraft. This study makes use of the radar and radiometer observations from the HALO Microwave Package (HAMP, Mech et al. (2014)), the microwave and sub-millimeter radiometer observations from the International Submillimetre Airborne Radiometer (ISMAR,
90 Fox et al. (2017)), which was flown on the FAAM aircraft, as well the radar observations from the Radar Aéroporté et Sol de Télédétection des propriétés nuAgeuses (RASTA) mounted on SAFIRE. However, only the HAMP and ISMAR observations are used in the combined retrieval. Due to their comparably low sensitivity and because the retrieval was developed for a single-frequency radar, the RASTA observations are not used to retrieve ice hydrometeors. Instead, the observations from RASTA are used to assess the retrieval results by comparing the simulated radar reflectivities to those observed by RASTA.

95 **2.2.1 HAMP radar**

The HAMP radar, which is flown on HALO, is a cloud radar operating at a frequency of 35 GHz. Although the standard resolution of the radar is 30 m, the observations have been downsampled to a resolution of 200 m due to computational constraints. The radar reflectivities from the cloud overpass are displayed in Fig. 2. Reflectivities in bins less than 250 m above the surface were assumed to be contaminated by ground clutter and set to the value found in the lowest bin above that threshold.

100 For the retrieval, also the reflectivities resulting from the overpasses of the FAAM and Falcon aircraft have been removed.

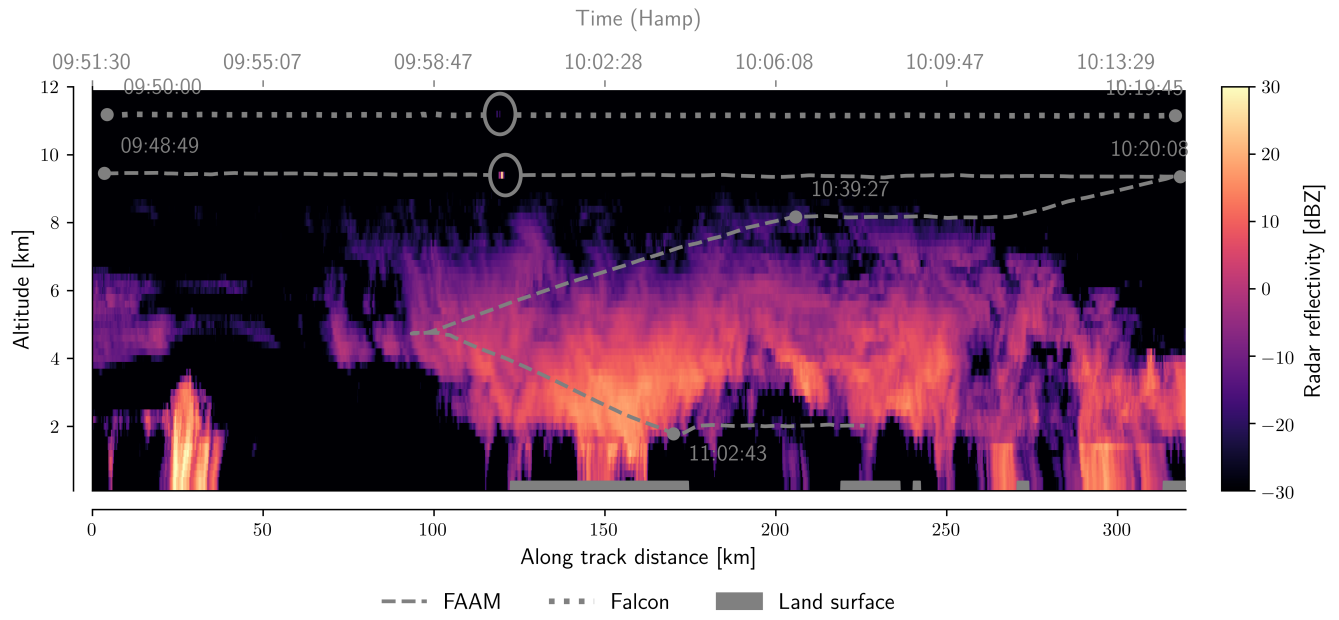


Figure 2. Radar reflectivities measured by the HAMP radar during the joint cloud overpass overlaid with the flight paths of the Falcon and FAAM aircraft. The ellipses mark the locations where HALO passed over the other two aircraft.

2.2.2 HAMP passive

The radiances observed by the passive HAMP channels are displayed in Fig. 3. The five bands of HAMP cover the frequency range from 22 to 183 GHz. All bands except the highest show a clear impact of the land surface in the regions marked by the grey background color. These bands are used in the combined retrieval only for profiles located over ocean due to the difficulty 105 of simulating microwave surface emissions over land. The assumed uncertainties for each channel are taken as the root of the squared sum of the noise-equivalent delta temperature and accuracy given in Tab. 2 in Mech et al. (2014).

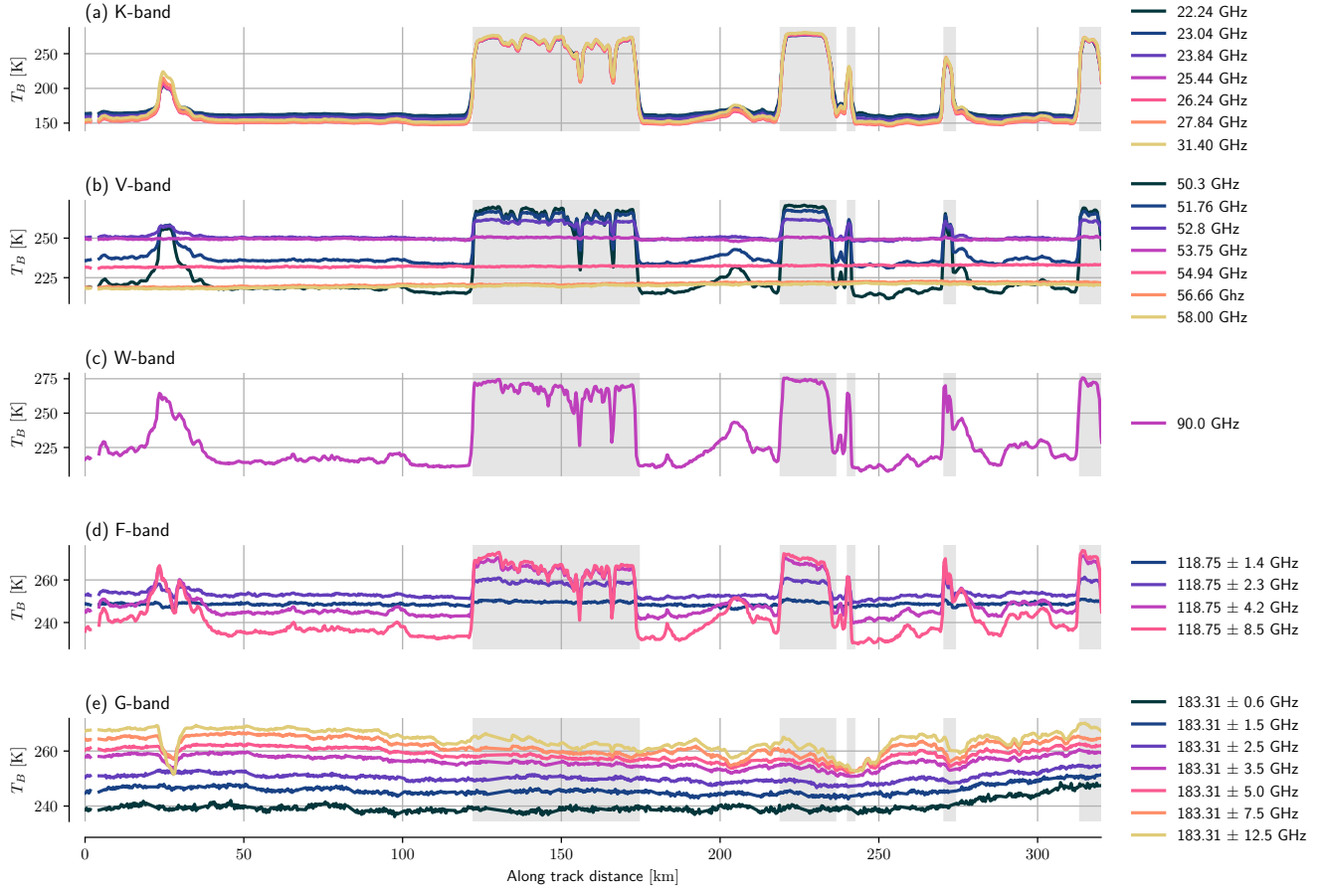


Figure 3. Brightness temperatures observed by the passive microwave channels of HAMP. The grey shading marks regions where observations are made over land surface.

2.2.3 ISMAR radiometer

On this flight, the ISMAR radiometer measured passive brightness temperatures covering a frequency range from 118 to 664 GHz. Unfortunately not all channels of ISMAR were available and produced observations of sufficient quality. For these

110 reasons only observations from the bands around 118, 248, 325 and 664 GHz were used from the flight. The observations were further restricted to views within $\pm 3^\circ$ off-nadir to simplify the co-location with the HAMP observations. The resulting observed brightness temperatures are displayed in Fig. 4. To co-locate the measurements with those made by HAMP, the ISMAR brightness temperatures were interpolated to the along track positions of the HAMP observations. Noise characteristics are taken from the estimated random errors provided with the ISMAR data.

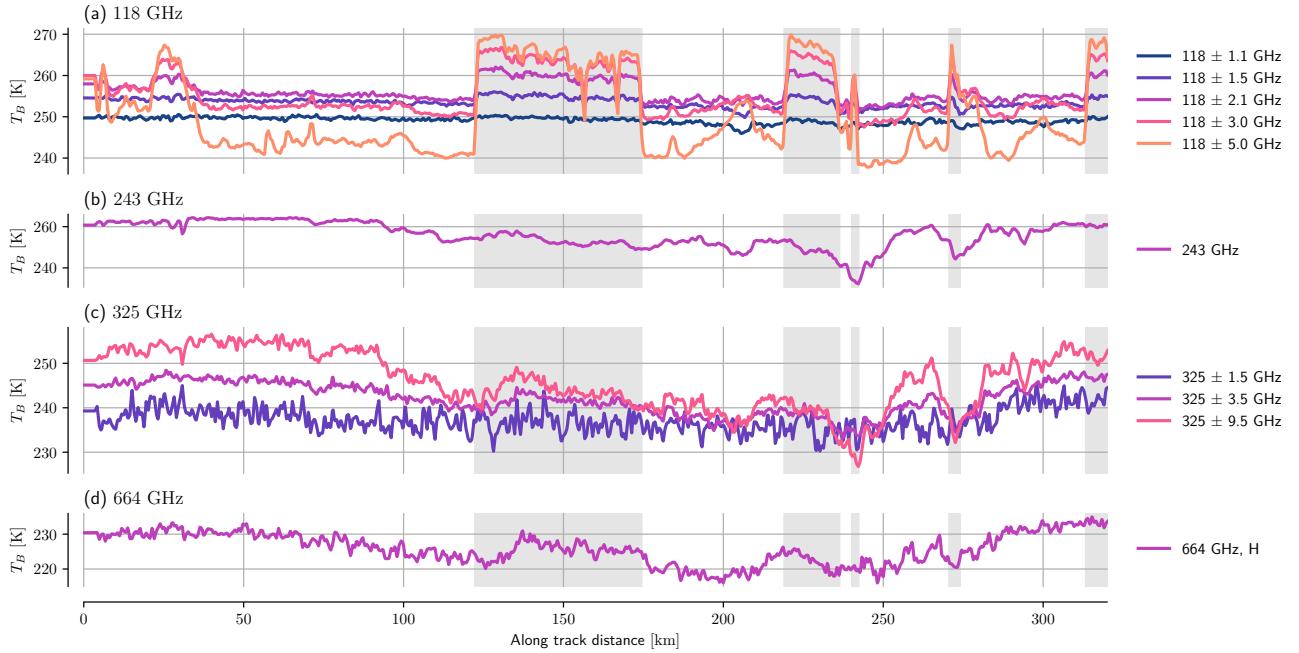


Figure 4. Brightness temperatures measured by ISMAR during the joint flight.

115 2.3 In-situ data

Following the coordinated cloud overpass, the FAAM aircraft made a descent to collect in-situ data on the hydrometeors in the cloud. The in-situ data used in this study are measurements of ice water content (IWC) as well as particle size distributions and particle images.

2.3.1 Liquid and frozen water content

120 Bulk total and liquid water content were measured during the descent using a deep-cone Nevezorov hot-wire probe (Korolev et al., 2013). The measurements were corrected using the baseline correction proposed by Abel et al. (2014). The ice water content is inferred from the difference of the measured mass densities. The measured ice and liquid water content profiles are displayed in Fig. 5. The IWC profile exhibits a region of relatively high IWC between 7 and 8 km. Below that, IWC decreases to 10^{-5} kg m⁻³ to then gradually increase up to reaching its maximum of about $2 \cdot 10^{-4}$ kg m⁻³ at an altitude of 2.5 km. The
125 profile exhibits a discontinuity at about 5 km where no significant IWC is measured, but this is likely due to the turn that the aircraft performed at this altitude. Water in the liquid phase was detected up to an altitude of 6 km but at concentrations about an order of magnitude less than those of ice.

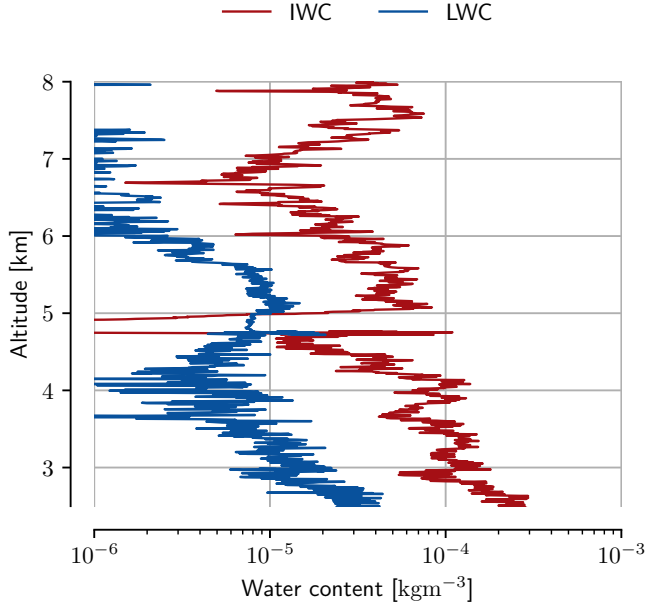


Figure 5. Ice and liquid water content measured by the Nevezorov probe during the descent through the cloud.

2.3.2 Particle size distributions

The FAAM aircraft also measured particle size distributions of hydrometeors during the descent through the cloud. The PSDs 130 were recorded using DMT CIP-15 and DMT CIP-100 probes, which have resolutions of 15 and 100 μm , respectively. Particle counts were measured for time intervals of 1s. Since particles smaller than 100 μm make up for a considerable fraction of the IWC in the upper parts of the observed cloud, it was decided to make use of the full range of size bins of the CIP-15 probe. To make up for the decreased sampling volume of these bins, the 1-second data has been averaged over 10-second intervals. The PSDs measured by the CIP-15 and CIP-100 probes are combined into a single measured PSD to simplify the analysis. For this, 135 the bins of the CIP-15 probe are used up to a size of 700 μm and the bins of the CIP-100 probe are used above that.

Fig. 6 displays averages of the PSDs measured over 10-second intervals for different altitudes. Solid lines display the mean PSD for the given altitude interval. The shading marks the extent of one standard deviation around the mean. Very high concentrations of small particles are observed at altitudes between 7 and 8 km. Between 6 and 7 km a significant decrease of particles smaller than 100 μm is observed. Below that, the concentrations of particles smaller than about 500 μm remains 140 fairly constant while the number of larger particles gradually increases. At altitudes between 2 and 3 kilometers particles were observed even in the largest size bins of the CIP probe. This indicates that even larger particle could have been present at these altitudes but have not been measured since they exceeded the maximum particle size of the CIP-100 probe.

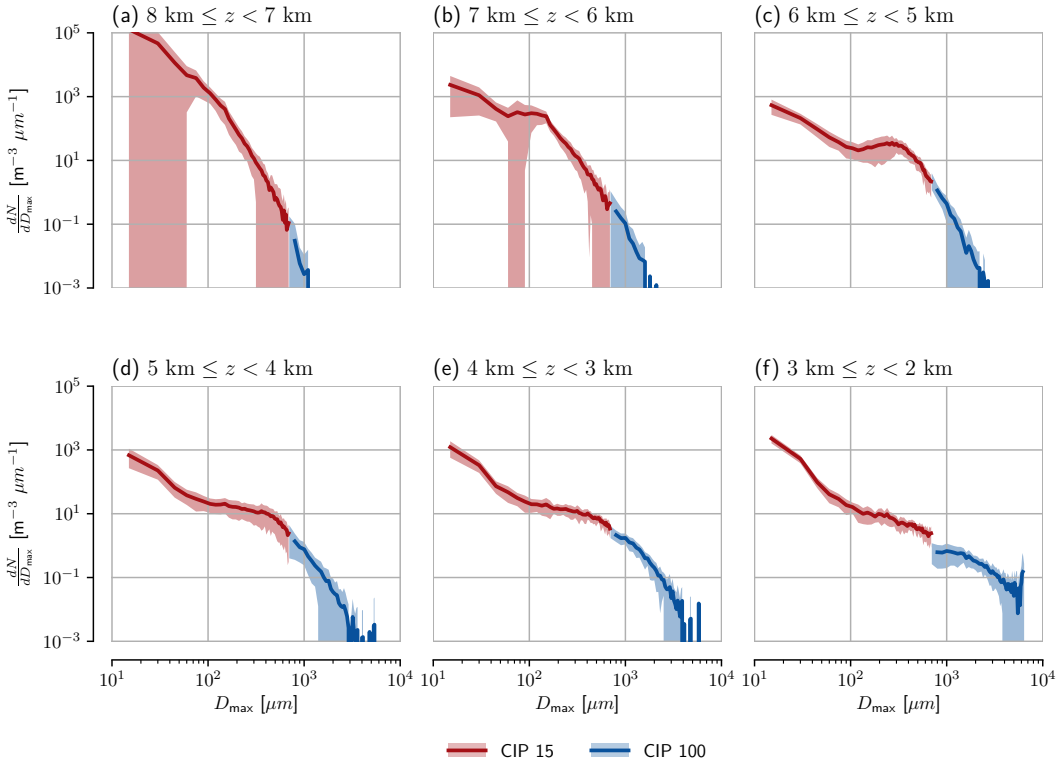


Figure 6. In-situ-measured PSDs for four different temperatures in the cloud. Each panel shows the PSDs measured by the CIP-15 probe, the CIP-100 probe and the combined PSD.

2.3.3 Particle images

The two CIP probes also record images of the ice particles that they sample. Since the raw images contain a large fraction of out-of-focus particles as well as a number of erroneous detections, a pre-processing loosely based on that from O’Shea et al. (2016) has been applied. Particle images were discarded if

- the minimum height or width was less than 6 pixels,
 - the center of mass of the particle lies outside the particle mask,
 - their height is one pixel over more than 50% of their width.
- 150 In addition to that, particles containing holes that make up more than 30% of their area were also discarded. The diameter of each imaged particle was determined by fitting an ellipse to the particle and using the length of its semi-major axis as its diameter.

To provide an overview of the different ice particle shapes that were encountered during the descent through the cloud, randomly-chosen particle images for different altitudes and particles sizes are displayed in Figure 7. All of the displayed particle

155 images have been rescaled uniformly to a size of 32×32 pixels. In this way, their shapes can be compared independently of their size. This, however, also means that size scales of different particle images are not comparable.

Comparing images across the different diameter ranges, a clear dependence of the shape on the particle size can be observed. At small sizes, the particles are relatively compact. As the size increases the shapes become more irregular. Above sizes of 500 μm most of the particles can be identified as aggregates. It further seems that above 1 mm the fractal dimension of the 160 shapes decreases. This, however, may be an artifact caused by the low resolution of the CIP-100 probe at sizes smaller than that. With respect to the altitude, no evident relationship to the shape of the particles can be observed.

2.4 Synergistic retrieval algorithm

In the following, a description of the synergistic retrieval algorithm that is used to retrieve frozen hydrometeors from the radar and radiometer observations is given. Since the algorithm is presented in full detail in Pfreundschuh et al. (2019), this section 165 provides only a brief overview over the algorithm and then focuses on the adaptations made to the original version.

2.4.1 Retrieval quantities

The principal retrieval quantity of the retrieval algorithm are frozen hydrometeors. Their distributions are retrieved in terms of two degrees of freedom of their PSD. In addition to that, liquid hydrometeors, liquid cloud water and water vapor are retrieved. In this study, however, only the retrieved frozen hydrometeors are considered.

170 The retrieval retrieves hydrometeor distribution column-by-column. The distributions are described using the normalized particle size distribution formalism proposed by Delanoë et al. (2005). The PSD $\frac{dN(D_{\text{eq}})}{dD_{\text{eq}}}$ of frozen hydrometeors, defined with respect to the volume-equivalent diameter D_{eq} , is described by a horizontal and a vertical scaling parameter at each altitude level in the atmospheric column. The horizontal scaling factor, D_m , is defined as the mass-weighted mean size of the PSD, i.e. the ratio of its fourth and third moment:

$$175 D_m = \frac{\int_0^\infty D_{\text{eq}}^4 \frac{dN(D_{\text{eq}})}{dD_{\text{eq}}} dD_{\text{eq}}}{\int_0^\infty D_{\text{eq}}^3 \frac{dN(D_{\text{eq}})}{dD_{\text{eq}}} dD_{\text{eq}}} \quad (1)$$

The vertical scaling factor, N_0^* , is defined as

$$N_0^* = \frac{4^4}{6} \frac{\left(\int_0^\infty D_{\text{eq}}^3 \frac{dN(D_{\text{eq}})}{dD_{\text{eq}}} dD_{\text{eq}} \right)^5}{\left(\int_0^\infty D_{\text{eq}}^4 \frac{dN(D_{\text{eq}})}{dD_{\text{eq}}} dD_{\text{eq}} \right)} \quad (2)$$

Given values of D_m and N_0^* , the corresponding bulk ice-mass density, the ice water content (IWC), can be inferred using

$$\text{IWC} = \frac{\pi\rho}{4^4} N_0^* D_m^4. \quad (3)$$

180 The normalized shape of the PSD, the so-called unified size distribution shape, is assumed to be of the form

$$F_{a,b}(x) = b \frac{\Gamma(4)}{4^4} \frac{\Gamma(\frac{a+5}{b})^{4+a}}{\Gamma(\frac{a+4}{b})^{5+a}} x^a \exp\left(-\left(x^b \frac{\Gamma(\frac{a+5}{b})}{\Gamma(\frac{a+4}{b})}\right)^b\right) \quad (4)$$

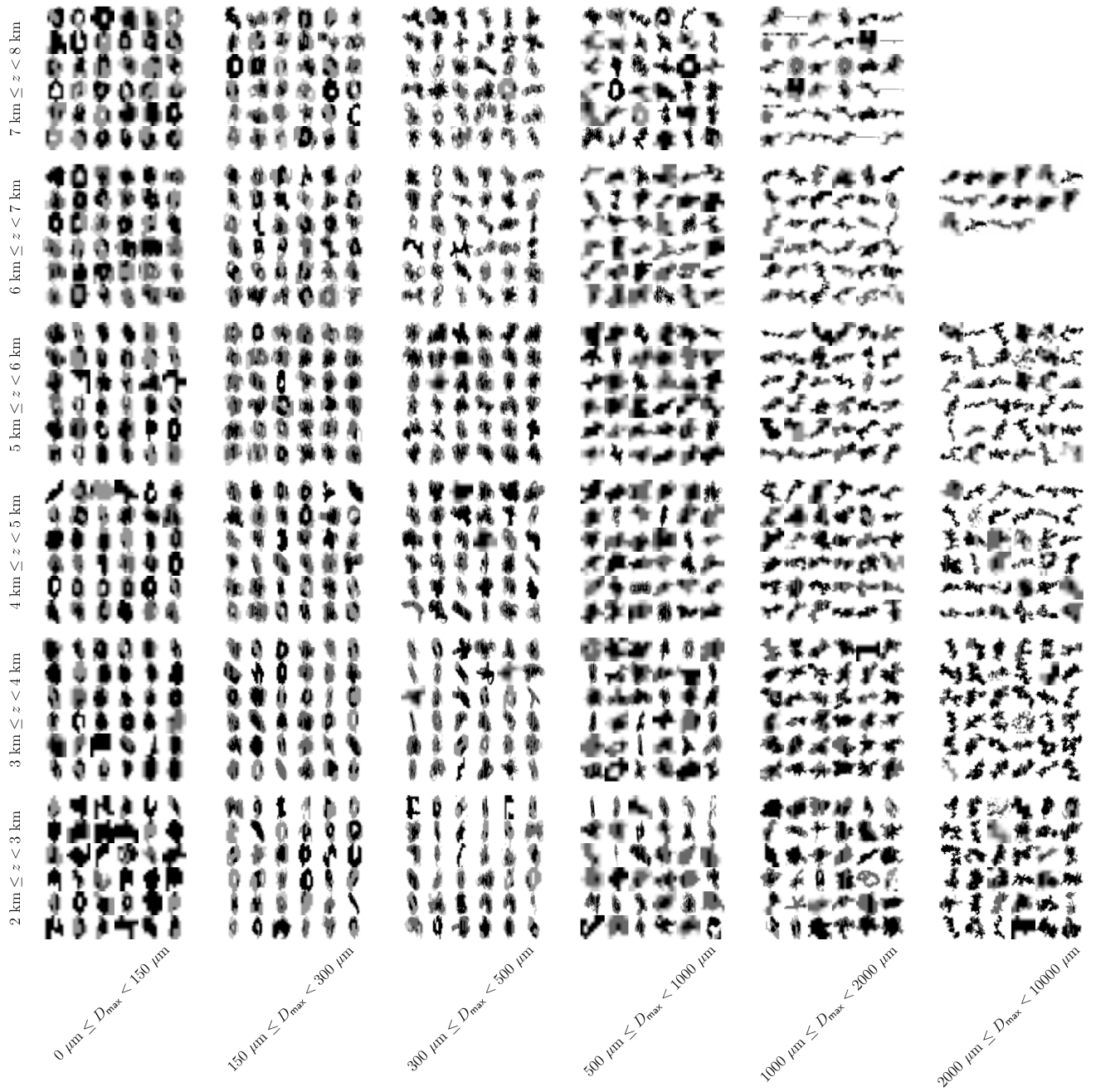


Figure 7. Ice particle shape images recorded by the CIP probes. Each image patch displays 70 particle images for a given altitude and particle diameter range. Rows contain particle images from 1–km intervals ranging from 8 km (first row) down to 2 km (last row). Columns contain particle sizes with the interval boundaries given below the lowermost image patch.

with shape parameters a, b . The shape parameters are assumed fixed a priori and determined from fits to in-situ data. Note that the shape parameters a, b have been renamed compared to the definition in Delanoë et al. (2014) to avoid confusion with the parameters of the mass-size relation.

185 **2.4.2 Mathematical formulation**

The applied retrieval algorithm makes use of the optimal estimation framework (Rodgers, 2000). Given an observation vector $\mathbf{y} \in \mathbb{R}^m$, the retrieved state $\mathbf{x} \in \mathbb{R}^n$ is defined as the one that maximizes the Bayesian a posteriori probability of \mathbf{x} under the assumptions of Gaussian measurement errors and a priori uncertainties. Practically, \mathbf{x} is found by minimizing a cost function of the form

190
$$\mathcal{L}(\mathbf{x}, \mathbf{y}) \propto (\mathbf{F}(\mathbf{x}) - \mathbf{y})^T \mathbf{S}_e^{-1} (\mathbf{F}(\mathbf{x}) - \mathbf{y}) + (\mathbf{x} - \mathbf{x}_a)^T \mathbf{S}_a^{-1} (\mathbf{x} - \mathbf{x}_a), \quad (5)$$

which corresponds to the negative log-likelihood of the posterior distribution. Here, \mathbf{F} is a numerical model that maps a given retrieval state \mathbf{x} to a simulated observation $\mathbf{F}(\mathbf{x})$. The vector \mathbf{x}_a is the mean of the a priori distribution. The matrices \mathbf{S}_e and \mathbf{S}_a are the covariance matrices that describe the Gaussian distributions of measurement error and a priori uncertainties, respectively. The choice of the values for \mathbf{x}_a and \mathbf{S}_a is described in Pfreundschuh et al. (2019).

195 **2.4.3 Adaptation to joint flight observation**

The main modifications applied to the original implementation affect the observation vector \mathbf{y} , which for this study consists of the observations from the HAMP radar, the passive radiances measured by ISMAR and the passive channels of HAMP. All observation errors are assumed to be independent. The assumed uncertainties as well as the preprocessing applied to the observations are described in Sec. 2.2.

200 Furthermore, the resolution and extent of the retrieval grids were adapted to the viewing geometries of the cloud overpass. The D_m parameter of the PSD of frozen hydrometeors is retrieved at a resolution of 200 m between the melting layer and an altitude of 12 km. The N_0^* parameter is retrieved at a reduced resolution of about 1 km.

2.5 Radiative transfer modeling

Version 3.2.1277 of the Atmospheric Radiative Transfer Simulator (ARTS, Buehler et al. (2018)) is used both a the retrieval
205 forward model as well as the forward simulations for the RASTA radar.

2.5.1 Retrieval forward model

RADAR reflectivities are simulated using ARTS' single-scattering radar solver. For the simulation of passive radiances, a hybrid solver is used which combines the RT4 (Evans and Stephens, 1995) scattering solver with the ARTS standard scheme for pencil beam radiative transfer. Surface emissivity over the ocean surface is simulated using the Tool to Estimate Sea-
210 Surface Emissivity from Microwaves to sub-Millimeter waves (TESSEM, Prigent et al. (2017)). Absorption from N_2 and O_2

are modeled using the absorption model by Rosenkranz (1998). For H_2O , absorption lines are taken from the AER line catalog (Oyafuso et al., 2017) combined with the MT-CKD3.2 (Mlawer et al., 2012) continuum. Scattering data for ice particles and liquid particles is taken from the ARTS single scattering database (ARTS SSDB, Eriksson et al. (2018)).

3 Cloud microphysical properties

215 As shown in Pfreundschuh et al. (2019), the developed synergistic retrieval shows considerable sensitivity to the assumed microphysical properties of the ice particles used in the retrieval. To assess the validity of these assumptions, it is desirable to compare them to the available in-situ measurements of the observed cloud. Unfortunately, most of these properties cannot be measured directly by the available instrumentation, but further analysis is required to infer them from the data. This section describes this derivation and summarizes the resulting properties.

220 **3.1 Mass size relation**

The mass size relation is an important property for the remote sensing of bulk properties of ice particles. The relation connects the maximum diameter D_{\max} of a particle to its mass m and thus describes how the optical properties of a particle (assumed to be mainly governed by particle size) relate to its mass. Two approaches are followed here to estimate the mass size relation from the available in-situ data. For the first approach, the mass size relation is assumed to follow a power law of the form

225
$$m = \alpha \cdot D_{\max}^{\beta}, \quad (6)$$

where α and β are viewed as local properties of cloud. For the second approach, the assumption of a specific parametric form of the mass-size relation is relaxed instead modeled as a continuous function of maximum particle diameter D_{\max} and flight time t .

3.1.1 Power-law model

230 To determine the parameters of the power-law mass-size relation given in Eq. (6), $\log_{10}(\alpha(t))$ and $\beta(t)$ are modeled as functions of the flight time describing the properties of the ice particles along the descent through the cloud. To determine $\log_{10}(\alpha(t))$ and $\beta(t)$, they are modeled as independent Gaussian processes. Each joint realization of these random processes corresponds to an estimated IWC quasi-profile along the flight path, which is given by the integral of the corresponding particle mass over the measured particle size distributions:

235
$$\text{IWC}(t) = \int_{D_{\max}} \alpha(t) \cdot D_{\max}^{\beta}(t) \cdot \frac{dN(D_{\max})}{dD_{\max}} dD_{\max}. \quad (7)$$

Since m and $\frac{dN}{dD_{\max}}$ are measured, the above formulation allows to perform Bayesian inference for the functions $\alpha(t)$ and $\beta(t)$. This requires specifying an uncertainty for the predicted IWC with respect to the IWC measured by the Nevezorov probe. We somewhat arbitrarily assume an uncertainty of 5% for PSD and mass-density measurements averaged over 10-second intervals. This error budget accounts for errors in the measured m , the measured PSD as well as the representativeness of the model.

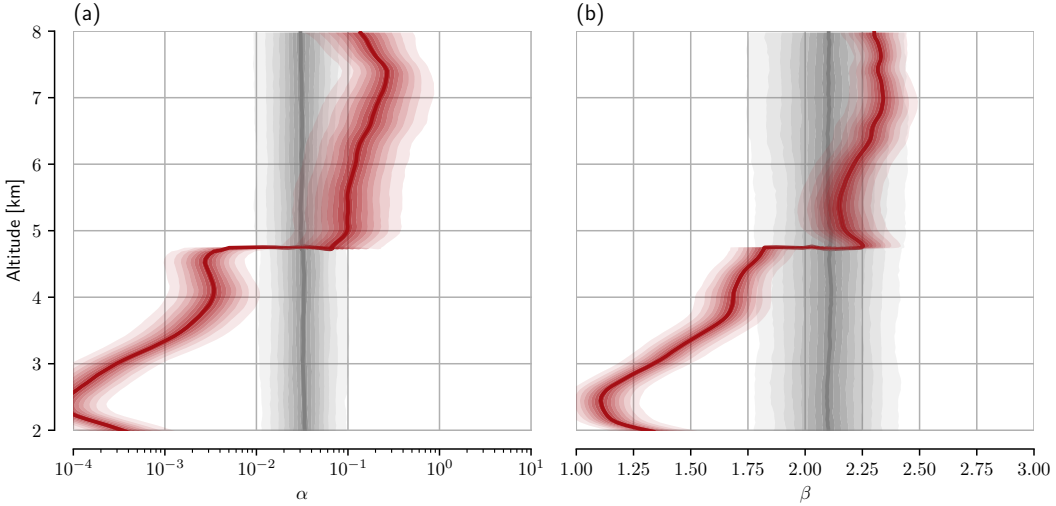


Figure 8. Prior (grey) and posterior (red) distributions for the Gaussian process models for the α and β parameters of the mass-size relation Eq. 6. Solid lines show the median of the distribution, while the shading marks the centered confidence intervals ranging from 10 to 90% confidence.

240 As priors for α and β constant mean functions with Matérn $\nu = \frac{5}{2}$ covariance functions (Williams, 2006) are assumed. The mean value for β was set to 2.1 and a corresponding value for α was determined by minimizing the mean squared error between corresponding IWC profile and the in-situ measured IWC.

With these assumption made, estimates for $\alpha(t)$ and $\beta(t)$ can be obtained by sampling their posterior distributions using Markov-chain Monte Carlo sampling. This has been done using the PyMC3 package for probabilistic programming (Salvatier 245 et al., 2016). The results of the inference for the α and β parameters are shown in Figure 8. The figure displays the assumed a priori distributions as well as the inferred a posteriori distributions for α and β as functions of the altitude. Above an altitude of 5 km, the values of both α and β are fairly close to the prior. At 5 km a strong discontinuity is observed at which both α and β jump to significantly smaller values. Below that, both parameters show a continued decrease with altitude.

3.1.2 Parameter-free model

250 The analysis presented above specified a parametric form for the mass-size relation of the particles. To investigate the effect of this assumption on the inferred mass-size relation, also a parameter-free model has been fitted to the measured PSD and IWC data. Instead of two independent Gaussian processes for α and β , a two-dimensional Gaussian process representing the logarithm of the particle mass as a function of flight time and particle maximum diameter D_{\max} is assumed. The prior mean 255 is chosen to be equivalent to what has been assumed for the the parametrized model. Also the covariance function in the time dimension is chosen similar to that used for the fitting of the power-law model. Along the size dimension a correlation length of 0.5 is assumed for $\log(D_{\max})$.

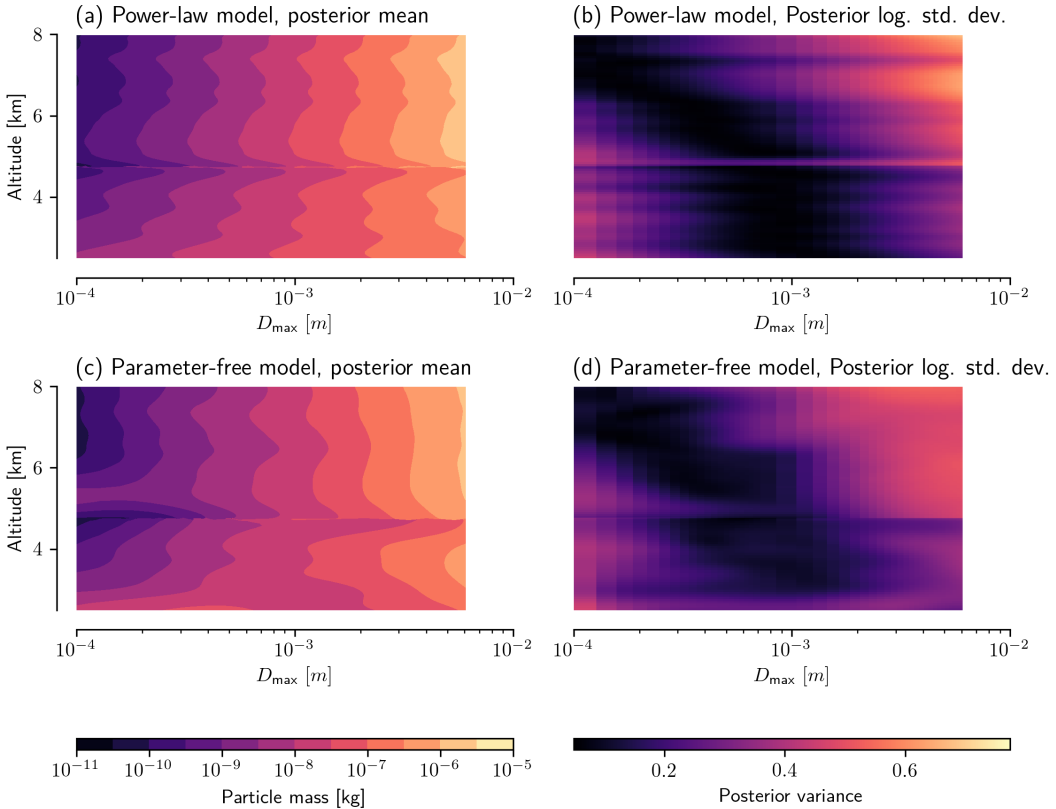


Figure 9. Posterior distributions of the inferred mass-size relationships. Panel (a) and (c) display the posterior mean of the inferred mass-size relation for the power-law and parameter-free model. Panel (b) and (d) display the corresponding standard deviations.

The inferred mass size relationships are displayed in Figure 9. For reference also the corresponding results obtained with the power-law model are shown in the upper panels of the figure. The parameter-free model yields comparable results to the power-law model above 5 km. Although the increased width of the filled contours around $D_{\max} = 300 \mu\text{m}$ indicates a slight deviation from the log-linear form of Eq. (6), the results remain close to those obtained with the parametrized model. Displayed in terms of the resulting masses, the discontinuity observed in the fitted α and β profiles for the power-law fit is clearly less dramatic. The same holds for the parameter-free model. Although a discontinuity is visible at an altitude around 5 km, the masses directly above or below the line remain fairly similar. Below this altitude, the irregular horizontal width of the contours clearly indicate deviations from a log-linear mass-size relationship.

Shown in panel (b) and (d) are the standard deviations of the log-masses as predicted by both models. Both of them exhibit the same general behavior: The regions of low posterior uncertainty shift from very small particle sizes at the top of the cloud to larger sizes at the bottom. This reflects the circumstance that the in-situ measurements at each altitude provide information only on particle size ranges that are observed and contribute significantly to the measured IWC.

A more detailed view of the retrieved mass-size relations at specific altitudes is provided in Fig. 10, which displays the
270 inferred relations for six altitude ranges in the cloud. The results confirm the observation that above 5 km the parameter-free model agrees fairly well with the power-law model. The differences that are observed for larger particle sizes are due to the flexibility of the parameter-free model, which returns to the a priori for sizes at which the in-situ measurements provide no information on the mass-size relationship.

At altitudes between 4 and 5 km as well as 4 and 3, the parameter-free model shows consistent deviations from a log-linear shape. Compared to the power-law model, the parameter free model generally exhibits a steeper slope for small particle sizes, which then flattens between 500 μm and 1000 μm . Overall, however, the results remain mostly consistent with those obtained with the power-law model, which is sufficiently close to be a linear approximation of the log-masses predicted by the parameter-free model.
275

For the lowest altitude range between 2 and 3 km, both models predict masses that exceed that of ice spheres. A possible explanation for these unphysical results are the very large particle sizes that were observed at these altitudes. As could be seen already in Panel (f) of Fig. 6, it is possible that particles with sizes exceeding the maximum measured diameter of the CIP probes were present at these altitudes. Large particles missing in the observed PSDs would force the fitted models to predict increased masses for observed particle sizes and thus potentially lead to overestimated particle masses.
280

3.1.3 Comparison to ice particle models

285 Another way to assess the validity of ice particle models is to use their assumed mass-size relationship to predict the in-situ measured IWC from the observed PSDs. A particle model that represents the actually observed particle well should yield IWC values comparable to those measured by the Nevezorov probe. The results of such an analysis are displayed in Fig. 11 for a range of different particle models from the ARTS SSDB as well as the fitted mass-size relationships.

Not very surprisingly, the fitted mass-size relationships, shown in Panel (a), exhibit only very small deviations from the
290 in-situ measured IWC. Of the particle models that correspond to pristine ice particles, shown in Panel (b), the PlateType1, ColumnType1 and 6-BulletRosette yield the best agreement with the in-situ data. The ice sphere particle model yields very large deviations from the in-situ data. The same holds for rimed particles, which have similarly high densities as ice spheres, and lead to a significant overestimation of the measured IWC. For aggregate particles, the LargePlateAggregate yields the best fit up to an altitude of 6 km above which the 8-ColumnAggregate yields the smallest errors.
295

Based on these results, it seems reasonable to exclude the models for rimed particles as well as the GemCloudIce model from the range of models to consider for the ice particles in the cloud. A direct comparison of the mass-size relationships of the remaining particle models and the ones inferred from the in-situ data is given in Fig. 12. For the three highest altitude ranges, most particle models fit the retrieved mass-size relationships well. Exceptions are the LargeColumnAggregate and the SectorSnowflake models. For the three lower altitude ranges, however, the retrieved mass-size relationships predict lower
300 masses for large particles than any of the available particle models.

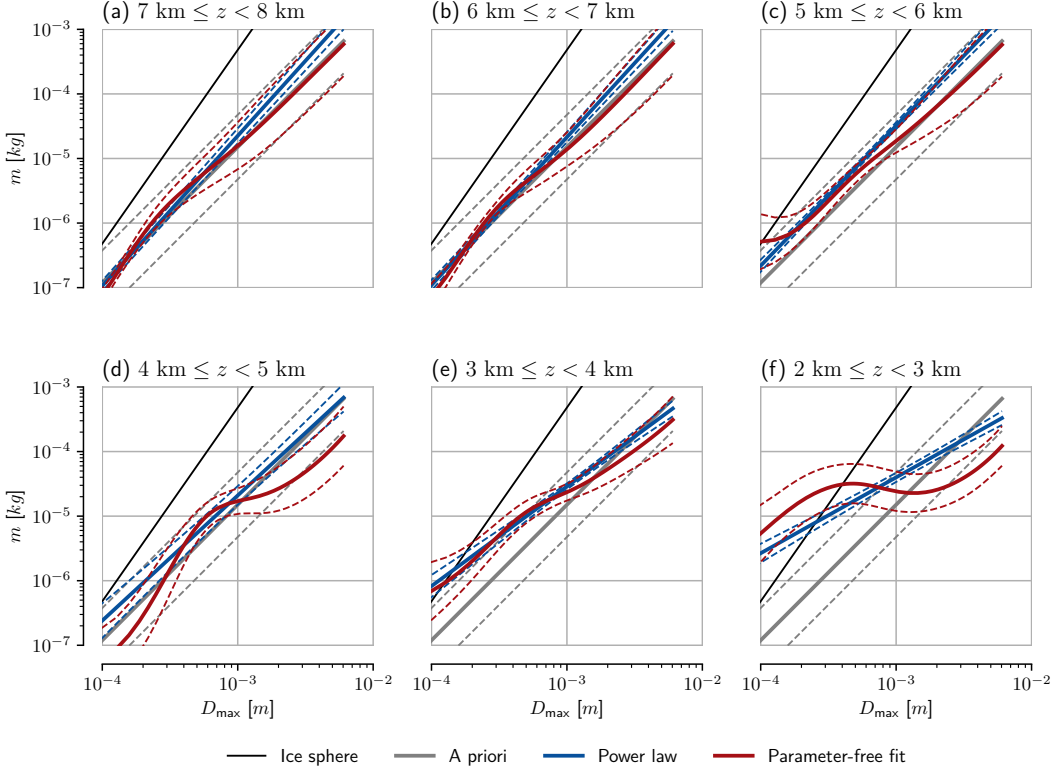


Figure 10. Fitted mass-size relationships for different altitudes within the cloud. In each panel, the a priori assumed relationship (grey), the fitted power-law model (blue) and the parameter-free model (red) are shown. Solid lines show the mean while dashed lines mark the extent of two standard deviations of the variability over the altitude interval and the posteriori uncertainty. The mass-size relationship corresponding to a solid ice sphere is shown by the solid black line.

3.2 PSD shape

In addition to the shape of the ice particles, the retrieval requires assumptions to be made on the shape of the PSD. Although in-situ measurements of PSDs are available from the CIP probes, it is not possible to directly infer the unified size distribution shape from them. This is because the CIP probes measure the PSD with respect to the approximate maximum particle diameter

305 D_{\max} whereas the unified shape is defined with respect to the volume-equivalent diameter D_{eq} . In order to derive the unified PSD shape from the in-situ data, it is thus necessary to assume a mass-size relationship to convert the observed D_{\max} to D_{eq} . Here, we use the power-law mass-size relationship derived above to compute the unified PSD shape. The resulting PSDs are displayed in Fig. 13 for different altitudes in the cloud.

Also shown in the figure are fits to the observed PSD shapes. Following Delanoë et al. (2014), two fits were derived for 310 each altitude interval by minimizing the difference in the visible extinction and radar reflectivities. The visible extinction corresponds to the second moment of the PSD and the resulting fit will therefore be more dominated by the behavior at smaller

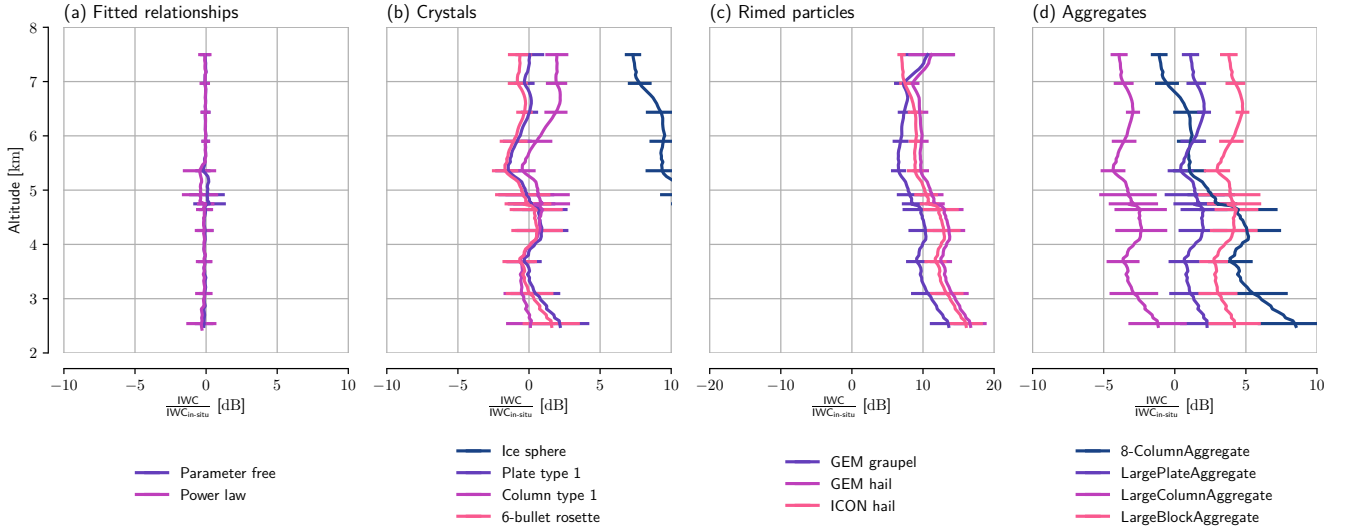


Figure 11. Deviations of the IWC profiles derived from the observed PSDs using the mass-size relationship of the model from the observed IWC. Panel (a) shows the deviations for the mass-size relationships fitted to the in-situ data. Panel (b), (c) and (d) show the deviations for different ice particle models classified into crystals, rimed particles and aggregates.

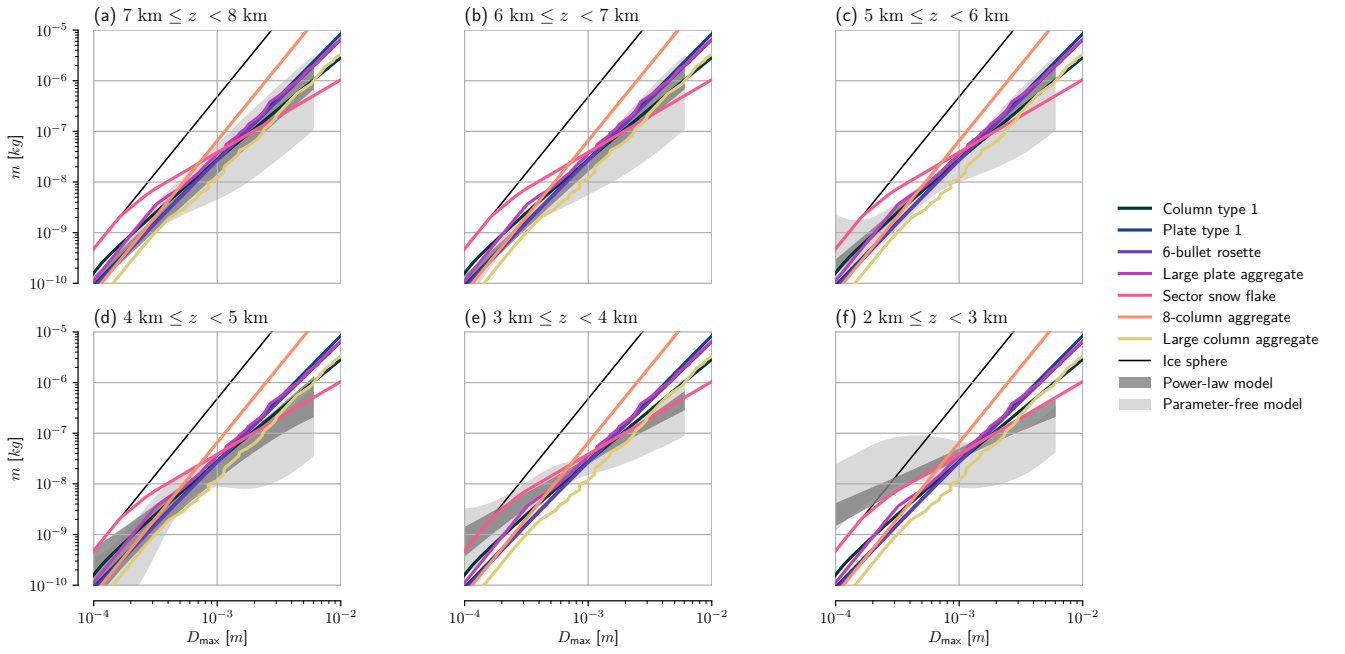


Figure 12. Mass-size relationships of the different particle models compared to the inferred mass-size relationship at different altitude in the cloud. The colored markers show the mass-size relationships for different particle models. The black line shows the mean of the fits obtained with the power-law model, while the shading displays the mass ranges predicted by the parameter-free model.

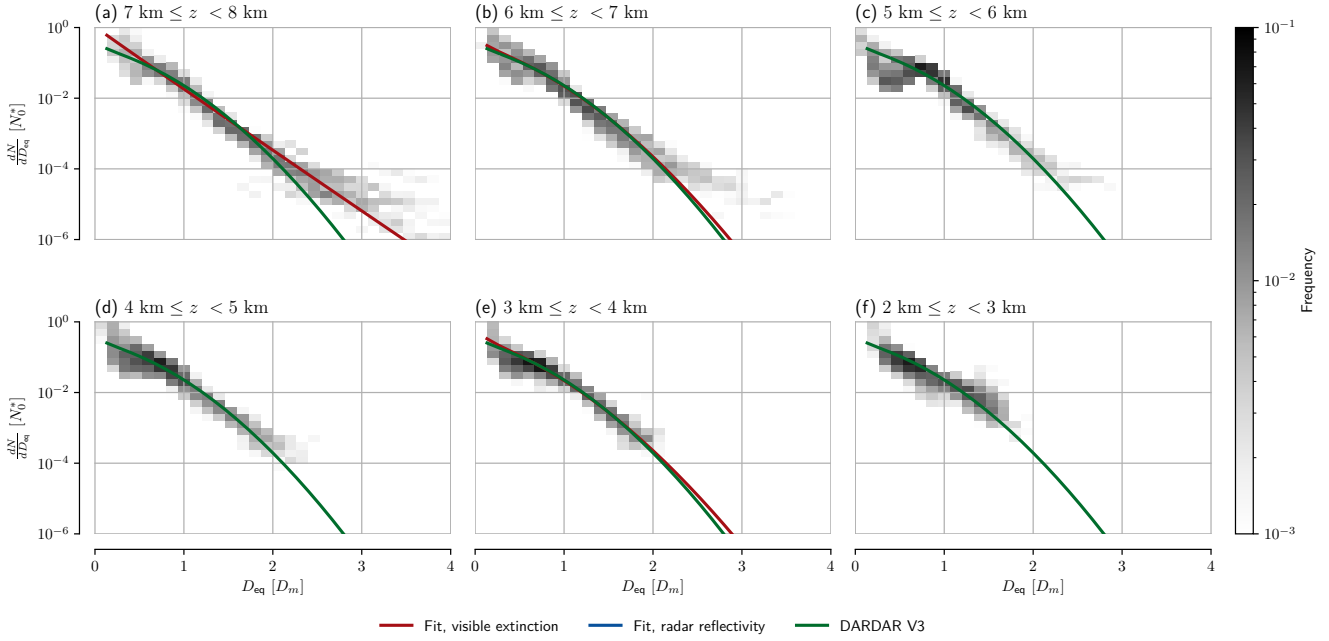


Figure 13. Observed and fitted unified particle distribution shapes. Each panel shows the unified PSDs for each altitude interval together with the fits obtained by minimizing the difference in extinction and radar reflectivity as well as the shape used in the DARDAR cloud product.

particle sizes. Contrarily, by fitting the radar reflectivity, which corresponds to the sixth moment of the PSD, more emphasis is put on the behavior for large particles. Also shown in each panel is the unified shape used by version 3 of the DARDAR cloud product (Cazenave et al., 2018), which is the shape that is in the synergistic retrieval algorithm.

315 The DARDAR shape generally provides a very good fit over all altitudes. For the two highest altitude ranges, the obtained fits tend more towards monodisperse distributions. Below that, the shape gradually levels off at low D_m values. The results at the lowest altitude interval are likely not very reliable due to the potentially missing large particles, which already caused unphysical results for the inferred mass-size relationships.

320 Although the DARDAR shape gives a very good fit to the observed unified particle distribution shape derived from the in-situ measurements, the quality of this fit still depends on the assumed mass-size relationship. This means that for particles with a drastically different mass-size relationship a different shape may provide a better fit. To investigate this effect, shape parameters for the particle models applied in the retrieval were derived using their specific mass-size relationships. For each shape, two fits were derived for all of the altitude intervals using both visible extinction and radar reflectivity as similarity measures. From these, the fit to the visible extinction obtained for the height interval between 3 and 4 km is used in the retrieval to test its 325 sensitivity to the assumed PSD shape. The choice of the fit was based on the observation at this altitude interval and for the fit using the visible extinction the largest deviations from the DARDAR shape were obtained. The derived a and b parameters are

included together with a plot of the observed and fitted unified particle distribution shapes for the 8-column aggregate particle model in Appendix A.

4 Retrieval results

330 In this section, the results of the synergistic hydrometeor retrieval applied to the active and passive microwave observations obtained during the cloud overpass are presented. The results obtained with the LargePlateAggregate particle model and the DARDAR PSD shape are presented first to serve as a baseline. This configuration is used here since it was found to work well on the synthetic cloud scenes considered in Pfreundschuh et al. (2019). These results are then compared to the in-situ measurements and the results obtained with other particle models and PSD shapes. Finally, the closure of the different retrieved
335 atmospheric states with respect to the radar observations from the RASTA radar is considered.

4.1 Fit to observations

We start by examining the fits to the observations obtained with the baseline configuration. Accurate forward modeling of remote sensing observations is itself a challenging task and even more so if observations from multiple sensors are involved. The quality of the fits of the retrieval to the observations thus constitutes an important consistency check regarding the reliability
340 of the retrieval results.

4.1.1 Hamp radar

The fitted radar observations of the combined retrieval are displayed together with the fits obtained with a radar-only version of the retrieval algorithm in Fig. 14. The radar-only retrieval fits the observations well over the whole scene, except for some deviations in range bins close to the boundaries of the cloud. Contrary to this, significant deviations from the observations
345 appear in the results from the combined retrieval. They are concentrated in two regions located at around 150 km and 330 km where the observed radar reflectivities are strongly underestimated. Both of them are regions of comparably high radar reflectivity, indicating the presence of large ice particles or potentially even water in the liquid phase. Since the misfit is not present in the results of the radar-only retrieval, this indicates an inconsistency between the active and passive observations which the retrieval is not able to resolve.

350 4.1.2 HAMP passive channels

The residuals of the fits to the radiances observed by the passive HAMP channels are displayed in Figure 15. The bands around 25 and 53 GHz exhibit very low deviations from the observations over the whole scene. For the 90-GHz band, however, the retrieval does not achieve an equally good fit to the observations. Instead a warm-bias of the retrieval of a few Kelvin is observed. Since this bias is particularly apparent in the left part of the scene where there are only very few clouds, a potential
355 explanation for it are errors in the emissivity model used for the sea surface.

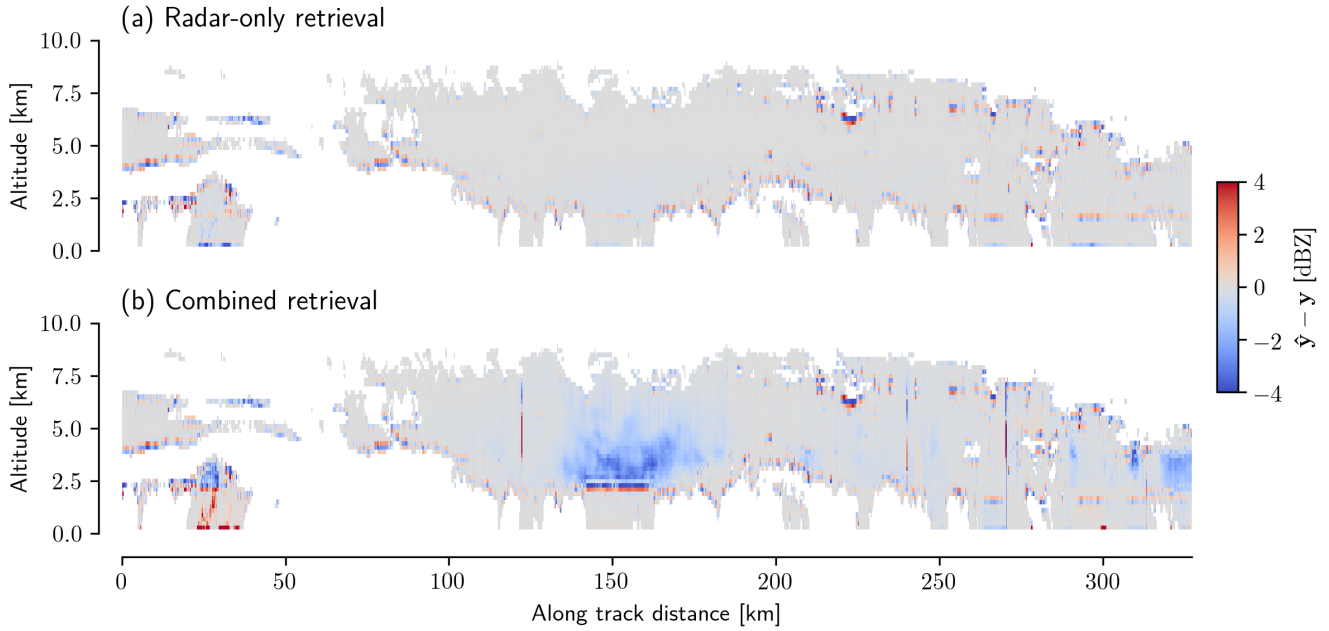


Figure 14. Fitted radar reflectivities. Panel (a) displays the radar reflectivities y as observed by the HAMP radar. Panel (b) displays the fitted reflectivities \hat{y} obtained with the LargePlateAggregate particle model. Panel (c) shows the difference between fitted and observed radar reflectivities.

A small but consistent bias towards warm brightness temperatures is observed for the channels closest to the line center of the 118-GHz band. For the two other channels, this bias is even larger.

For the band around 183 GHz, the residuals of almost all channels are small and appear random. The exception are the channels at 0.6 GHz and 3.5 GHz from the line center which exhibit visible warm respectively cold biases.

360 4.1.3 ISMAR

The residuals for the radiances observed by ISMAR are displayed in Fig. 16. For the channels around 118 GHz, the behavior is the opposite of that observed for the corresponding HAMP channels: While the channels closest to the line center fit the observations well, a systematic cold bias is observed for the channels further out. The systematic biases observed in both bands could therefore point towards potential calibration discrepancies between the two sensors.

365 For the 243 GHz channel, a good fit is observed over almost the whole scene except for a region around 150 km for which the retrieval produces brightness temperatures that are too low. The two innermost channels around the 325 GHz line fit the observations well despite a comparably large random error. The outermost channel of this band, however, shows a cold bias around 150 km, which is even stronger than that of the 243 GHz channel. For the channel at 664 GHz a good fit is achieved over basically the whole scene.

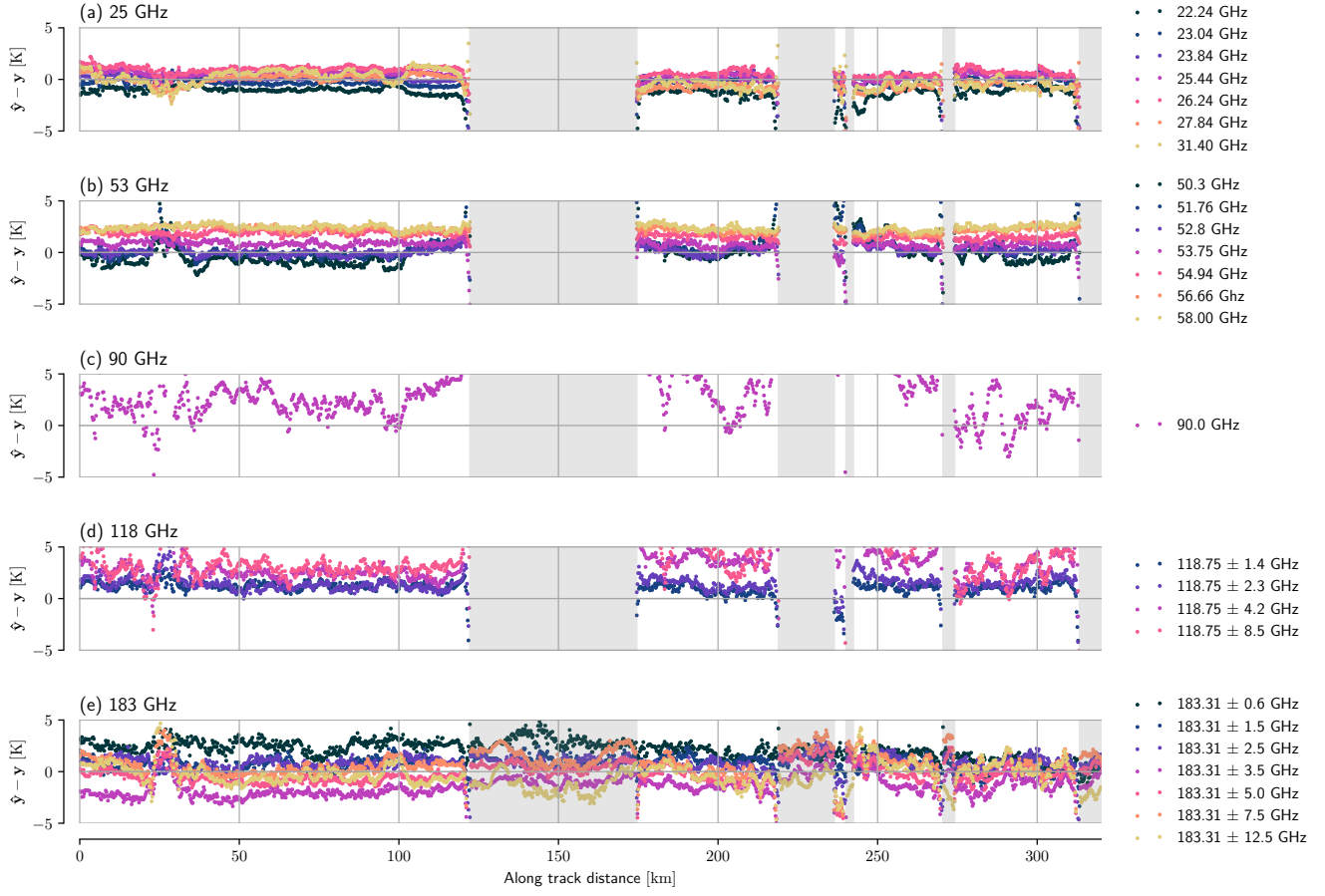


Figure 15. Fitted radiances for the passive HAMP channels. Each panel in the figure displays the residuals of the passive HAMP channels, defined as the difference between observed radiances y and fitted radiances \hat{y} .

370 It is notable that the cold biases in the 243 GHz and 325 GHz bands coincide in location with the cold biases observed in the fitted radar reflectivities. This points towards an inconsistency between the backscattering at 35 GHz and the cloud signal observed at 243 and 325 GHz.

4.2 Retrieved hydrometeors fields

The retrieved fields of the D_m and N_0^* parameters of the PSDs of frozen hydrometeors are displayed in Figure 17. Both fields
375 show a clear signal from the observed cloud. While D_m parameter exhibits fine structures comparable with those observed in the radar observations, the retrieved N_0^* -field varies more smoothly. One of the most distinct features of the retrieved N_0^* field is a region of very low N_0^* values located at 150 km. Since this is also the region where the active and passive observations do not agree this may be a compensation effect rather than a real signal. Apart from that, the cloud still exhibits considerable

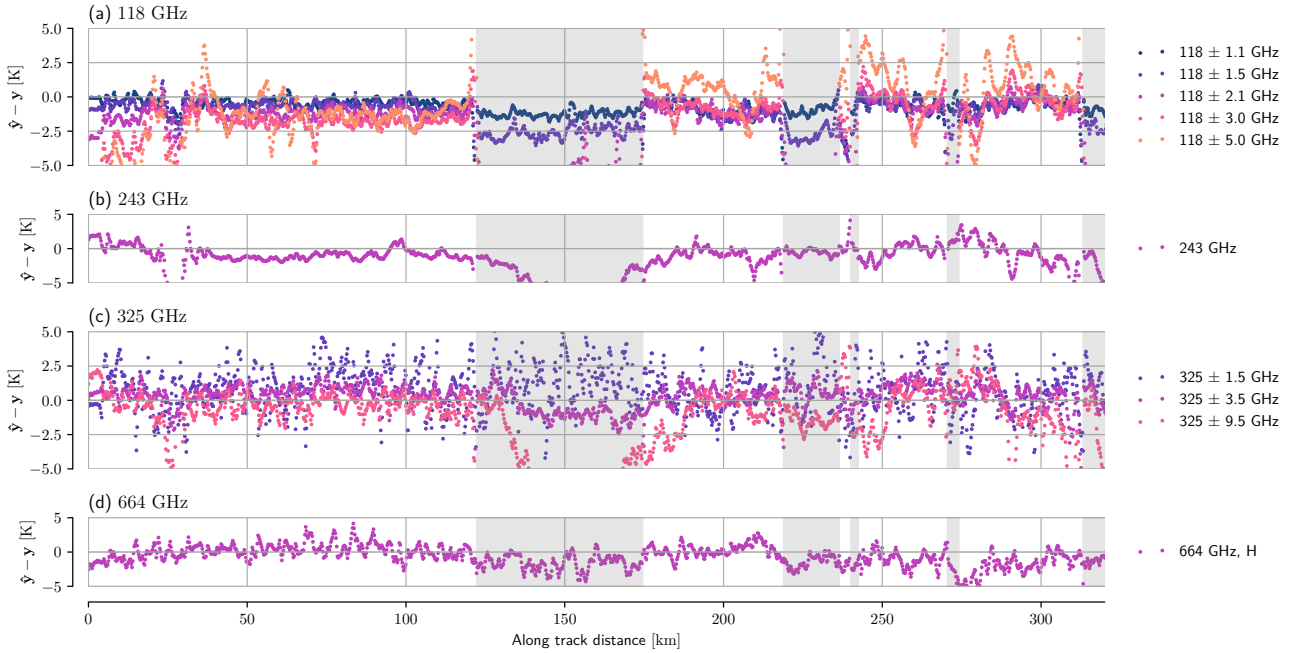


Figure 16. Fitted radiances for the channels of ISMAR. Each panel in the figure displays the residuals one of the bands of ISMAR, defined as the difference $\hat{y} - y$ between observed radiances y and fitted radiances \hat{y} .

variability in the N_0^* field which could potentially provide relevant information on the microphysical properties of the cloud.

380 Unfortunately, the areas where the retrieval predicts significant deviations from the background were not during the descent of the cloud so it is difficult to judge whether these results are trustworthy.

4.3 Comparison to in-situ data

A very interesting question which the data from the joint flight can help to answer is how well the synergistic retrieval agrees with in-situ measurements of ice hydrometeors. To compare the retrieved values to the in-situ-measured ones, the retrieval 385 results have been interpolated to the flight path of the FAAM aircraft. The resulting quasi-profiles of the D_m and N_0^* parameters as well as the corresponding IWC are displayed in Figure 18. The in-situ profiles for D_m and N_0^* were determined from the measured PSDs using the power-law mass-size relationship described in Sec. 3. In addition to the in-situ data, also the results from the radar-only version of the retrieval are shown, which serve as a baseline for the synergistic retrieval.

The D_m values retrieved using the combined retrieval are in good agreement with the in-situ data. The exception is the 390 8-column aggregate for which the largest deviations from the in-situ profile are observed. For most particles, the D_m values retrieved from the combined retrieval are in better agreement with the in-situ data than those from the radar-only retrieval. The exception is again the 8-column aggregate, for which the D_m value is strongly overestimated. It should be noted, however,

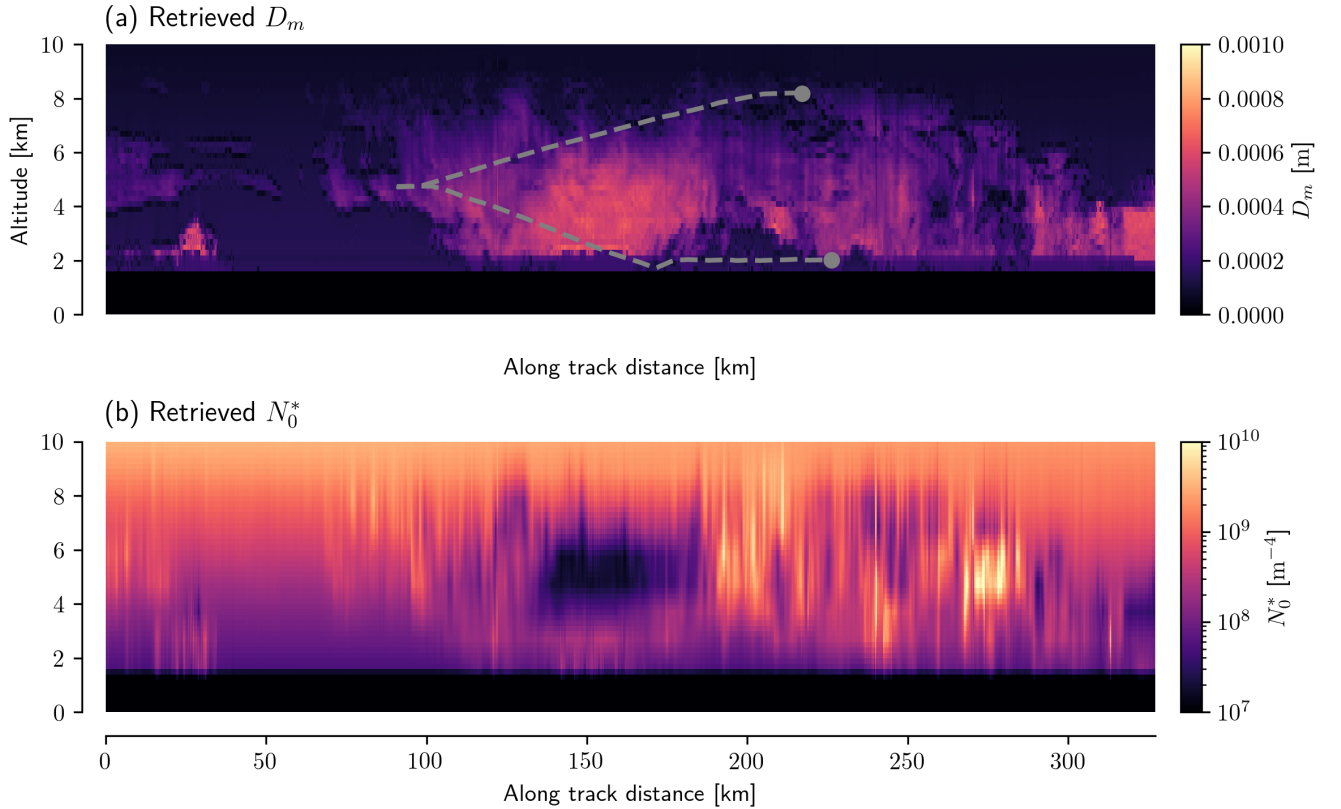


Figure 17. Retrieved scaling parameters D_m (Panel (a)) and N_0^* (Panel (b)) using the LargePlateAggregate particle model. The grey dashed line in Panel (a) shows the flight path of the FAAM aircraft during its descent through the cloud.

that the 8-column aggregate is shown here as an example for a very dense particle, for which high values of D_m correspond to significantly smaller particle sizes than for less dense particles.

395 For the N_0^* parameter, the situation is slightly different. Both the combined and the radar-only results are completely insensitive to the very high values encountered at the top of the cloud. The results from the combined retrieval deviate only slightly from those of the radar-only retrieval. Since N_0^* is not retrieved in the radar-only retrieval the result here is just the a priori N_0^* -profile used for both retrievals. The combined retrieval seems to yield slight improvements compared to the radar-only retrieval at least for altitudes between 3 and 6 km. Below that, however, the N_0^* can show exhibit quite drastic deviations from 400 the reference values as is the case for the large column aggregate and the 8-column aggregate particles.

Regarding the retrieved IWC, both the results from the combined and the radar-only retrievals agree fairly well with the in-situ data. The exception is the altitude range between 6.5 and 8 km, where both retrievals underestimate the mass by an order of magnitude.

The effect of the PSD shape on the retrieval results is generally small but in most cases helps to improve the retrieval.

405 This shows that the particle shape and the corresponding mass-size relationship remain one of the major sources of retrieval uncertainty.

4.4 Closure

Finally, we inspect the closure with respect to the observations from the RASTA radar. RASTA is a W-band cloud radar operating at 95 GHz. The radar reflectivities observed during the flight have been scaled down to a resolution of 200 m. These are 410 compared to simulated radar reflectivities obtained using the results from the combined and the radar-only retrieval. Figure 19 displays the true and the simulated radar-reflectivities for both retrieval types and the particles models discussed above. The simulated radar reflectivities are in general agreement with the observed radar reflectivities. Small biases are observed for the radar-only retrieval using the large plate aggregate and the 8-column aggregate particles, which are slightly reduced in the results of the combined retrieval. The combined retrieval, however, exhibits larger spread for radar reflectivities between 0 and 415 5 dBZ. Overall, the differences between the radar -only and the combined retrieval remain small.

5 Discussion

The principal aim of this study was the validation of the synergistic hydrometeor retrieval, particularly of the required modeling of cloudy-sky radiative transfer at sub-millimeter wavelengths. The validation is based on the following three assessments:

1. The fit of the forward model to the observations,
- 420 2. the comparison of the retrieval results to in-situ data taking into account the derived microphysical properties of the cloud,
3. and the closure with respect to the observations from the RASTA radar.

5.1 Fit to observations

Regarding the fit to the observations shown in Fig. 14, 15 and 16, it can be noted that a good fit is achieved over most parts of 425 the scene. Since the retrieval uses observations from 3 different sensors on two different airplanes this is not self-evident. The strongest systematic biases were observed in the HAMP channels around 90 GHz and 118 GHz, however even those are likely still within the error margins if absolute calibration and modeling errors are accounted for.

Nonetheless, significant deviations were observed in the fitted HAMP radar reflectivities and the ISMAR channels at 243 and 325 ± 9.5 GHz. Upon closer investigation, the misfit was found to depend on the applied particle model. This is illustrated 430 in Panel (a) of Fig. 20, which displays the column integrated misfit in the radar reflectivities against the misfits in the 325 GHz channel. Although the general dependency of the misfit on the particle model is expected, it is puzzling that the deviations are smallest for the particles that would be deemed the most unlikely based on the particle images (Fig. 7) and the fitted mass-size relationships (Fig. 11), namely the ice sphere and the 8-column aggregate. To arrive at a possible explanation for this behavior

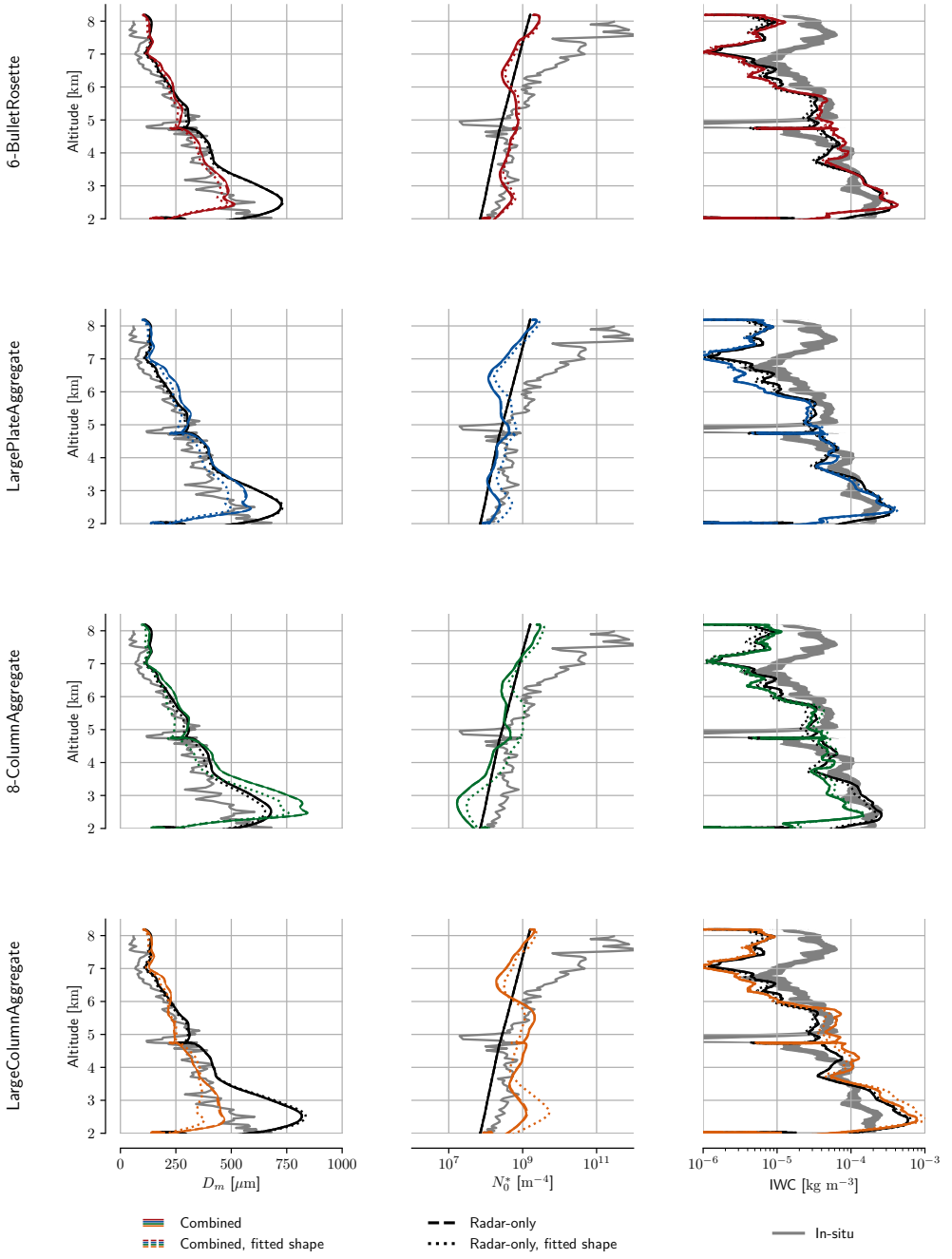


Figure 18. Comparison of retrieved profiles of D_m (first column), N_0^* (second column) and IWC (third column) for the synergistic retrieval with different ice particle models. Colored lines show the results from the combined retrieval, while the black lines show the corresponding results from the radar-only retrieval. The in-situ measurement are given by the solid grey lines.

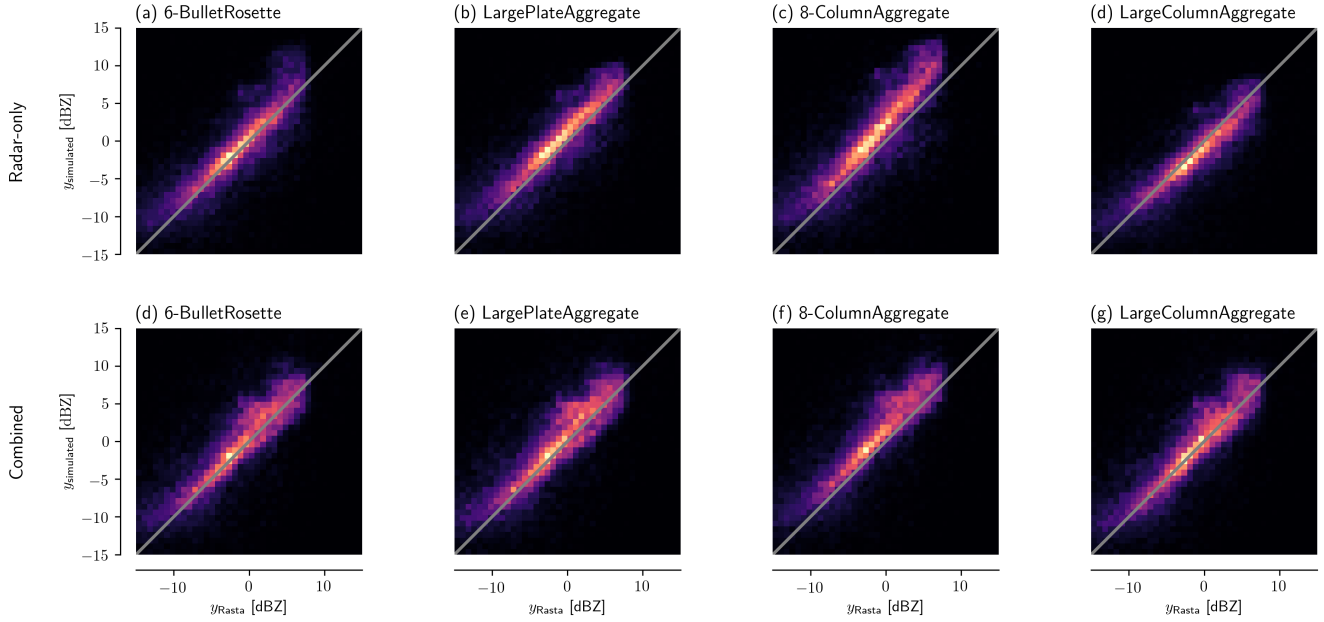


Figure 19. Scatter plots of observed versus simulated radar reflectivities from the RASTA radar. First row displays simulations obtained from the results of the radar-only retrieval. Second row displays simulations obtained from the combined retrieval.

the scattering properties of the different particles were analyzed leading to the results shown in Panel (b) of Fig. 20, which
435 displays the ratios of the scattering coefficients at the frequencies $325 \pm 9.5\text{GHz}$ and 35 GHz plotted against the maximum
particle diameter. Comparison with the retrieval misfits in Panel (a) reveals a similar grouping of the scattering properties as
observed for the magnitude of the misfits. These results seem to indicate that a better fit to the observations is obtained when
the ratio of the scattering coefficients decreases more rapidly with particle size. Also shown in the plot is the corresponding
440 curve for liquid droplets, which shows a significantly more rapid decline in the ratio of the scattering coefficients than any other
particle model. Based on this analysis, a possible explanation of the observed misfit would be the presence of mixed-phase or
liquid particles in this region of the cloud. This explanation would also match the appearance of the radar reflectivities in this
region that hint at convective activity and strong updrafts in this region (Houze Jr., 1981). Moreover, this hypothesis would also
be supported presence of liquid water detected by the Nevezorov (Fig. 5) probe.

This hypothesis has been briefly investigated by repeating the retrieval and allowing rain to exist above the $0 - {}^\circ\text{C}$ -isotherm.
445 Indeed this removed the misfits for all particles but affected the ice hydrometeor retrieval negatively. Furthermore, since this
did not lead to a significant improvement in the closure with respect to the RASTA radar reflectivities and because this is
certainly a very crude way of modeling the presence of liquid-phase particles, these results were not included here. Instead this
is left for future investigation.

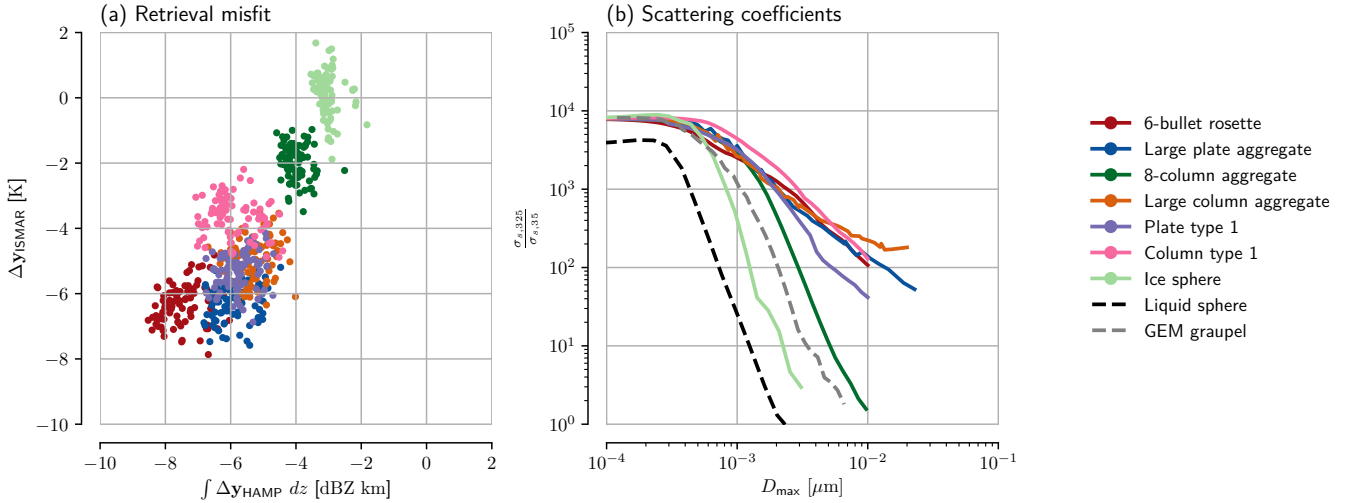


Figure 20. Panel (a) displays the column-integrated deviations of the fitted radar observations plotted against the misfit at the ISMAR 325 ± 9.5 GHz channel. Panel (b) displays the ratio of the scattering coefficients at 325 GHz and 35 GHz with respect to the maximum diameter D_{\max} .

Nonetheless, there are certainly also other possible explanations for the observed deviations. One of them would be multiple scattering, which is neglected in the radar simulations. Multiple scattering could explain the underestimation of the backscatter observed in the fitted radar reflectivities. Although it is generally thought to not be of relevance for airborne observations (Battaglia et al., 2010), it cannot be excluded here a priori.

5.2 Comparison to in-situ measurements

The most critical point for the validation is certainly the comparison to the in-situ measured IWC concentrations. In general, the retrieval results agreed quite well the IWC measured by the IWC probe in the lower parts of the cloud. Above altitudes of about 6.5 km the retrieval underestimates the IWC by almost an order of magnitude. In general, the combined retrieval did not yield significant benefits for the retrieved IWC profiles compared to the radar-only retrieval. Although this does not mean that the passive observations do not add information to the . Rather, improvements were observed in the retrieved profiles of D_m and N_0^* , for which in most cases the combined retrieval gave better results than the radar-only retrieval. This seems to indicate that the benefit of the combined retrieval is not necessary that it yields an improved IWC retrieval but rather that it improves the retrieval of additional moments of the PSD. Moreover, the a-priori assumed values for N_0^* are very close to those derived from the in-situ data, so there is not much information the passive information could add to the radar-only retrieval.

Similar to what has been found in Pfreundschuh et al. (2019), the retrieval results showed a clear dependence on the assumed particle shape. What is encouraging, however, is that the bad performance of specific particle models can be explained by their inconsistency with the in-situ observations. For example, the mass of the 8-column aggregate is well above the mass-size

relationships derived from in-situ data (Fig. 12) for sizes around 1 mm, which is the region that is constrained by the in-situ data at the relevant altitudes (c.f. Fig. 9). The same holds for the large column aggregate, which lies below the fitted mass-size relationships for most parts of this region.

As a synthesis of the results and in order to investigate the ice mass missed by the retrieval at the cloud top, the retrieval
470 results are presented once again in terms of retrieved IWC and number density in Fig. 21. Here, however, the IWC and number densities including only particles that are larger than $D_{\max} \geq 100 \mu\text{m}$ are given as reference profiles. These reference values have been obtained by applying the fitted power-law mass-size relationship. As the plot shows, when small ice particles are disregarded, the increase of IWC at high altitudes disappears and the retrievals yield better agreement with the in-situ data. Nonetheless, the retrievals still systematically underestimate the particle masses and number densities for altitudes above 6 km.
475 This behavior, however, is likely because most particles at these altitudes are too small to yield a significant back scattering signal in the radar observations and their concentrations too small to yield a signal in the sub-millimeter channels.

In summary, we find that the combined retrieval is in good agreement with the in-situ measurements of ice hydrometeors taking into account expected sensitivity ranges of the sensors. Although no large improvements are observed compared to the radar-only retrieval, these results show that the applied forward model is capable of consistently modeling the radiative transfer
480 for the radar sensor as well as the sub-millimeter channels. This provides an important validation for the findings presented in Pfreundschuh et al. (2019) on the potential synergies between radar and passive microwave observations. It further has to be considered here, that the region for which in-situ data was available was located above land which made that not all of the passive channels could be used in the retrieval. This could have further diminished potential synergies that could have been observed otherwise.

485 5.3 Closure

Regarding the closure with respect to the RASTA observations, fairly good agreement was obtained for most particles models as well as for both tested retrieval methods. The combined retrieval showed some signs of being able to correct or at least reduce biases observed in the results from the radar-only retrieval (Fig. 19, Panels (b), (c), (d)). Although this effect is rather small, it could indicate that the improvements in the retrieval results of the combined retrieval compared to the radar-only version
490 are more consistent with respect to the RASTA observations than with respect to the retrieved hydrometeor parameters. This would confirm that the inferior retrieval results obtained for example for the 8-column aggregate are due to the unsuitability of the particle model rather than the retrieval implementation.

6 Conclusions

From the results and discussion presented above we can conclude that the synergistic retrieval algorithm presented in Pfre-
495 undschuh et al. (2019) can provide accurate retrievals of distribution of frozen hydrometeors given suitable assumptions on the employed particle model. The results indicate a sensitivity of the combined retrieval down to mass concentrations around $10^{-5} \text{ kg m}^{-3}$ and particle diameters around $100 \mu\text{m}$.

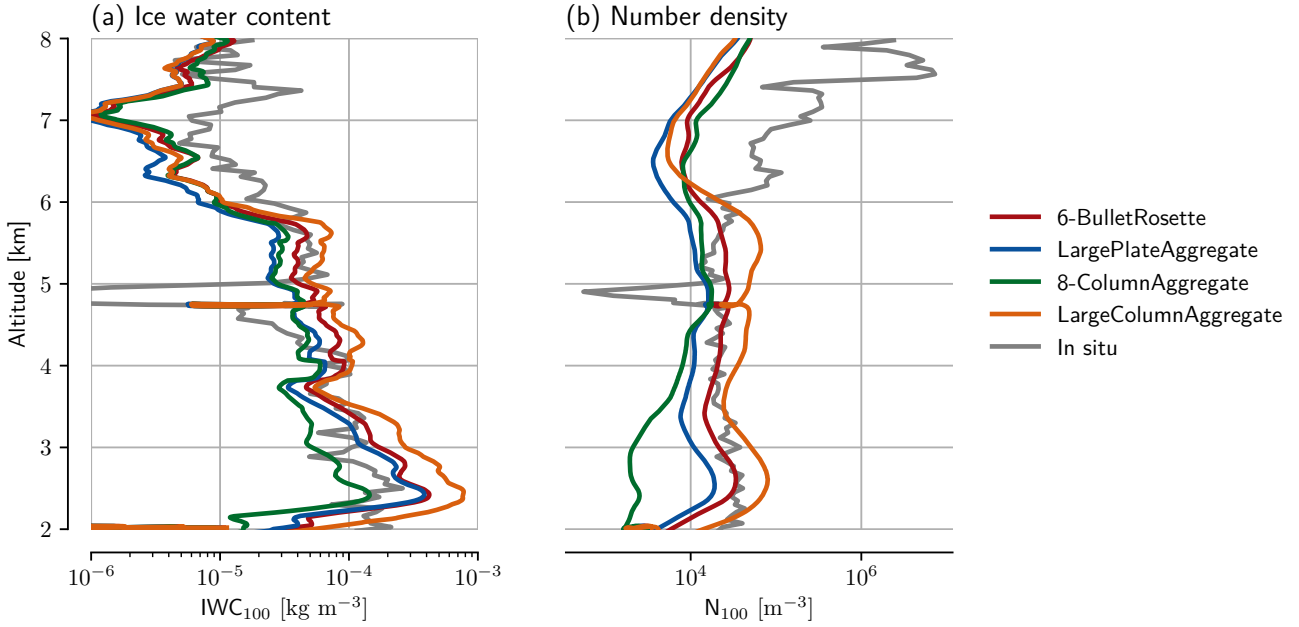


Figure 21. Synthesis of the retrieval results from Fig. 18 in terms of IWC (Panel (a)) and number density (Panel (b)). Reference profiles are calculated including only particles larger than $D_{\max} \geq 100 \mu\text{m}$.

Moreover, we conclude that the radiative transfer across the millimeter and sub-millimeter is sufficiently well understood that good fits could be obtained by the variational retrieval over the large parts of a complex cloud scene. The exception were
500 two regions that showed indications of convective activity where no consistent fit was obtained. It is suspected that this could be caused by the presence of liquid water above the melting layer but further work will be required to fully understand the cause of the misfits. Anyhow, this clearly shows the potential of combined observations involving radars and microwave radiometers, in particular at high microwave frequencies, for the remote sensing of the microphysical properties of clouds.

This study thus not only validates the findings regarding the synergies between active and passive microwave observations
505 Pfreundschuh et al. (2019) but also demonstrates the usefulness of the approach for the testing of radiative transfer models. The identified regions of convective activity will be useful studies cases for the development of ice particle models and potentially even cloud physics.

Code availability. All code used to produce the results in this study is available through public repositories (Simon Pfreundschuh, 2019).

Data availability.

510 **Appendix A: Fitted PSD shapes**

Table A1 displays the PSD shape parameter obtained by fitting the parametrized shape given in Eq. (4) to the normalized, in-situ measured PSDs. Since the normalization requires a mass-size distribution to be assumed, different fits are obtained for the PSD shape depending on the chosen particle model. The unified size distribution shape and the corresponding fits for the 8-column aggregate are given in Fig. A1 as an example of how the obtained fits can deviate from the results obtained in Fig. 13.

Table A1. Fitted parameters a and b of the unified size distribution shape (4) obtained by fitting the visible extinction of the unified size distribution shape over altitudes between 3 and 4 km.

Particle name	a	b
Plate type 1	0.036	1.11
Column type 1	0.094	1.43
6-bullet rosette	0.051	1.17
Large plate aggregate	0.07	1.26
Large column aggregate	0.04	1.15
8-column aggregate	-0.01	0.95
Ice sphere	0.03	1.1
Large block aggregate	0.08	1.34
Sector snow flake	0.26	2.32

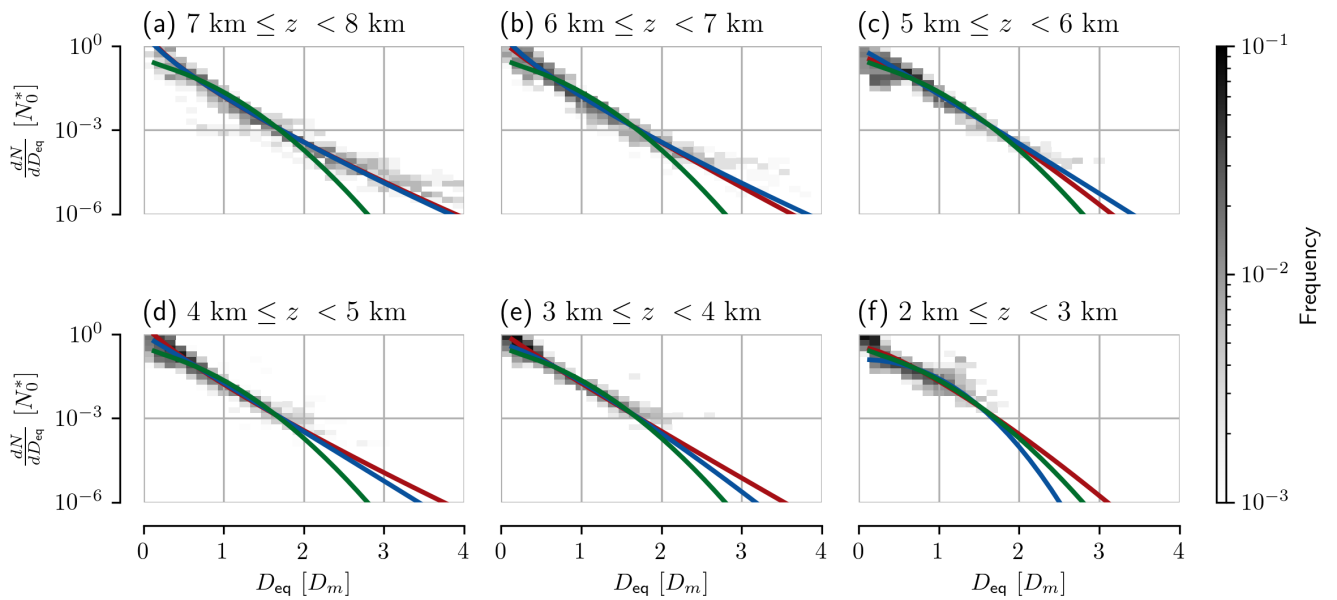


Figure A1. Observed and fitted unified size distribution shapes assuming the mass-size relationship of the 8-column aggregate.

515 Appendix B: Retrieval results for remaining particle models

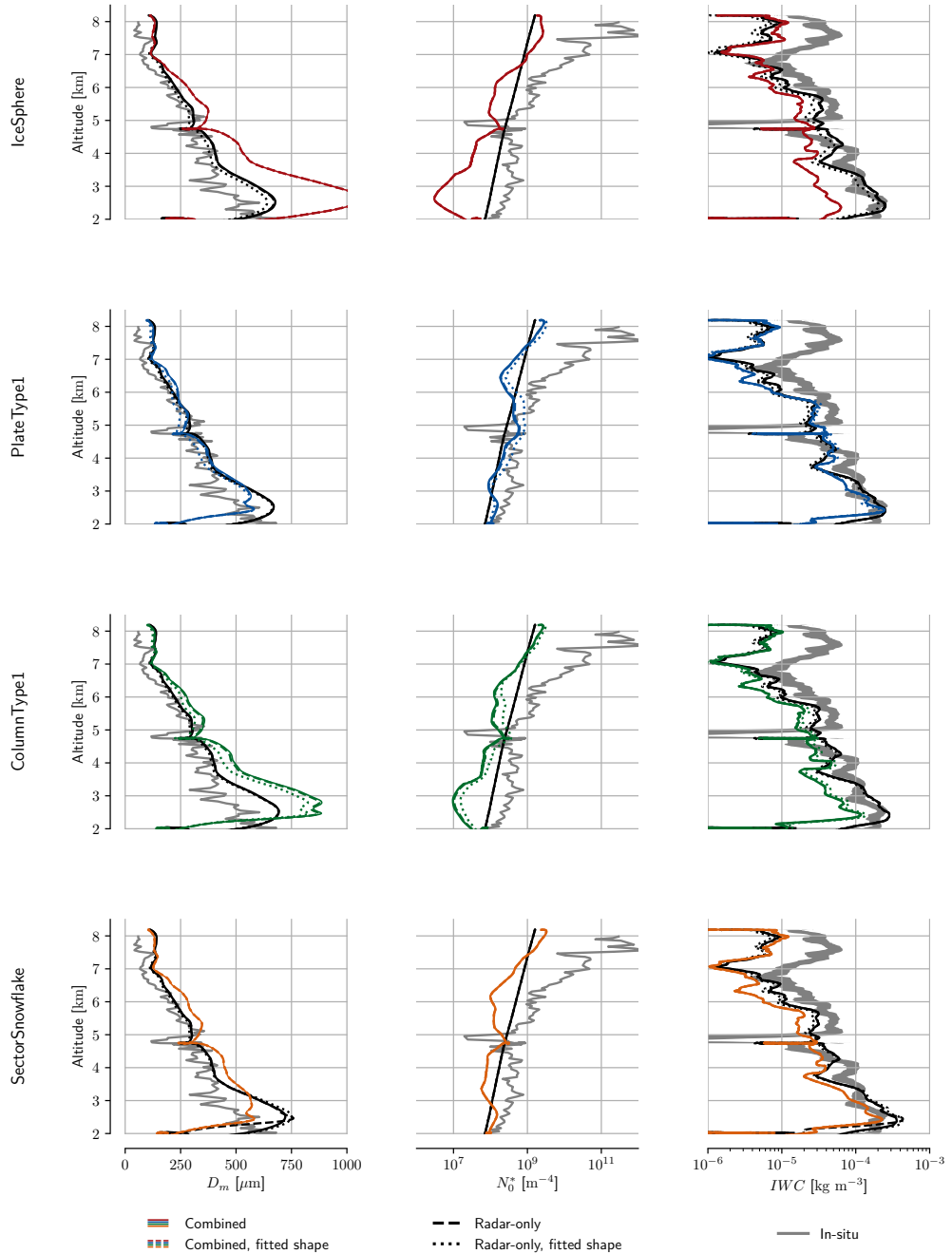


Figure B1. Same as Fig. 18 but for the remaining ice particle models.

Author contributions. Simon Pfreundschuh has performed the retrieval calculations and data analysis as well as written the manuscript. Patrick Eriksson, Stefan A. Buehler, Patrick Eriksson, Manfred Brath, David Duncan and Simon Pfreundschuh have collaborated on the study that lead to the development of the presented algorithm. Stuart Fox, Florian Ewald and Julien Delanoë have provided the flight campaign data, guidance regarding their usage and contributed to the interpretation and discussion of the retrieval results.

520 *Competing interests.* No competing interests are present

Acknowledgements. The combined and radar-only was developed as part of the ESA-funded study “Scientific Concept Study for Wide-Swath High-Resolution Cloud Profiling” (Contract number: 4000119850/17/NL/LvH). The authors would like to thank study manager Tobias Wehr for his valuable input and guidance during the study.

525 The work of SP, PE and RE on this study was financially supported by the Swedish National Space Agency (SNSA) under grants 150/14 and 166/18.

SB was supported by the Deutsche Forschungsgemeinschaft (DFG, German Research Foundation) under Germany’s Excellence Strategy — EXC 2037 ‘Climate, Climatic Change, and Society’ — Project Number: 390683824, contributing to the Center for Earth System Research and Sustainability (CEN) of Universität Hamburg.

530 The computations for this study were performed using several freely available programming languages and software packages, most prominently the Python language (The Python Language Foundation, 2018), the IPython computing environment (Perez and Granger, 2007), the numpy package for numerical computing (van der Walt et al., 2011) and matplotlib for generating figures (Hunter, 2007).

The computations were performed on resources at Chalmers Centre for Computational Science and Engineering (C3SE) provided by the Swedish National Infrastructure for Computing (SNIC).

References

- 535 Abel, S. J., Cotton, R. J., Barrett, P. A., and Vance, A. K.: A comparison of ice water content measurement techniques on the FAAM BAe-146 aircraft, *Atmos. Meas. Tech.*, 7, 3007–3022, <https://doi.org/10.5194/amt-7-3007-2014>, <https://www.atmos-meas-tech.net/7/3007/2014/>, 2014.
- Battaglia, A., Tanelli, S., Kobayashi, S., Zrnic, D., Hogan, R. J., and Simmer, C.: Multiple-scattering in radar systems: A review, *Journal of Quantitative Spectroscopy and Radiative Transfer*, 111, 917–947, 2010.
- 540 Buehler, S., Defer, E., Evans, F., Eliasson, S., Mendrok, J., Eriksson, P., Lee, C., Jiménez, C., Prigent, C., Crewell, S., et al.: Observing ice clouds in the submillimeter spectral range: the CloudIce mission proposal for ESA's Earth Explorer 8, *Atmos. Meas. Tech.*, 5, 1529–1549, 2012.
- Buehler, S. A., Mendrok, J., Eriksson, P., Perrin, A., Larsson, R., and Lemke, O.: ARTS, the Atmospheric Radiative Transfer Simulator – version 2.2, the planetary toolbox edition, *Geosci. Model Dev.*, 11, 1537–1556, <https://doi.org/10.5194/gmd-11-1537-2018>, <https://www.geosci-model-dev.net/11/1537/2018/>, 2018.
- 545 Cazenave, Q., Ceccaldi, M., Delanoë, J., Pelon, J., Groß, S., and Heymsfield, A.: Evolution of DARDAR-CLOUD ice cloud cloud retrieval: new parameters and impacts on the retrieved microphysical properties, *Atmos. Meas. Tech. Discuss.*, 2018, 1–24, <https://doi.org/10.5194/amt-2018-397>, <https://www.atmos-meas-tech-discuss.net/amt-2018-397/>, 2018.
- Delanoë, J., Protat, A., Testud, J., Bouniol, D., Heymsfield, A. J., Bansemer, A., Brown, P., and Forbes, R.: Statistical properties of the 550 normalized ice particle size distribution, *J. Geophys. Res.-Atmos.*, 110, 2005.
- Delanoë, J., Heymsfield, A., Protat, A., Bansemer, A., and Hogan, R.: Normalized particle size distribution for remote sensing application, *J. Geophys. Res.-Atmos.*, 119, 4204–4227, 2014.
- Duncan, D. I. and Eriksson, P.: An update on global atmospheric ice estimates from satellite observations and reanalyses, *Atmos. Chem. Phys.*, 18, 11 205, <https://search.proquest.com/docview/2087361828?accountid=11162>, 2018.
- 555 Eliasson, S., Buehler, S. A., Milz, M., Eriksson, P., and John, V. O.: Assessing observed and modelled spatial distributions of ice water path using satellite data, *Atmos. Chem. Phys.*, 11, 375–391, <https://doi.org/10.5194/acp-11-375-2011>, <https://www.atmos-chem-phys.net/11/375/2011/>, 2011.
- Eriksson, P., Ekström, M., Rydberg, B., and Murtagh, D. P.: First Odin sub-mm retrievals in the tropical upper troposphere: ice cloud properties, *Atmos. Chem. Phys.*, 7, 471–483, 2007.
- 560 Eriksson, P., Rydberg, B., Sagawa, H., Johnston, M., and Kasai, Y.: Overview and sample applications of SMILES and Odin-SMR retrievals of upper tropospheric humidity and cloud ice mass, *Atmos. Chem. Phys.*, 14, 12 613–12 629, 2014.
- Eriksson, P., Ekelund, R., Mendrok, J., Brath, M., Lemke, O., and Buehler, S. A.: A general database of hydrometeor single scattering properties at microwave and sub-millimetre wavelengths, *Earth System Science Data*, 10, 1301–1326, 2018.
- Evans, K. F. and Stephens, G. L.: Microweave radiative transfer through clouds composed of realistically shaped ice crystals. Part II. Remote 565 sensing of ice clouds, *J. Atmos. Sci.*, 52, 2058–2072, 1995.
- Evans, K. F., Walter, S. J., Heymsfield, A. J., and Deeter, M. N.: Modeling of Submillimeter Passive Remote Sensing of Cirrus Clouds, *J. Appl. Meteorol.*, 37, 184–205, [https://doi.org/10.1175/1520-0450\(1998\)037<0184:MOSPRS>2.0.CO;2](https://doi.org/10.1175/1520-0450(1998)037<0184:MOSPRS>2.0.CO;2), [https://doi.org/10.1175/1520-0450\(1998\)037<0184:MOSPRS>2.0.CO;2](https://doi.org/10.1175/1520-0450(1998)037<0184:MOSPRS>2.0.CO;2), 1998.

- Evans, K. F., Wang, J. R., Racette, P. E., Heymsfield, G., and Li, L.: Ice Cloud Retrievals and Analysis with the Compact Scanning Submillimeter Imaging Radiometer and the Cloud Radar System during CRYSTAL FACE, *J. Appl. Meteorol.*, 44, 839–859, 570 <https://doi.org/10.1175/JAM2250.1>, <https://doi.org/10.1175/JAM2250.1>, 2005.
- Fox, S., Lee, C., Moyna, B., Philipp, M., Rule, I., Rogers, S., King, R., Oldfield, M., Rea, S., Henry, M., Wang, H., and Harlow, R. C.: ISMAR: an airborne submillimetre radiometer, *Atmos. Meas. Tech.*, 10, 477–490, <https://doi.org/10.5194/amt-10-477-2017>, <https://www.atmos-meas-tech.net/10/477/2017/>, 2017.
- Fox, S., Mendrok, J., Eriksson, P., Ekelund, R., O’Shea, S. J., Bower, K. N., Baran, A. J., Harlow, R. C., and Pickering, J. C.: Airborne validation of radiative transfer modelling of ice clouds at millimetre and sub-millimetre wavelengths, *Atmos. Meas. Tech.*, 12, 1599–1617, <https://doi.org/10.5194/amt-12-1599-2019>, <https://www.atmos-meas-tech.net/12/1599/2019/>, 2019.
- Geer, A. J., Baordo, F., Bormann, N., Chambon, P., English, S. J., Kazumori, M., Lawrence, H., Lean, P., Lonitz, K., and Lupu, C.: The growing impact of satellite observations sensitive to humidity, cloud and precipitation, *Q. J. R. Meteorol. Soc.*, 143, 3189–3206, 580 <https://doi.org/10.1002/qj.3172>, <https://rmets.onlinelibrary.wiley.com/doi/abs/10.1002/qj.3172>, 2017.
- Geer, A. J., Lonitz, K., Weston, P., Kazumori, M., Okamoto, K., Zhu, Y., Liu, E. H., Collard, A., Bell, W., Migliorini, S., Chambon, P., Fourrié, N., Kim, M.-J., Köpken-Watts, C., and Schraff, C.: All-sky satellite data assimilation at operational weather forecasting centres, *Q. J. R. Meteorol. Soc.*, 144, 1191–1217, <https://doi.org/10.1002/qj.3202>, <https://rmets.onlinelibrary.wiley.com/doi/abs/10.1002/qj.3202>, 2018.
- Houze Jr., R. A.: Structures of atmospheric precipitation systems: A global survey, *Radio Science*, 16, 671–689, 585 <https://doi.org/10.1029/RS016i005p00671>, <https://agupubs.onlinelibrary.wiley.com/doi/abs/10.1029/RS016i005p00671>, 1981.
- Hunter, J. D.: Matplotlib: A 2D graphics environment, *Comput. Sce. Eng.*, 9, 90–95, <https://doi.org/10.1109/MCSE.2007.55>, 2007.
- Korolev, A., Strapp, J. W., Isaac, G. A., and Emery, E.: Improved Airborne Hot-Wire Measurements of Ice Water Content in Clouds, *J. Appl. Opt.*, 30, 2121–2131, <https://doi.org/10.1175/JTECH-D-13-00007.1>, <https://doi.org/10.1175/JTECH-D-13-00007.1>, 2013.
- Mech, M., Orlandi, E., Crewell, S., Ament, F., Hirsch, L., Hagen, M., Peters, G., and Stevens, B.: HAMP – the microwave package on the High Altitude and LOng range research aircraft (HALO), *Atmos. Meas. Tech.*, 7, 4539–4553, <https://doi.org/10.5194/amt-7-4539-2014>, <https://www.atmos-meas-tech.net/7/4539/2014/>, 2014.
- Millán, L., Read, W., Kasai, Y., Lambert, A., Livesey, N., Mendrok, J., Sagawa, H., Sano, T., Shiotani, M., and Wu, D.: SMILES ice cloud products, *J. Geophys. Res.-Atmos.*, 118, 6468–6477, 2013.
- Mlawer, E. J., Payne, V. H., Moncet, J.-L. ane Delamere, J. S., Alvarado, M. J., and Tobin, D. C.: Development and recent evaluation of the MT_CKD model of continuum absorption, *Phil. Trans. R. Soc. A*, 370, 2520–2556, 2012.
- O’Shea, S. J., Choularton, T. W., Lloyd, G., Crosier, J., Bower, K. N., Gallagher, M., Abel, S. J., Cotton, R. J., Brown, P. R. A., Fugal, J. P., Schlenczek, O., Borrmann, S., and Pickering, J. C.: Airborne observations of the microphysical structure of two contrasting cirrus clouds, *Journal of Geophysical Research: Atmospheres*, 121, 13,510–13,536, <https://doi.org/10.1002/2016JD025278>, <https://doi.org/10.1002/2016JD025278>, 2016.
- Oyafuso, F., Payne, V. H., Drouin, B. J., Devi, V. M., Benner, D. C., Sung, K., Yu, S., Gordon, I. E., Kochanov, R., Tan, Y., et al.: High accuracy absorption coefficients for the Orbiting Carbon Observatory-2 (OCO-2) mission: Validation of updated carbon dioxide cross-sections using atmospheric spectra, *Journal of Quantitative Spectroscopy and Radiative Transfer*, 203, 213–223, 2017.
- Perez, F. and Granger, B. E.: IPython: A System for Interactive Scientific Computing, *Computing in Science Engineering*, 9, 21–29, 605 <https://doi.org/10.1109/MCSE.2007.53>, 2007.

- Pfreundschuh, S., Eriksson, P., Buehler, S. A., Brath, M., Duncan, D., Larsson, R., and Ekelund, R.: Synergistic radar and radiometer retrievals of ice hydrometeors, *Atmospheric Measurement Techniques Discussions*, 2019, 1–35, <https://doi.org/10.5194/amt-2019-369>, <https://www.atmos-meas-tech-discuss.net/amt-2019-369/>, 2019.
- Prigent, C., Aires, F., Wang, D., Fox, S., and Harlow, C.: Sea-surface emissivity parametrization from microwaves to millimetre waves, *Q. J. R. Meteorol. Soc.*, 143, 596–605, <https://doi.org/10.1002/qj.2953>, <https://rmets.onlinelibrary.wiley.com/doi/abs/10.1002/qj.2953>, 2017.
- Rodgers, C. D.: Inverse methods for atmospheric sounding: theory and practice, vol. 2, World scientific, 2000.
- Rosenkranz, P. W.: Water vapor microwave continuum absorption: A comparison of measurements and models, *Radio Sci.*, 33, 919–928, 1998.
- Salvatier, J., Wiecki, T. V., and Fonnesbeck, C.: Probabilistic programming in Python using PyMC3, *PeerJ Computer Science*, 2, e55, <https://doi.org/10.7717/peerj-cs.55>, <https://doi.org/10.7717/peerj-cs.55>, 2016.
- Schäfler, A., Craig, G., Wernli, H., Arbogast, P., Doyle, J. D., McTaggart-Cowan, R., Methven, J., Rivière, G., Ament, F., Boettcher, M., Bramberger, M., Cazenave, Q., Cotton, R., Crewell, S., Delanoë, J., Dörnbrack, A., Ehrlich, A., Ewald, F., Fix, A., Grams, C. M., Gray, S. L., Grob, H., Groß, S., Hagen, M., Harvey, B., Hirsch, L., Jacob, M., Kölling, T., Konow, H., Lemmerz, C., Lux, O., Magnusson, L., Mayer, B., Mech, M., Moore, R., Pelon, J., Quinting, J., Rahm, S., Rapp, M., Rautenhaus, M., Reitebuch, O., Reynolds, C. A., Sodemann, H., Spengler, T., Vaughan, G., Wendisch, M., Wirth, M., Witschas, B., Wolf, K., and Zinner, T.: The North Atlantic Waveguide and Downstream Impact Experiment, *Bull. Amer. Met. Soc.*, 99, 1607–1637, <https://doi.org/10.1175/BAMS-D-17-0003.1>, <https://doi.org/10.1175/BAMS-D-17-0003.1>, 2018.
- Simon Pfreundschuh: mcrf – A microwave cloud retrieval framework, <https://github.com/simonpf/mcrf>, <https://doi.org/10.5281/zenodo.3467316>, 2019.
- The Python Language Foundation: The Python Language Reference, <https://docs.python.org/3/reference/index.html>, 2018.
- van der Walt, S., Colbert, S. C., and Varoquaux, G.: The NumPy Array: A Structure for Efficient Numerical Computation, *Computing in Science Engineering*, 13, 22–30, <https://doi.org/10.1109/MCSE.2011.37>, 2011.
- Waliser, D. E., Li, J.-L. F., Woods, C. P., Austin, R. T., Bacmeister, J., Chern, J., Del Genio, A., Jiang, J. H., Kuang, Z., Meng, H., Minnis, P., Platnick, S., Rossow, W. B., Stephens, G. L., Sun-Mack, S., Tao, W.-K., Tompkins, A. M., Vane, D. G., Walker, C., and Wu, D.: Cloud ice: A climate model challenge with signs and expectations of progress, *J. Geophys. Res.-Atmos.*, 114, <https://doi.org/10.1029/2008JD010015>, <https://agupubs.onlinelibrary.wiley.com/doi/abs/10.1029/2008JD010015>, 2009.
- Wang, J., Liu, G., Spinhirne, J., Racette, P., and Hart, W.: Observations and retrievals of cirrus cloud parameters using multichannel millimeter-wave radiometric measurements, *J. Geophys. Res.-Atmos.*, 106, 15 251–15 263, 2001.
- Williams, C. Rasmussen, C. E.: Gaussian processes for machine learning, vol. 2, MIT press Cambridge, MA, 2006.
- Wu, D. L., Jiang, J. H., and Davis, C. P.: EOS MLS cloud ice measurements and cloudy-sky radiative transfer model, *IEEE T. Geosci. Remote*, 44, 1156–1165, 2006.